UNIVERSIDAD DE CANTABRIA

Facultad de Ciencias

Departamento de Ciencias de la Tierra y Física de la Materia Condensada

Tesis Doctoral

SUPER SPIN GLASS BEHAVIOUR IN DILUTED Fe-Au, Ag AND Cu NANOGRANULAR THIN FILMS

Diego Alba Venero

Santander, Mayo de 2011

D. Luis Fernández Barquín, Profesor Titular del Departamento de CITIMAC

INFORMA:

Que el trabajo que se presenta en esta memoria, titulado "COMPORTAMIENTO DE SUPER VIDRIO DE ESPÍN EN PELÍCULAS DELGADAS NANOGRANULARES DILUIDAS DE Fe-Au, Ag Y Cu", ha sido realizado bajo su dirección en el Departamento CITIMAC de la Universidad de Cantabria, y emite su conformidad para que dicha memoria sea presentada y tenga lugar, posteriormente, la correspondiente lectura y defensa.

Santander, Mayo de 2011

Fdo.: Luis Fernández Barquín

"It is a capital mistake to theorise before one has data. Insensibly one begins to twist facts to suit theories, instead of theories to suit facts."
Sherlock Holmes, A scandal in Bohemia.

Contents

Agradecimientos

Este trabajo no hubiera sido posible sin el apoyo constante, tanto profesional como personal, de muchas personas. En particular me gustaría agradecer la importancia de las siguientes personas.

En primer lugar destacar a mi director, Luis Fernández Barquín, no sólo por todo el apoyo y el trabajo que me ha dedicado en estos casi cinco años, si no que su actitud científica ha sido un referente constante. Sin él esta tesis no hubiese sido posible.

A Jesús Rodríguez y José Espeso, por tener siempre la puerta abierta para preguntas, por tontas que fuesen.

Mis primeros pasos en esto de la investigación se los debo a Ángel Mañanes. También fue el que me puso sobre la pista de la beca gracias a la cual he podido realizar este trabajo.

A todos los miembros del CITIMAC, por hacer del departamento un lugar tan agradable donde trabajar. En concreto es obligatorio acordarse de Luis Echeandía, Rosa Cuadra y Nieves Merino, por estar siempre dispuestos a echarme una mano.

I'm also very grateful to David McComb, from the Department of Materials of the Imperial College London, who welcomed me in his group, and to Mahamoud Ardakani, Catriona McGilvery and James Perkins for introducing and teaching me about the sample preparation, TEM and related techniques.

To Sean Langridge, my supervisor at the Large Scale Structures group at ISIS, and to Christy Kinane and Timothy Charlton, for the practical and theoretical lessons on PNR, and a lot of enriching discussions about, neutrons, magnetism and life in general. I want also to mention Ray Fan for help during the SANS experiment.

I also want to mention my local contacts at ILL during the SANS experiment at the D22 beamline, Dr. Albrecht Wiedenmann and to Dr. Naomi Kawamura and Dr. Motohiro Suzuki for his support at the BL39XU at SPring-8.

También tengo que agradecer a nuestros colaboradores españoles. En el País Vasco a Maria Luisa Fernández-Gubieda, Javier Alonso y Andrey Svalov, quienes no sólo prepararon las películas delgadas aquí analizadas, si no que han sido una referencia constante en los aspectos técnicos de su medida y con quienes la discusión científica ha sido fluida y enriquecedora. También a los de Zaragoza, Jesús Chaboy, Cristina Piquer, Roberto Boada y Clara Guglieri, por la ayuda en los experimentos de sincrotrón y por introducirme en los sistemas de aleaciones de metal de transición-tierra rara. Trabajar con todos vosotros es un placer.

Las medidas de EDX se las debo a David Méndez. Muchas gracias por su rapidez, eficiencia y calidad.

A mis compañeros en el despacho *"de más allá de la nevera"*, Toño e Imanol. Siempre habeis tenido palabras de apoyo y muy buenos consejos que darme.

Lidia Rodríguez ha sido un apoyo constante, tanto en la adquisición y el análisis de las imágenes de microscopia electrónica de transmisión, así como en el aprendizaje más profundo de esta técnica.

A los doctorandos con los que he compartido tanto tiempo en el CITIMAC (Rosa, Susana, Álvaro, Pablo, Marta, Cristina, Charly, Gloria, María José y Sander). Si estos años han sido tan buenos en gran parte es por vuestra culpa. Not less important, to my mates at the Imperial College (Alex, Angela, Eva, Farid, Liam, Sebah and Shima) who made me feel like at home nearly thousand miles away.

A todos mis compañeros que han pasado por el Independiente Rugby Club, por compartir conmigo este juego de villanos jugado por caballeros.

Todos mis amigos, con los que he pasado tantos ratos buenos. Seguid así, sois los mejores.

A mi FAMILIA, con mayúsculas como vosotros.

Finalmente me gustaría acordame a las personas más importantes de mi vida: mis

padres, Ana y Pedro, y mi hermano, Fran, por su amor y su apoyo incondicional.

Chapter 1

Resumen

En esta tesis se ha abordado el estudio de las interacciones magnéticas en sistemas nanoparticulados de Fe disueltos en una matriz diamagnética y metálica con la composición Fe_xM_{100-x} (M = Cu, Ag y Au). Estos sistemas tienen forma de película delgada (espesor menor de 300 nm) y una baja concentración de Fe $x < 15\%$ *at*.

Las aleaciones fueron depositadas por la técnica *DC-magnetron sputtering*, que permite producir muestras de alta calidad; perfectamente repetitivas y homogéneas. Asi, se han utilizado diversas técnicas para su caracterización, tanto estructural como magnética. Se ha realizado microscopía de fuerza atómica para medir el espesor de las películas; espectroscopia energía dispersiva de rayos X, en un microscopio electrónico de barrido para obtener la composición química de las aleaciones. Por otro lado se ha utilizado la difracción de rayos X para comprobar la cristalinidad de las muestras, así como la ausencia de fases espúreas. El análisis medidas de transporte eléctrico, variando tanto la temperatura (ausencia de átomos magnéticos disueltos) como el campo magnético (presencia de nanopartículas magnéticas) y microscopía electrónica de transmisión, tanto convencional, como de alta resolución. También se ha llevado a cabo difracción de electrones y microscopía electrónica de transmisión por barrido, incluyendo la técnica de imagen en campo oscuro generada por electrones dispersados a alto ángulo (HAADF). Cabe señalar algunas experiencias realizadas en el difractómetro de bajo ángulo de neutrones polarizados D22, situado en el *Institue Laue-Langevin (ILL)*. En cuanto a las medidas magnéticas,

se han tomado principalmente en el magnetómetro SQUID MPMS XL 5T. En él se ha aplicado tanto medidas de magnetización DC (procesos de enfriamiento sin campo (ZFC) y de enfriamiento con campo (FC) con temperaturas entre 2 y 300 K) como de ciclos de histéresis (hasta $H = 50$kOe) y de susceptibilidad en corriente alterna (0.1 Hz $\leq \omega \leq$ 1000 Hz). Finalmente, se obtuvo tiempo de haz para realizar dicroismo circular de rayos X (XMCD) en el borde de absorción $L_{2,3}$ del Au en el sincrotrón *SPring-8*. También se abordó un tratamiento térmico a distintas temperaturas (hasta 250 °C) en una muestra, modificando su comportamiento magnético.

Cuando el tamaño de los materiales ferromagnéticos se reduce por debajo de un tamaño crítico (típicamente en la nanoescala) emergen partículas monodominio. Cuando estas nanopartículas están aisladas unas de las otras y suficientemente diluidas, presentan un comportamiento superparamagnético. Éste es muy similar a los paramagnéticos clásicos, pero fluctuando todo el momento magnético de la nanopartícula (acoplado por canje directo y llamado superespín) en lugar de todos los momentos magnéticos atómicos independientemente. Sin embargo, cuando se favorecen la existencia de interacciones magnéticas, aparecen comportamientos muy distintos (y complejos), tales como el super vidrio de espín (fase donde los superespines están frustrados) o el super ferromagnetismo donde todos los superespines están alineados por las interacciones interparticulares.

En nuestro estudio en concreto, los resultados obtenidos han sido sorprendentes por dos motivos. El primero es la gran cantidad de interacciones existentes pese a lo diluido de las muestras (del orden del 10% *at.* en Fe), observando ciclos de histéresis a temperatura ambiente. Este comportamiento (contrario a lo observado previamente en la literatura) pone de manifiesto la importancia de la nanoestructura, destruyendo aquí la fase puramente superparamagnética. El segundo resultado fuera de lo común es la obtención de fases tipo vidrio de espín en sistemas que clásicamente no lo admitian debido a su fuerte comportamiento Kondo, como son las aleaciones de FeCu y FeAg. La existencia de nanopartículas magnéticas permite una nueva visión de este problema.

Recapitulando: se han fabricado nanostructuras en forma de películas delgadas, con una baja concentración de material ferromagnético y con distintas matrices de metal

noble. Se ha realizado una profunda caracterización tanto estructural como magnética, con técnicas de laboratorio y en grandes instalaciones. Asimismo, se han probado varios modelos teóricos, y se ha comparado sistemáticamente con sistemas similares (tanto en forma masiva (*bulk*) como en forma de película degada) para conseguir un entendimiento global del magnetismo subyacente del sistema.

Chapter 2

Introduction

Since the dawn of mankind, the available tools have played a key role. In ancient times, the discovery of the synthesis and manipulation of a new kind of materials with enhanced properties led to changes in the prehistoric age. For example, the Stone Age finished when the improved properties of the bronze were understood, allowing the manufacture of improved tools. The twilight of the Bronze Age came with the beginning of the use of the Iron. This trend is still a driving force in todays research: even now, the discovery of brand new materials changes our way of life, allowing the production of new and more sophisticated tools or improving the existing ones. In particular, magnetic materials are present everywhere in a daily life in form of both, high and low technology. As an example there are magnetic materials in cellphones, speakers, induction cookers, magnetic recording media, magnetic resonance imaging devices, cores of motors or electric transformers, etc. [1, 2]. In short, the field of magnetism is still in phenomenal shape and future trends are clearly foreseen.

Reducing the size of the material to the nanoscale, favours the emergence of new properties. The nanoscience dug its roots in the sixties, when Richard P. Feynman disserted about the possibilities of the reducing size materials (and tools) in his talk *"There's plenty of room at the bottom"*. Nowadays the understanding of the new properties and its relation with size reduced materials (nanoscience) are much more developed than its use in actual devices (nanotechnology). The boom of the nanoscience was in 1981 with

the development of the scanning tunneling microscope, allowing not only the imaging of a single atom but also its manipulation. In addition, the electron microscopes, which became popular among research institutions almost simultaneously, permits as well such an impressive development.

Magnetism was one of the pioneering disciplines to address the properties at the nanoscale. In particular, improving dramatically the quality of soft magnets and the cost-reduction of the expensive and indispensable rare-earth based permanent magnets [3]. More recently the entry of the magnetism in biomedical applications, not only allows the imaging but also therapeutical applications, like a selective drug delivery or hyperthermia treatment [4]. These were only possible through the use of systems at the nanoscale. When the size of a magnetic material is reduced, the number of magnetic domains diminishes. If a critical size is reached, the particle will be completely magneticaly coupled, without magnetic domains, forming a *superspin* [5]. Concretely, systems comprising nanoparticles has experimented a research explosion in the last decade, although back in 1949, L. Néel established the basis of the behaviour of the magnetic nanoparticles with his seminal work *Théorie du trainage magnétique des ferromagnétiques en grains fins avec applications aux terres cuites* [6]. If the system is diluted enough the magnetic interactions among the particles (direct exchange, dipolar and Ruderman-Kittel-Kasuya-Yosida: RKKY) will be feeble. This will lead in practice to a superparamagnetic (SPM) state.

Other systems close in their magnetic behaviour to SPM, are those comprising magnetic impurities randomly dispersed on a diamagnetic matrix with random magnetic interactions. These have been called as spin glasses (SG). This kind of systems, widely studied since some decades ago, presents implications for other scientific attractive subjects, such as those modeling neural networks [7].

In this work, both kind of systems (SPM & SG) have been combined, with the aim of producing metals composed by *superspins* randomly placed in a non magnetic matrix and with random interactions (mainly dipolar, since they depend on the relative orientation of the *superspins*). If these interactions are strong enough, they will modify the energy

landscape of a SPM system, leading to the superspin glass (SSG) behaviour. Other kind of interactions can also play a role, although their final influence is expected to be weak.

One of the main challenges of the nanomagnetism is to achieve an unambiguous understanding of the interplay between the nanostructure of the systems and the macroscopic magnetic behaviour. In the present work, we have studied the magnetic interactions in magnetically-diluted systems in thin film shape. Fe and a non-magnetic conductive noble metal (Cu, Ag or Au) were deposited on Si (100) substrate by DC-magnetron sputtering giving as a result thin films (thickness below 300 nm) composed by Fe nanoparticles embedded in a noble metal matrix. It is important to remark that this study is fully complementary to that carried out very recently on Fe_xAg_{100-x} ($20 \leq x \leq 55$) in collaboration with the group led by *Prof. M. L. Fdez-Gubieda*. Similar systems (comprising magnetic nanoparticles with non-magnetic and both conductive and non-conductive matrices) had being studied in a wide compositional range and will be then useful systems for the mentioned comparison. One landmark of the current work is the deposition of films of FeCu and FeAg with a SSG behaviour. The lack of solubility of the Fe in both noble metals, and in the case of Cu, the high Kondo temperature, mask the spin glass behaviour in traditional bulk alloys [8].

As it will be shown in the development of this thesis, the work has been performed in very diluted systems. On top of the low amount of mass available for each sample, the dilution of the magnetic material adds supplementary difficulty to extract quantitative magnetic information. In consequence, the performed magnetometry experiments have been extremely challenging. In this sense this work contributes to settle the basic procedures for working with systems with *ultra* low magnetic response.

The structure of the work is as follows: after the introduction (the current chapter), the main physical concepts needed for the understanding of the studied systems are reminded in **Chapter 3**. Next, **Chapter 4** presents the fabrication of the thin films by the DC-magnetron sputtering. Furthermore powdered systems produced by mechanical alloying have also been produced for comparison purposes. Details of the alloying procedure will be given, although their magnetic behaviour is much less interesting. The experimental

techniques used in the frame of this work are introduced in **Chapter 5**. **Chapter 6** describes all the various experimental results. Considering the complexity of the systems and that the interpretation of the overall physics behind the alloys requires more than one technique for being settled, **Chapter 7** puts forward a debate of all the implications and meaning of those experimental results. Finally the main conclusions gathered along the thesis are summarised in **Chapter 8**.

Bibliography

[1] S. D. Bader. Colloquium: Opportunities in Nanomagnetism. *Rev. Mod. Phys.*, **78**:1, 2005.

[2] O. Gutfleisch, M. A. Willard, E. Brück, C. H. Chen, S. G. Sankar, and J. P. Liu. Magnetic materials and devices for the 21st century: stronger, lighter and mor energy efficient. *Adv. Mater.*, **23**:821, 2011.

[3] G. Herzer. Grain structure and magnetism of nanocrystalline ferromagnets. *IEEE transactions on magnetics*, **25**:3327, 1989.

[4] Q.A. Pankhurst, J. Connolly, S.K. Jones, and J. Dobson. Applications of magnetic nanoparticles in biomedicine. *J. Phys. D*, **36**:R167–R181, 2003.

[5] S. Bedanta and W. Kleemann. Supermagnetism. *J. Phys. D: Appl. Phys.*, **42**:013001, 2009.

[6] L. Néel. Théorie du trainage magnétique des ferromagnétiques en grains fins avec applications aux terres cuites. *Ann. Geophys.*, **5**:99–136, 1949.

[7] Daniel J. Amit, Hanoch Gutfreund, and H. Sompolinsky. Spin-glass models of neural networks. *Phys. Rev. A*, **32**:1007–1018, 1985.

[8] J. A. Mydosh. *Spin Glasses: An Experimental Introduction.* Taylor and Francis, London, 1993.

Chapter 3

Theoretical background

The initial relevant steps in nanomagnetism were given in the pioneering work of L. Néel [1], mostly focused on the understanding of spin relaxation phenomena. It is widely known that when the size of a ferromagnetic material is reduced to (below) a certain value (depending on the magnetic anisotropy of the system) within the nanoscale, the domain structure tends to the presence of a unique single-domain arrangement [2]. Typically each nanoparticle contains magnetic moments, frequently ferromagnetically coupled by direct exchange. When the temperature is high enough (but below the Curie temperature of the bulk), the overall particle magnetic moment (labelled as *superspins*) is flipping between the easy-axis directions, behaving in a fashion resembling that of a paramagnetic (PM) state. In such a situation, the flipping is a coupled spin rotation of all the moments in the particle, whereas in the PM state it obviously involves single atomic spins. By contrast with the pure PM, the ensemble of spins in the particle can become *blocked* at low temperatures in a random arrangement as will be explained in the following. Despite the appeal of this topic, the work had been restricted to a few groups who provided a fabulous support for the boom in the field when the nanoscience came into play around the eighties. This relatively low input (although of high quality) was surely due to the intrinsic difficulties of synthesising and measuring nanoparticles sometimes with very weak magnetic response.

However, more recently a huge research effort has been put in the understanding of

such systems [3, 4, 5], not only interesting from the fundamental point of view, but also with very attractive applications, as occurs with aspects of paramount importance as the giant magnetoresistance or the selective targeting of drugs, to cite just two of them [6].

Magnetic domains are formed in order to reduce the magnetostatic energy, but with the additional drawback (from an energetic point of view) of the creation of Bloch walls [2]. When the particle size decreases, the magnetostatic energy is also reduced (it is proportional to the volume). For this reason, the creation of domain walls is less and less energetically favourable when the size decreases. Eventually, a critical size is reached and the energy cost of forming domain walls is greater than the energy gained reducing the magnetostatic energy, giving rise to a single-domain particle. Typical critical radii are 15 nm for Fe, 35 nm for Co or 750 nm for $SmCo_5$ [7]. Such a critical size depends on the exchange, anisotropy and magnetisation through the relationship:

$$r_c \approx 9\frac{(AK)^{\frac{1}{2}}}{\mu_0 M_s^2} \tag{3.1}$$

where A is the exchange constant, K is the uniaxial magnetic anisotropy of the particle, μ_0 is the constant of permeability, and M_s is the saturation magnetisation.

Isolated magnetic single-domain particles are initially assumed to present uniaxial anisotropy [1, 8, 9], with two magnetic-degenerated (see Fig. 3.1) states along the easy axis. The system anisotropy energy will be:

$$E = KVsin^2(\theta) \tag{3.2}$$

where V is the particle volume and θ is the angle between the particle magnetic moment and the easy axis. It is then needed the presence of an external energy to allow the transition between both spin configurations in the particle, separated by the energy barrier ($E_b = KV$). Due to the small size necessary to achieve single-domain particles, and although the anisotropy energy is usually one order of magnitude larger than in the bulk systems [10, 11, 12] low thermal energies are usually sufficient to overcome the anisotropy barrier and induce the transition between both magnetic states [13]. When a magnetic field H is applied, the degeneracy of both magnetic states is broken down, with a decrease

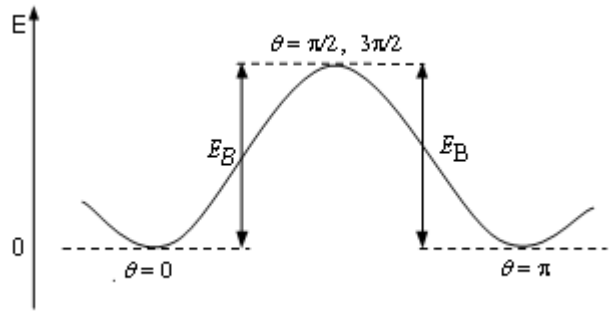

Figure 3.1: *Typical representation of the magnetic energy levels of a nanoparticle in absence of field. $\theta = 0$ and $\theta = \pi$ correspond to the two equally energetic spin configurations.*

of $MHcos\theta$ (with θ the angle between the applied field and the easy axis) in the energy level corresponding to the spin aligned to the field and an increase of the same value to the spins opposite to the field. Macroscopically the presence of such a barrier can be easily detected with standard DC-magnetometry. The presence of an energy barrier separates effectively the behaviour of single-domain particles in two thermal windows. Above a certain temperature the system is in the so-called superparamagnetic (SPM) state, where the whole particle is flipping continuously and coherently. The other region is entered when the system is cooled down to low enough temperatures so that each ensemble of spins within single-domain will be randomly trapped into one of the two possible magnetic levels.

The transition between spin configurations takes a certain relaxation time. This relaxing process was predicted to follow an Arrhenius-Néel law:

$$\tau = \tau_0 e^{-\frac{E_B}{k_B T}} \tag{3.3}$$

where τ is the system relaxation time, τ_0 is the intrinsic relaxation time (10^{-13} s typically for non-interacting particles [14]), E_B the energy barrier between both stable magnetic states of the superspin (usually is assumed to be proportional to the product of the nanoparticle volume times the magnetic anisotropy), k_B is the Boltzmann constant and T the absolute temperature. The *measuring time*, t_m of each technique is a crucial parameter

when dealing with systems of magnetic nanoparticles. The blocking temperature T_B is defined as the temperature where $\tau = t_m$. At a fixed temperature, if the $t_m \gg \tau$ the magnetic response will be SPM-like. On the other hand, if $t_m \ll \tau$ the system response will be static. If the t_m is fixed, when $T > T_B$ the system will behave like a SPM, where it will be blocked at $T < T_B$. Naturally, if $T > T_B$ the SPM behaviour will present the same features as the PM state. Among the latter, it is obvious the absence of coercivity and a field dependence of magnetisation (at a fixed temperature) following the Langevin model.

If a field is applied, the degeneration of both states will be lifted, as can be observed in figure 3.2. Nevertheless, due to the anisotropy barrier, the spins will continue in a *blocked* state if the system is at low enough temperature. When thermal energy is added into the system, this will enable the spins at the excited state to overcome the anisotropy barrier, allowing a decay to the fundamental state for some of the particles. This results in a raise of the magnetisation when heating. Once the thermal energy exceeds that of the barrier of the fundamental state ($k_bT > KV + MH$), the spins can flip over both states (fundamental and excited), reducing the magnetisation of the sample above such a temperature. When we cool down with an applied field (FC process), the degeneration of the magnetic states does not exist and accordingly the magnetisation should grow when decreasing the temperature (the fundamental energy states should be thermally accessible, while the states with the magnetic moment opposite to the magnetic field not). Eventually, the system will arrive to a state where all the spins will be in the ground state. Further cooling should not increase the system magnetisation significantly, since all the moments should be aligned with the field (yet obeying thermal disorder inside the nanoparticle).

When the applied field is greater than $\frac{KV}{Mcos(\theta)}$, only the level with the magnetisation parallel to the field is stable, removing the two level system. Such an intense field does not allow the existence of irreversibilities between the ZFC and the FC [13]. To summarise the rich variety of ingredients for a basic description of a SPM system, is to count with single-domain magnetic particles behaving independently. In this way, there will be

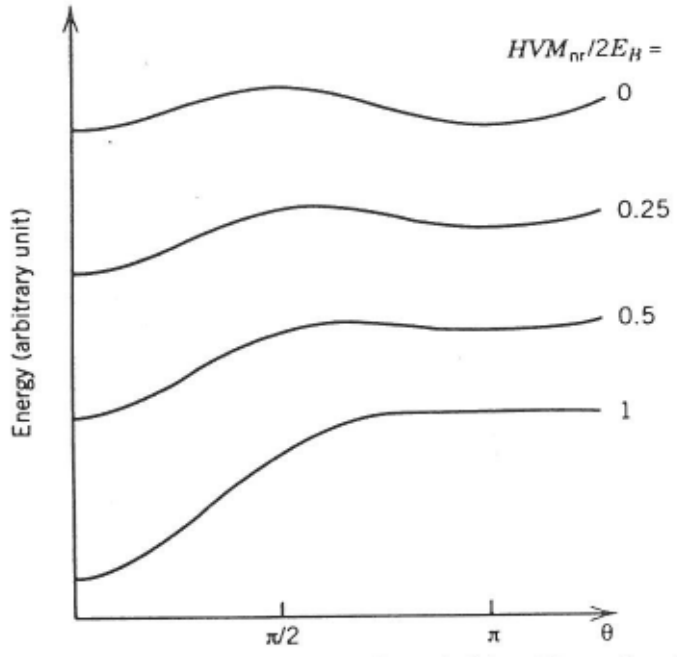

Figure 3.2: *Variation of the magnetic energy levels when a magnetic field is applied. Reproduced from [13].*

blocked/unblocked spin states with a blocking temperature related to an energy barrier. This barrier depends on the anisotropy and the volume of the particle. The spin relaxation follows the mentioned Arrhenius-Néel law with a (super)paramagnetic response for $T > T_B$.

Another basic pillar supporting the global understanding of the nanomagnetism is found in systems consisting of diluted magnetic ions massively surrounded by a non-magnetic host. These materials lie in the family of spin glass (SG) materials, in which a random spatial arrangement and competing interactions are present [15, 16]. The canonical spin glasses (Fe solved in Au, Mn in Ag or Cu, for example) have suffered a wide and exhaustive study during the seventies-eighties. The appeal of such SGs stems from the still ambiguous definition of the possible magnetic phase transition taking place. Even nowadays this is an intriguing field where notable and profound discussions are held depending of different conditions, like the presence or not of an external magnetic field, or if the spins follow a Heisenberg of Ising model [17, 18], to cite a few. At high tempera-

tures these magnetic materials behave like paramagnets, with no correlation among the solved spins. When the system is cooled down, the spin glass state comes into play. The competition of interaction and randomness gives rise to the concept of magnetic frustration. A spin is typically frustrated when suffers interactions both, ferro and antiferromagnetic simultaneously. In the canonical conducting spin glasses, the ruling interaction is the Ruderman-Kittel-Kasuya-Yosida (RKKY) and the corresponding Hamiltonian is described as:

$$H = J_{RKKY}(r)\boldsymbol{\mu}_i \cdot \boldsymbol{\mu}_j \tag{3.4}$$

where $\boldsymbol{\mu}$ is the magnetic moment of the impurities i and j and $J_{RKKY}(r)$:

$$J_{RKKY}(r) = 6\pi Z J^2 N(E_F)[\frac{sin(2k_F r)}{(2k_F r)^4} - \frac{cos(2k_F r)}{(2k_F r)^3}] \tag{3.5}$$

with Z is the number of conduction electrons per atom, J is the s-d exchange, $N(E_F)$ is the density of states at the Fermi energy, k_F is the Fermi momentum and r is the distance between the two interacting moments. When the SG is found in an insulating host the superexchange and dipolar interactions govern the system. The latter is expressed as:

$$H_{ij}^{dip} = \frac{1}{r_{ij}}[\boldsymbol{\mu}_i \cdot \boldsymbol{\mu}_j - 3(\boldsymbol{\mu}_i \cdot \hat{r}_{ij})(\boldsymbol{\mu}_j \cdot \hat{r}_{ij})] \tag{3.6}$$

In both cases (eq. 3.4 and 3.6), the sign of the interaction varies from positive to negative (or equivalently from ferro to antiferromagnetic coupling) with the distance in the RKKY or with the relative orientation in the dipolar. At high temperatures, the thermal fluctuations of the magnetic impurities will be the dominating process. However, when the system is cooled down, a magnetic state is established down with random spin configuration. Incidently, the spin glass state, was chiefly characterised by (among others) a cusp in the thermal variation of the χ_{AC} susceptibility (which is frequency dependent), the absence of long range order and a special decay of the remanent magnetisation with the time (aging) [19]. Different models have been developed to describe the SG state. Among them, it is recurrent to take into account the Edward-Anderson model. This is a mean-field

approach where the spin positions are in a regular lattice and the disorder is introduced by a suitable distribution of exchange bonds. Alternatively the Sherrington-Kirpatrick (an extension of the Edward-Anderson model) assumes an infinite range for interactions and that each spin is equally coupled to the other spins. The Droplet model deals with low-lying excitations which dominate the long-distance and long-time correlations in the Ising-spin glass are clusters or *droplets* of coherent flipped spins. The fractal-cluster model where the droplets have a correlation length ξ which diverges as $(\frac{T}{T_f} - 1)^{\nu}$. The volume of these clusters is ξ^D where D is the fractal dimension) [16, 15, 20, 21, 22]. The spin glasses have then been theoretically described as a collection of single spins (sometimes clustered in small pockets) which interact collectively giving rise to a disordered magnetic state below the freezing temperature.

Another effect found in ensembles of nanomagnetic particles is the drastic variation of the anisotropy when varying the magnetic size. In Fig. 3.3 we show a very popular picture of K vs D (more precisely, H_c) in magnetic alloys. In this diagram it is shown the $K \propto \frac{1}{D^6}$ dependence for very small D values. This variation is explained by the random anisotropy model (RAM), originally developed for *ultrasolft* nanocrystalline alloy produced from amorphous magnetic alloys acting as precursors [23]. In such systems the low coercive force is achieved when the magnetic (exchange) correlation length exceeds the size of the nanograins. Since the magnetic anisotropy (K) of each grain is randomly distributed, the resulting anisotropy is an average of all the coupled grains:

$$\langle K \rangle = \frac{K}{\sqrt{N}} \tag{3.7}$$

with N the number of grains coupled. When the temperature rises, the correlation length begins to drop, and hence the number of coupled grains. At low temperatures there is a compensation between the decrease of the anisotropy of each grain K and the reduction in the number of grains. At high enough temperatures, the correlation length is reduced to each nanocrystal, leading to a remarkable rise of the average magnetic anisotropy [23].

In the present work, ingredients from all these models will be used altogether. Randomness and competitive magnetic interactions (concepts arising from the spin glasses

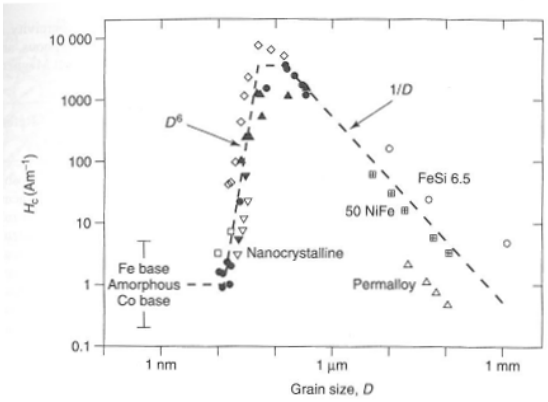

Figure 3.3: *Variation of the coercive field with the grain size. At high particle diameters there is a linear increase of the coercivity with the particle size reduction. When D reaches a critical size, the average anisotropy predicted by the RAM comes into play, resulting in a drastic reduction of the coercivity. Reproduced from [24].*

systems) will affect single-domain particles, modifying the SPM behaviour, leading to a weakly interacting superparamagnetism or, in this particular case a super spin glass (SSG) behaviour.

The SSG presents similarities in the properties of the canonical SG, like the aging or the cusp in the $\chi_{AC}(T)$. SSGs are found in, as example discontinuous metal-insulator multilayers [3], Fe-C nanoparticles in a frozen ferrofluid [25], nonstoichiometric manganites [26] or Fe_xAg_{100-x} granular thin films [27]. The term SSG has been coined relatively recently although this was discussed briefly by K. Binder and A. P. Young in 1986 [16] and it also follows the ideas described in goethite by S. Morup's group [28]. Basically it describes a group of magnetic materials comprising nanoparticles which are interacting through the matrix. In such states, the ruling interaction is the dipolar. Calculations by Altbir and coworkers [29] showed that when the particle size exceed 1 nm, the RKKY interaction is negligible compared with the dipolar just a few interatomic distances away. The study of this field in magnetism is becoming really attractive, especially in connection to the also similar, so called, superferromagnetism. The latter state is produced if the concentration of nanoparticle increases (but below the physical percolation) eventually

producing a rise in the interparticle interactions. Finally this can lead to a *kind* of ferromagnetic domain state [30]. FM-like correlations will arise between the superspins, of the nanoparticles in addition to those between the atomic moments within the particles. The intrinsic behaviour of SSG has not been theoretically explained yet and it is difficult to get analytical expressions due to the intrinsic complexity of spin glass Hamiltonians [31].

In consequence, the description of the SSG and SFM is mostly based on phenomenological approaches of the χ_{AC} and $M_{DC}(T)$ data. Some of the most salient features of what it is now labelled as *supermagnetism* are briefly described in the following. It should be noted that not all the analysed materials give a experimental unique response to confront the models, and thus permiting a clear definition of the magnetic state. In any case among the most salient phenomenological features we can indicate the parameters for a critical slowing down. In the canonical spin glasses the values lay near the $5 \leq z\nu \leq 11$ of the canonical spin glasses; for example Al_2O_3/Co discontinuous multilayer present $z\nu = 10.2$ [32], Fe_3O_4 $z\nu = 9$ [33], frozen ferrofluids $z\nu = 11.4$ [34] and Fe_xAg_{100-x} ($x = 39$, 34 and 24) have $z\nu = 8.3$, 4.7 and 4.3 respectively. Another feature meriting attention is the so-called Cole-Cole plots (χ'' vs χ'). This also presents modifications respect to the classical SPM. As was previously reported [35], [36] the typical shape is a flattened semicircle (where in classical SPM, that is a pure semicircle). Last but not least, aging experiments are another useful method to prove spin glass behaviour. It consists in cooling the sample in absence of field from above the glass temperature to below T_g. After a waiting time t_w a small DC magnetic field is applied, and then, the magnetisation is recorded as a function of time. Since the variation of the relaxation is dependent on the t_w, the spin system is in a non-equilibrium state during the waiting time. Variations of these processes are possible but the underlaying physical idea is the same.

Bibliography

[1] L. Néel. Théorie du trainage magnétique des ferromagnétiques en grains fins avec applications aux terres cuites. *Ann. Geophys.*, **5**:99–136, 1949.

[2] B. D. Cullity. *Introduction to magnetic materials.* Addison-Wesley, Massachusetts, 1972.

[3] S. Bedanta and W. Kleemann. Supermagnetism. *J. Phys. D: Appl. Phys.*, **42**:013001, 2009.

[4] X. Batlle and A. Labarta. Finite-size effects in fine particles: magnetic and transport properties. *J. Phys. D: Appl. Phys.*, **35**:R15–R42, 2002.

[5] Franz Bødker, Mikkel F. Hansen, Christian Bender Koch, Kim Lefmann, and Steen Mørup. Magnetic properties of hematite nanoparticles. *Phys Rev. B*, **61**:6826, 2000.

[6] S. D. Bader. Colloquium: Opportunities in Nanomagnetism. *Rev. Mod. Phys.*, **78**:1, 2005.

[7] D. Givord, Q. Lu, and M. F. Rossignol. *Science and Technology of Nanostructured Materials.*

[8] R. H. Kodama, A. E. Berkowitz, E. J. McNiff, Jr., and S. Foner. Surface spin disorder in $NiFe_2O_4$ nanoparticles. *Phys. Rev. Lett.*, **77**(2):394–397, Jul 1996.

[9] P. Gambardella, S. Rusponi, M. Veronese, S. S. Deshi, C. Grazioli, A. Dallmeyer, I. Cabria, R. Zeller, P. H. Dederichs, K. Kern, C. Carbone, and H. Brune. Giant magnetic anisotropy of single Co atoms and nanoparticles. *Sci.*, **300**:1130, 2003.

[10] L. Fernández Barquín, R. García Calderón, B. Farago, J. Rodríguez-Carvajal, A. Bleloch, D. McComb, R. Chater, and Q. A. Pankhurst. Neutron spin echo evidence of mesoscopic spin correlations among Fe(Cu) ferromagnetic nanoparticles in a silver diamagnetic matrix. *Phys. Rev. B*, **76**(17):172404, 2007.

[11] F. Bødker, S. Mørup, and S. Linderoth. Surface effects in metallic iron nanoparticles. *Phys. Rev. Lett.*, **72**:282, 1994.

[12] D. H. Ucko, Q. A. Pankhurst, L. Fernández Barquín, J. Rodríguez Fernández, and S. F. J. Cox. Magnetic relaxation in the nanoscale granular alloy $Fe_{20}Cu_{20}Ag_{60}$. *Phys. Rev. B*, **64**:104433, 2001.

[13] J. L. Dormann, D. Fiorani, and E. Tronc. Magnetic relaxation in fine-particle systems. *Adv. Chem. Phys.*, **98**:283, 1997.

[14] J. L. Tholence and R. Tournier. Susceptibility and remanente magnetization of a spin glass. *Journal de physique*, **5**:C4–229, 1974.

[15] J. A. Mydosh. *Spin Glasses: An Experimental Introduction.* Taylor and Francis, London, 1993.

[16] K. Binder and A. P. Young. Spin glasses: Experimental facts, theoretical concepts, and open questions. *Rev. Mod. Phys.*, **58**:801, 1986.

[17] Petra E. Jönsson, Hiroko Aruga Katori, Atsuko Ito, and Hajime Takayama. Field effects in the ising spin glass $Fe_{0.55}Mn_{0.45}TiO_3$. *Progress of Theoretical Physics Supplement*, **157**:38–41.

[18] A. P. Young. Phase transitions in spin glasses. *J. Magn. Magn. Mat.*, **310**:1482–1486, 2007.

[19] D. Chowdhury. *Spin glasses and other frustrated systems.* World Scientific, Singapore, 1986.

[20] Daniel S. Fisher and David A. Huse. Ordered Phase of Short-Range Ising Spin-Glasses. *Phys. Rev. Lett.*, **56**:1601, 1986.

[21] T. Jonsson, P. Svedlindh, and M. F. Hansen. Static Scaling on an Interacting Magnetic Nanoparticle System. *Phys. Rev. Lett.*, **81**:3976, 1998.

[22] Daniel S. Fisher and David A. Huse. Equilibrium behavior of the spin-glass ordered phase. *Phys. Rev. B*, **38**:386, 1988.

[23] G. Herzer. Grain structure and magnetism of nanocrystalline ferromagnets. *IEEE transactions on magnetics*, **25**:3327, 1989.

[24] H. S. Nalwa, editor. *Magnetic nanostructures*. American scientific publishers, California, 2002.

[25] C. Djurberg, P. Svedlindh, P. Nordblad, M. F. Hansen, F. Bødker, and S. Mørup. Dynamics of an Interacting Particle System: Evidence of Critical Slowing Down. *Phys. Rev. Lett.*, **79**:5154, 1997.

[26] C. Raj Sankar and P. A. Joy. Superspin glass behavior of a nonstoichiometric lanthanum manganite $LaMnO_{3.13}$. *Phys. Rev. B*, **72**:132407, 2005.

[27] J. Alonso. *Collective magnetic behaviours of Fe_xAg_{100-x} ($20 \leq x \leq 55$) granular thin films ans their structural characterization*. PhD thesis, Universidad del Pais Vasco, 2010.

[28] Steen Mørup, Morten Bo Madsen, Jørgen Franck, Jørgen Villadsen, and Christian J.W. Koch. A new interpretation of Mössbauer spectra of microcrystalline goethite: "Super-ferromagnetism" or "super-spin-glass" behaviour? *J. Magn. Magn. Mat*, **40**:163–174, 1983.

[29] D. Altbir, J. d'Albuquerque e Castro, and P. Vargas. Magnetic coupling in metallic granular systems. *Phys. Rev. B*, **54**:R6823, 1996.

[30] S. Bedanta, T. Eimuller, W. Kleemann, J. Rhensius, F. Stromberg, E. Amaladass, S. Cardoso, and P. P. Freitas. Overcoming the dipolar disorder in dense CoFe nanoparticle ensembles: Superferromagnetism. *Phys. Rev. Lett.*, **98**:176601, 2007.

[31] S. G. Magalhaes, F. M. Zimmer, and B. Coqblin. Van Hemmen-Kondo model for disordered strongly correlated electron systems. *Phys. Rev. B*, **81**:094424, 2010.

[32] S. Sahoo, O. Petracic, W. Kleemann, S. Stappert, G. Dumpich, P. Nordblad, S. Cardoso, and P. P. Freitas. Cooperative versus superparamagnetic behavior of dense magnetic nanoparticles in $Co_{80}Fe_{20}/Al_2O_3$ multilayers. *Appl. Phys. Lett.*, **82**:4116, 2003.

[33] Pankaj Poddar, Tamar Telem-Shafir, Tcipi Fried, and Gil Markovich. Dipolar interactions in two- and three-dimensional magnetic nanoparticle arrays. *Phys. Rev. B*, **66**:060403, 2002.

[34] P. E. Jonsson. Superparamagnetism and Spin Glass Dynamics of Interacting Magnetic Nanoparticle Systems. *Adv. Chem. Phys*, **128**:191, 2004.

[35] O. Petracic, X. Chen, S. Bedanta, W. Kleemann, S. Sahoo, S. Cardoso, and P.P. Freitas. Collective states of interacting ferromagnetic nanoparticles. *J. Magn. Magn. Mat*, **300**:192–197, 2006.

[36] J. Alonso, M. L. Fdez-Gubieda, J. M. Barandiarán, A. Svalov, L. Fernández Barquín, D. Alba Venero, and I. Orue. Crossover from superspin glass to superferromagnet in Fe_xAg_{100-x} nanostructured thin films ($20 \leq x \leq 50$). *Phys. Rev. B*, **82**:054406, 2010.

Chapter 4

Synthesis of the samples

In this work we have prepared pseudobinary [(FeCu)-Au] alloys and binary Fe-Au nanometric grains embedded in a nanocrystaline Au matrix in powdered state. Likewise and constituting the mainframe of the thesis truly binary alloys of Fe nanoparticles in Au, Ag or Cu matrices in the shape of thin films (thickness, $z \leq 300$ nm) have been extensively produced. The preparation has been carried out by mechanical alloying (powders) and by DC-magnetron sputtering (thin films).

4.1 Mechanical alloying

The mechanical alloying is a synthesis technique to produce powder samples by the continuous fracture-soldering of the original material (usually powdered elements or alloys) [1]. The original materials are inserted into a container with some balls. The balls and the containers are typically made of stainless steel or WC for metals. Then, the container is placed on a platform which rotates, allowing a planetary (supplementary) movement. The synthesis is caused by the continuous collisions of the balls with the material. The mechanically alloying can produce a wide variety of samples in both, equilibrium or non-equilibrium phase: supersaturated solid solutions, metastable crystalline phases, amorphous alloys or nanostructures [2].

The main controlling parameters of the instrument are the material of the balls and

the recipient, the relation between the mass of the balls and the material in the container, the atmosphere, the angular-speed of the spinning plate and the time of milling. Although the method is relatively simple, the mentioned variety of parameters, results in a time consuming task to find the optimal combination for a particular alloy. In this sense, the previous work made by *Dr. R. García Calderón* has set the basis for the current synthesis [3]. In our case, FeAu and FeCuAu alloys had been produced by this route, in different nominal compositions: $Fe_{10}Au_{90}$, $Fe_{10}Cu_{10}Au_{80}$ (1 and 2) and $Fe_{15}Cu_{15}Au_{70}$.

The milling process has been carried out in a commercial *Retsch PM 400/2* (Fig. 4.1 located in the *Universidad de Cantabria*. All the samples have been milled in 125 ml WC container, under Ar (99.99%) atmosphere to avoid oxidation, at 200 rpm and with a ball/sample mass relation of 12/1. The milling time extended to 70 h, but not in a continuous way: after each hour of milling we allow another hour of pause, to avoid the excessive heating of the containers, which could produce spurious phases and reaggregation.

Figure 4.1: *Planetary ball mill Retsch PM 400/2. WC balls and containers have been used in our particular case.*

4.2 DC-Magnetron sputtering

The sputtering (see Fig 4.2) is a widely used technique in research and the industry (especially in the field of coating applications for, e.g., metal-working industry, biomedical

applications, and optical or electrical components) [4]. The technique is based on the evaporation of bulk substances and its deposition onto a substrate to form a thin film. In particular, we have used the DC-magnetron sputtering; in the evaporation process, the target (the substance to sputter) is placed on the magnetron (the cathode, made of an arrange of magnets). High vacuum ($\sim 10^{-7} mbar$) is achieved in the evaporation chamber, to avoid air contamination and resputtering processes by the O^- ions. Then, the working gas (Ar in our case, due to its low reactivity and heavy enough for an efficient momentum transfer) is introduced and ionised (Ar^+). The ionisation is achieved when a large potential difference (500 V) is applied between the anode and the magnetron (the cathode of the system), chasing the acceleration of the Ar^+ ions. If the plasma is energetic enough (around four times the value of the sublimation heat of the system [5]), an evaporation of the target atoms is produced. Other effects as the displacement of the atoms in the target surface or the inclusion of the sputtering gas in the target can be present. The magnetron allows the reduction of the quantity of gas needed for the formation of a plasma, due to the confinement of free electrons in their own magnetic field. This favours e^--gas collisions and hence, an improvement of the sputtering rate [6].

The sputtered samples are often multilayers, which are deposited by changing the target after the deposition of each layer. However, we are here interested in granular samples, and the deposition technique is slightly different: in the same target position we place a disk with a diameter around 7 cm of noble metal (Au, Ag and Cu) and some pieces of Fe, as can be seen in Fig 4.3. The difference in the Fe amount in each target compensates the different sputtering rates of the other elements.

The deposition was performed at the laboratory of the *Departamento de Electricidad y Electrónica of the Universidad del País Vasco*, with the fine help of *Dr. Andrey Svalov*. The system, a commercial *Pfeiffer Vacuum Classic 500*, is equipped with four magnetrons, a substrate holder with 4 slots which can rotate to be placed just on the top of the desired magnetrons, and a rotating chopper to avoid cross-contamination from different magnetrons. The sputtering process was as follows: first high vacuum was reached in the

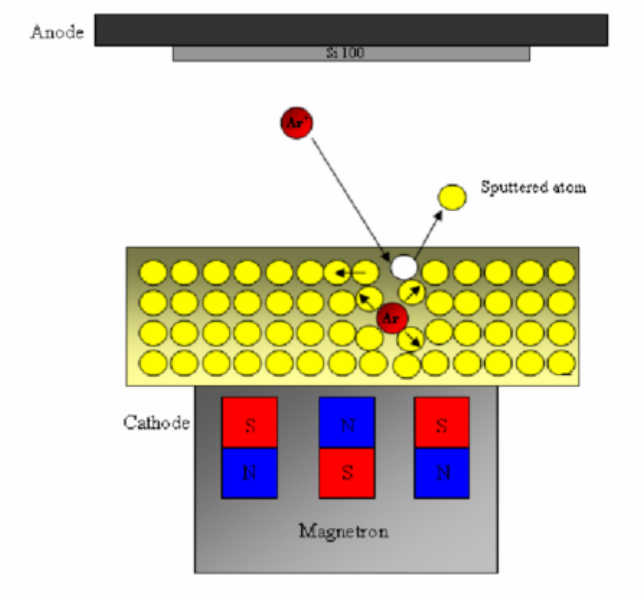

Figure 4.2: *Scheme of a DC-magnetron sputtering chamber. A large voltage is applied between the chamber (anode) and the magnetron plus the target (cathode). Due to this fact, the Ar atoms (working gas) are ionised and accelerated to the target. The free electrons are trapped by the magnetron (an arrange of magnets) magnetic field, helping to sustain the plasma. The collisions of the accelerated Ar^+ ions with the target atoms produce their evaporation. The evaporated atoms are collected on the substrate (Si (100)) over the the magnetron, producing a thin film.*

deposition chamber down to 10^{-7} mbar. Afterwards, the chamber was filled with Ar, with a working pressure of 8.3 x 10^{-3} mbar while the voltage was set to 470 V. The power, P, time, t, and intensity, I, applied were varying from sample to sample (to assure sample homogeneity). A $P = 0.10$ kW, $I = 0.23$ A and $t = 5$ min was used for the Fe_7Au_{93} sample; $P = 0.07$ kW, $I = 0.09$ A and $t = 10$ min for both Fe_7Ag_{93} and $Fe_{14}Ag_{86}$ and $P = 0.10$ kW, $I = 0.25$ A and $t = 5$ min for the Fe_9Cu_{91} films. After each deposition and without modifying the vacuum state (just rotating the substrate disk), a Au coating layer was finally deposited. For all cases the Au coating layer was deposited with $P = 0.06$ kW, $I = 0.31$ A and $t = 5$ s. These parameters were chosen after some trials and taking into account the great experience of *Dr. Svalov*. A feedback process to check the

Figure 4.3: *Targets used in the sputtering process. In the left panel the target for the evaporation of the Fe_7Au_{93} is shown. In the middle, the target for the $Fe_{14}Ag_{86}$ and in the right the one for the Fe_9Cu_{91} samples. The final composition depends not only on the rate of noble metal/iron in the target but also on the different sputtering rates of the elements or the position of the Fe pieces.*

Table 4.1: *Thickness of the deposited films obtained by atomic force microscopy.*

Sample	Thickness (nm)
Fe_7Au_{93}	200
Fe_7Ag_{93}	220
Fe_9Cu_{91}	100
$Fe_{14}Ag_{86}$	142

chemical composition of the films, using a EDX-SEM is continuously performed after the fabrication.

The depositions were made onto Si(100) wafers, with a thickness of 0.5 mm or 0.3 mm and a typical oxide native layer of 10 Å [6], and simultaneously onto a piece of glass with a marked line on it. The printed mark allows an easy removal of the material over it with acetone, so the objective of the deposition on the glass substrate is to monitor the thickness. After removing the material over the mark, we have a piece of film where the edge of the deposition is neat, thus the sample thickness can be measured with an atomic force microscope (AFM). The Si substrate was selected due to its absolute absence of magnetic impurities, and the thickness of the sputtered films is summarised in Table 4.1.

An important issue for the subsequent transmission electron microscopy (TEM) analysis, is to count with electron-transparent samples. The electron transparency is related

to the thickness of the sample (among other parameters), with 100 nm as an upper limit. Also, the shape of the sample is important; a 3 mm disk is needed for the TEM sample holder. In this sense, we have sputtered samples directly onto a Cu grid covered with an electron-transparent film of amorphous carbon, a 30 nm thick film. The other deposition parameters remained unchanged. These grids, commercially available, are commonly used in TEM.

4.3 Annealing

In order to gain a deeper view of the metallic systems, one of the thin film samples has been annealed. The idea behind is to favour the mobility of the atoms/clusters, producing variations of the nanostructure. These variations are related to nucleation processes, usually enlarging the size of clusters [7].

The annealing process has been performed in a quartz tube under high vacuum (less than 10^{-5} mbar, procured by a *Edwars RV8* turbopump) and different annealing temperatures have been applied (50, 100, 150, 200 and 250 °C), until a change in the magnetic response was observed. The annealing time was one hour for all cases. Finally, changes were observed for the films annealed at 200 and 250 °C. In practice, we first achieved high vacuum in the quartz tube outside the oven, while the furnace was set into the desired temperature. When such a temperature was reached inside the furnace, the quartz tube was inserted. The sample temperature was monitored with a thermocouple inside the vacuum chamber and close to the thin film. This assures the sample temperature and allows the control of the time while the thin film was at the desired temperature. This particular parameter was carefully monitored because the heat was mostly transferred by radiation, since the sample is in vacuum. Once the annealing process was over, the vacuum chamber was extracted and the sample was cooled down to room temperature, still under high vacuum.

Bibliography

[1] E. Ma. Alloys created between immiscible elements. *Prog. Mater. Sci.*, **50**:413, 2005.

[2] C. Suryanarayana. Mechanical Alloying and Milling. *Prog. Mater. Sci.*, **46**:1, 2001.

[3] R. García Calderón. *Efectos cooperativos en la relajación magnética de aleaciones nanométricas de Fe-Cu-Ag.* PhD thesis, Universidad de Cantabria, 2005.

[4] Ulf Helmersson, Martina Lattemann, Johan Bohlmark, Arutiun P. Ehiasarian, and Jon Tomas Gudmundsson. Ionized physical vapor deposition (IPVD): A review of technology and applications. *Thin Solid Films*, **513**:1 – 24, 2006.

[5] L. I. Maissel and R. Glang, editors. *Handbook of thin film technology.* McGraw-Hill, United States, 1970.

[6] C. J. Kinane. *The interplay of magnetism and structure in patterned multilayer thin films.* PhD thesis, University of Leeds, 2008.

[7] K. L. Chopra. *Thin film phenomena.* McGraw-Hill, United States, 1969.

Chapter 5

Experimental techniques

In order to fully understand the magnetic behaviour and the influence of the structure at the nanometric scale, a large number of experimental techniques have been used. Among these, structural techniques including diffraction techniques (X-Ray, neutrons or electrons), AC electrical resistivity (varying the temperature and the magnetic field), magnetometry techniques to record the magnetic response (DC-magnetization and AC-susceptibility) and X-Ray Magnetic Circular Dichroism (XMCD) have been extensively employed. In this chapter we will provide a summary of the different techniques and experimental procedures. Note that most of the techniques belong to the *Grupo de Magnetismo de la Universidad de Cantabria* which is in charge of their maintenance. It is worth indicating that a tremendous effort has been concentrated in understanding and running a transmission electron microscope (TEM), focused specifically on magnetic materials. Consequently, some more detail is given for this particular (and sophisticated) technique. Also time was granted to access large facilities beamlines (like the small angle neutron diffractometer D22 at the *Institut Laue-Langevin, ILL*, France or the beamline BL39XU of dedicated XMDC at the *SuperPhoton ring 8 GeV, SPring8*, Japan).

5.1 X-Ray diffraction

The X-Ray Diffraction (XRD) is a widely used structural technique in the solid state physics and in material science. The fact that the X-Ray wavelength is close to the typical interatomic distances (some Å) in the solids, enables the diffraction process. If the structure is crystalline the diffraction will be produced in particular and well-defined angular positions, following the Bragg's law:

$$2dsin(\theta) = n\lambda \tag{5.1}$$

where d is the distance between the crystallographic planes, θ the angle formed by the direction of the incident X-Rays and the crystallographic planes, and λ the X-Ray wavelength [1]. In simple and brief words, the interaction of the X-Rays and the condensed matter is related with the scattering with the electrons, and the intensity of the diffracted peak is proportional to the number of the electrons of the atom (form factor). Additionally, selection rules forbidding some reflections, are present and determined by the symmetry of crystals, which will have an important role in the present work. Two different diffractometers have been used: a *Bruker D8 Advance*, at the *Universidad de Cantabria* and a *Siemens D6000* belonging to the *Rutherford-Appleton Laboratory, RAL.*

5.1.1 Bruker D8 Advance

A *Bruker D8 Advance* (D8 onwards) diffractometer has been used for recording the XRD patterns mainly of powdered samples. This diffractometer operates in a Bragg-Bretano $\theta - \theta$ geometry. In this particular geometry, the sample lays in a horizontal plane and both, the X-Ray tube and the detector move around the sample. Both arms form a θ angle between the X-Ray beam and the sample, guided by a goniometer. The angular range covers (2θ) from 5º to 140º, with a maximum precision of $\Delta 2\theta = 0.0005$º. The diffractometer is equipped with a Cu anode (it is also possible to run with a Mo anode, although it has not been used in the present work), a sample holder and a reception arm with the CCD-detector and a Cu-K_α monochromator. The sample holder (an oriented Si

single crystal or a plastic holder) can rotate in the horizontal plane while the system is measuring. This sample spinning reduce preferential orientations of the resulting pattern. In addition, slits to eliminate non-desired disperse radiation are used. In our particular case with apertures of 1, 1, 0.2 and 0.6 mm.

Figure 5.1: *Bruker D8 Advance. It is a very flexible instrument, with several options, like changing the X-Ray tube or attaching furnaces or cryostats into the sample space.*

5.1.2 Siemens D6000

This diffractometer operates in a different way than the D8, with a $\theta/2\theta$ geometry. It consists of a fixed X-Ray tube, and a mobile (rotating) sample holder and detector. The angular precision of the motors is $\Delta 2\theta = 0.005^{o}$ for the sample holder and $\Delta\theta = 0.0001^{o}$ for the detector arm. The D6000 is also equipped with a Cu-K_{α} tube, a set of slits to collimate the beam and a X-Ray detector.

Figure 5.2: *Siemens D6000 diffractometer sited in the laboratory R53 of the RAL. Its $\theta/2\theta$ geometry is different to the Bruker apparatus.*

5.2 Magnetometry

In the next subsections we will describe the two instruments used for the development of this work, a *Quantum Design MPMS XL SQUID* magnetometer and a *Quantum Design PPMS 6000*. Although the magnetometry of both equipments is based on different physical principles, they share common elements.

Both systems are formed by a metallic cylinder with an approximate diameter of 0.5 m

and 1.5 meters tall. Inside this cylinder there is a dewar with liquid He. The liquid He has a double function: to refrigerate the superconducting elements below their critical temperature and to cool down the sample. The liquid He allows the magnetometer to operate in a temperature range from 2 to 350 K. Inside the dewar, there is a superconducting coil which generates the magnetic field. On top of the cylinder there is an aperture to allow the insertion of the samples. This is assured by attaching the sample to a long rod, which is length-calibrated to place the specimen inside the detection system. The rod present a top end that allows the sealing of the dewar. The physical detection system is also inside the dewar. However, the electronics that control the equipment (temperature, magnetic field or the measuring system) are in a supplementary cabinet. In both magnetometers the electronic is controlled by a computer, but the QD PPMS can be controlled directly with a front-end panel.

5.2.1 SQUID magnetometry

A SQUID (Superconducting QUantum Interference Device) is currently the most precise detector of magnetic fields (down to 10^{-7} emu in optimal conditions). We have used a QD-MPMS XL 5T (Fig. see 5.3). It is composed by a superconducting ring with one or two Josephson junctions. In standard measurements, when a magnetic dipole moves perpendicular to the SQUID surface, a tunneling current through the Josephson barrier is produced. The generated current is proportional to the dipole size. The SQUID is also capable of measuring AC susceptibility χ_{AC}. This is achieved by applying a small oscillating magnetic field with a determined frequency ω, and measuring the time response. Then the AC susceptibility $\chi(\omega) = \chi' + i\chi''$ can be obtained. The critical (maximum) field of the superconducting coil is $H = 50$ kOe, and includes a system to quench the coil above its critical temperature, in order to remove any remanent magnetisation.

The SQUID has been used to measure the thin film samples, due to the extremely (and challenging) small signal. The use of such an equipment is a must: in addition to the low ferromagnetic content, a very low amount of sample was available (10^{-6} cm^3, typically). Moreover a special care has been put in the sample mounting, and additional

considerations to allow a proper measurement have been taken into account. To place the sample in the dewar, it is used a large (commercial) rod and a plastic straw where the sample is inserted. For powder samples, a capsule that fits perfectly in the straw is used. However, in the case of the thin films, a less standard procedure has to be figured out. Firstly a piece of rice paper without magnetic impurities and with dimensions of the straw is cut. Afterwards, a piece of the film was glued to the paper with a drop of low temperature varnish *IMI insulating varnish 7031*. Once the film was fixed to the paper, the sample support was placed in the straw and subsequently into the sample rod. Usually, if the magnetic response of the sample is high enough, the raw data provided by the MPMS are taken as the magnetic signal. However in our samples, the diamagnetic contribution from the Si substrate plays an important role since the mass of the substrate is three orders of magnitude higher than the sample mass. For the rest, the diamagnetic contribution of the varnish drop is ignored, and the diamagnetic signal of the paper and the straw has not a significant effect since the integrated signal among the detection coil is negligible.

Figure 5.3: *QD-MPMS XL 5T sited in the Universidad de Cantabria. All the magnetic properties of the thin films have been acquired in this equipment.*

5.2.2 PPMS magnetometer

The *QD-PPMS* is a very versatile system, which can measure specific heat, electrical resistivity (as we will see in the next section), DC magnetometry and AC susceptibility in different conditions of magnetic field and temperature. Our PPMS (Fig. 5.4) system incorporates a superconducting coil with a critical field of $H = 90$ kOe, and is equipped with a He liquefier (*Evercool* system) [1]. The DC magnetic signals are measured by a secondary set of coils, based on Faraday's induction law: the sample is moved quickly up and down through the secondary coils, and the induced current is then measured. The AC susceptibility is obtained again applying a small and oscillating magnetic field (h) and measuring the time dependence of the induced current with a lock-in detection. The PPMS was used to measure the powder samples as the sensitivity (10^{-5} emu) is low for the films. The sample mounting was much easier: put the powder in a capsule and fix it with cotton to avoid the movement. Then, the capsule is inserted in a plastic straw, and the straw in the sample holder. Due to the large signal of the powdered sample (much more mass available) it is not necessary to correct the capsule diamagnetic contribution.

Figure 5.4: *QD-PPMS 9T sited in the Universidad de Cantabria. This system has been used to measure the resistivity of the films and the magnetic properties of the powdered alloys.*

[1] It consists in a cryocooler-dewar system that recondenses and liquefies gaseous helium directly within the dewar.

5.3 AC electrical resistivity

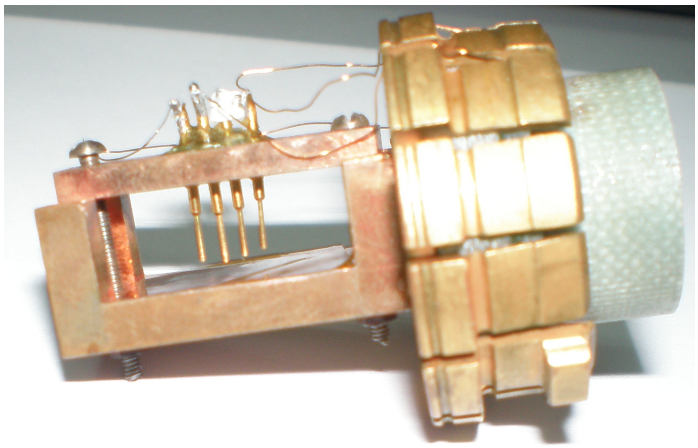

Figure 5.5: *Home-made four points contact. The needles have a spring inside to assure the contact.*

As it was commented in the section 5.2.2, the PPMS allows to perform electrical resistivity measurements. The selected contacts follow a four point geometry, with two contacts for the voltage (inside) and the two others for the current (both ends). The samples were mounted aligning the magnetic field direction with the in-plane direction of the film. Initially, we tried silver paste to assure the electrical contact. However, this method proved to be unefficient with some films, providing non-repetitive measurements due to the poor fixing of the contacts onto the film. Gold microsoldering was another available possibility, but was discarded because of the possible effect of the temperature on the film micro/nanostructure. To overcome this problem we designed a sample holder (see Fig. 5.5). This holder has four retractile contacts with a small spring inside. This perfectly suits our needs, since the films present an even surface. The needles were fixed with an insulating epoxy.

5.4 Atomic force microscopy

The atomic force microscope (AFM) was uniquely employed to measure the films thickness. The use of this technique was extremely limited and performed by *Dr. J. Alonso* and *Dr. A. Svalov* at the *Universidad del Pais Vasco*, thus the description is necessarily reduced. The AFM used in this work is a commercial *Nanotech DSP classic*. The AFM consist of a tip (cantilever) perpendicular to the surface to measure. The cantilever oscillates in a natural frequency, but its interaction with the material modify the tip frequency. This change of frequency reflects the profile of the sample, and consequently, the thickness of a step can be measured.

5.5 Electron microscopy

In optical microscopes, the angular resolution is limited by the light wavelength. Shortly after the formulation of the wave-particle duality by *Louis-Victor de Broglie* [2], *E. Ruska* and *W. Knoll* used the short wavelength of highly accelerated electrons in a beam to effectively set up an electron microscope. For example, with an energy of 100 keV, the associated wavelength is of $\lambda \sim 4$ pm, much lower that the atomic radius. The e^- beam trajectory is modified by using electromagnetic lenses, that is, a set of Cu coils inside Fe pole pieces. However, the quality of the electromagnetic lenses is really poor in comparison with the light lenses. As an example, the first electron microscope, in 1931, did not reach better angular resolution than a state-of-the-art light microscope. With time, electromagnetic lenses have improved notoriously, and now standard electron microscopes provide a point resolution of tenths of Å. Two different kinds of electron microscopes have been used in this work, a scanning electron microscope (SEM) and a transmission electron microscope (TEM). Although both kinds of instruments use electrons as probe, they are quite different, as we will see in the following.

5.5.1 Scanning Electron Microscope

The SEM is commonly used to characterize the surface of materials. The sample preparation for the microscopy is relatively easy for conducting samples, and usually, just a metal coating is needed for insulating ones (gold for high quality images and metallised carbon for elemental analysis). The reason for this is that for no-conducting materials the surface could be charged by the incoming electrons, producing artifacts in the image. The SEM image is usually formed with backscattered electrons: the electrons are accelerated, hit the sample, some of then are backscattered and a electron detector collects them. It is called "scanning" because the electrons are focused on a small probe and consequently, the beam is rastered. Taking advantage of the X-Ray dispersive energy spectrometer attached to the SEM (a relatively common complementary instrument), our interest was focused on the chemical composition of the samples. The X-Ray spectroscopy consists in the detection of the energy of the X-Rays arriving to the detector emitted by the sample. In a very oversimplified explanation the incident electrons have enough energy to excite core electrons and in the decay, the energy of the X-Rays are characteristic of the element. Counting the number of the photons at each energy channel of the detector, the relative concentration of the elements present in the sample can be quantified. The instrument used in this work was a *Jeol JSM 5800LV* equipped with a *EDX Oxford link XL* sited at the department *LADICIM Universidad de Cantabria*.

5.5.2 Transmission Electron Microscope

The transmission electron microscopy is very different from the SEM. The basic issue in TEM, is that the electrons that the image is formed by the transmitted electrons, instead being formed by the backscattered ones. Due to the large electron-electron interaction, the sample should be very thin (less than 100 nm) to allow electrons pass through. This requirement results in quite challenging experimental work related to the sample preparation. In this section we will describe the elements and operation modes of a typical transmission electron microscope, the alignment steps needed to take quality pictures and

the sample preparation selected in our work.

5.5.2.1 The instrument

The main component of the TEM (in our case a *Jeol JEM 2100* with an *INCA x-sight* EDX system, LaB_6 filament and a Gatan *Orius SC1000* digital camera, see Fig. 5.6) is the vacuum column were all the elements are inserted. Beginning from top to down, we find the electron gun (where electrons are generated and accelerated to the working voltage), the illumination system (where the electrons are controlled before the sample), the image system (electromagnetic lenses and apertures) and the image acquisition system (photographic paper or a CCD camera nowadays). The sample is inserted after the illumination system and before the image system.

Figure 5.6: *TEM used in the present study. At the left panel it is shown a JEOL 2000FX, at the middle a JEOL 2010 (both from the Imperial College, London), where at the right panel a Jeol JEM 2100 which belongs to the Universidad de Cantabria. Most of the work has been performed in the latter microscope.*

There are basically two kinds of electron sources: thermoionic and field emission (FE). The first emits the electrons when they are heated up (to around 1700 K for a LaB_6 crystal), and the second ones when an intense electric field is applied, at room temperature. The thermoionic sources are cheaper, but the electrons emitted have a wider energy distribution and a larger crossover (see below). The idea behind the thermoionic sources is that for any material at high enough temperature, the thermal energy of the electrons is greater than the attractive potential of the nucleus. Richardson's law relates the current

density of the emitted electrons with the temperature of the material [3].

$$J = AT^2 e^{-\frac{\phi}{k_B T}} \tag{5.2}$$

where J is the current density from the source, T the temperature, ϕ the work function, k_B the Boltzmann's constant and A the Richardson's constant (A/m^2K^2). We can see from equation 5.2 that the higher the temperature or the lower the work function, the greater the current density. For this reason, the materials for thermoionic sources usually are materials with a high melting point (like W) and with a low ϕ (like $\phi = 2.7eV$ for the LaB_6 [4]). In our particular case, the microscope at the *Universidad de Cantabria* is equipped with a LaB_6 filament. The LaB_6 has better characteristics than the W sources, like more brightness, less energy spread or greater lifetime. Once that the electrons are emitted, we need to drive them into the illumination system, as well as to accelerate to the velocity corresponding to the working voltage (V = 2.086 x 10^8 m/s) at 200 KV. A large potential is applied between the cathode (the electron source) and the anode (with a hole in the centre to allow the electrons to pass trough). Before the anode, there is another component, the Wehnelt cylinder. The Wehnelt is a "grid" with a negative applied potential [3], used to control the e^- beam. Due to the small negative potential of Wehnelt, all the electrons converge to a point called "crossover", with a characteristic size, around 10 μm for a LaB_6 filament [3].

Once the electrons move at the desired velocity, they will cross through a set of electromagnetic lenses and apertures to manipulate the electron beam. Modern microscopes are constituted by several lenses, which can be grouped into two main categories: *illumination system* and *image system*. The so-called *illumination system* is composed, in a simple scheme, by an arrange of two condenser lenses (one and two) and the condenser aperture. The aim of the illumination system is to control the way that the electrons reach the sample. The first condenser lens (C1) is used to demagnify the crossover from the Wehnelt [4], achieving a finer electron beam than produced by the Wehnelt alone. The purpose of the second condenser lens (C2), is to modify the electron beam shape. Varying the strength of the C2 lens, the electron beam can be focused as a very fine spot

or spread the electrons into a large and parallel beam. Finally the condenser aperture is used to chop off the electrons with a large illuminating angle. The idea is that the larger the illuminating angle the greater the aberrations (spherical and chromatic, for instance).

After the *illumination system*, the electrons will pass through the sample, arriving to the *imaging system*. In a simplified scheme this is composed by three lenses: objective lens, intermediate lens and the projection lens (although, as it was mentioned before, in modern microscopes is much more complicated) and two apertures: objective aperture and selected area diffraction (SAD) aperture. The strength of the lenses and the use of the apertures will depend on the work to be done: imaging or diffraction. For diffraction, the back focal plane of the objective lens acts as the object plane for the intermediate lens [3]. However, to get an image, the strength of the intermediate lens will be changed to make the image plane of the objective lens match with the object plane of the intermediate lens. In both cases, after the intermediate lens, electrons will be projected on the CCD or viewing screen by the projection lens. Usually, for diffraction, a SAD aperture is used. It is placed in the objective image plane, and selects the part of the image where the diffraction will be extracted. For instance, the objective aperture (in the back focal plane of the objective aperture) is used in most of the image processing, in both bright field (BF) and dark field (DF) image, but not for high resolution TEM (HRTEM). A summary scheme (from [3]) can be seen in Fig. 5.7.

Finally, the image acquisition system consist of a viewing screen and a recording element. The viewing screen is a plate coated by a material that convert the arriving electrons into visible light, like ZnS. The recording element are CCD cameras and photographic papers. Although the photographic papers have higher resolution, CCD cameras are much more common nowadays. Obviously, the main advantage is obtaining the final image almost in real time and much easier post processing.

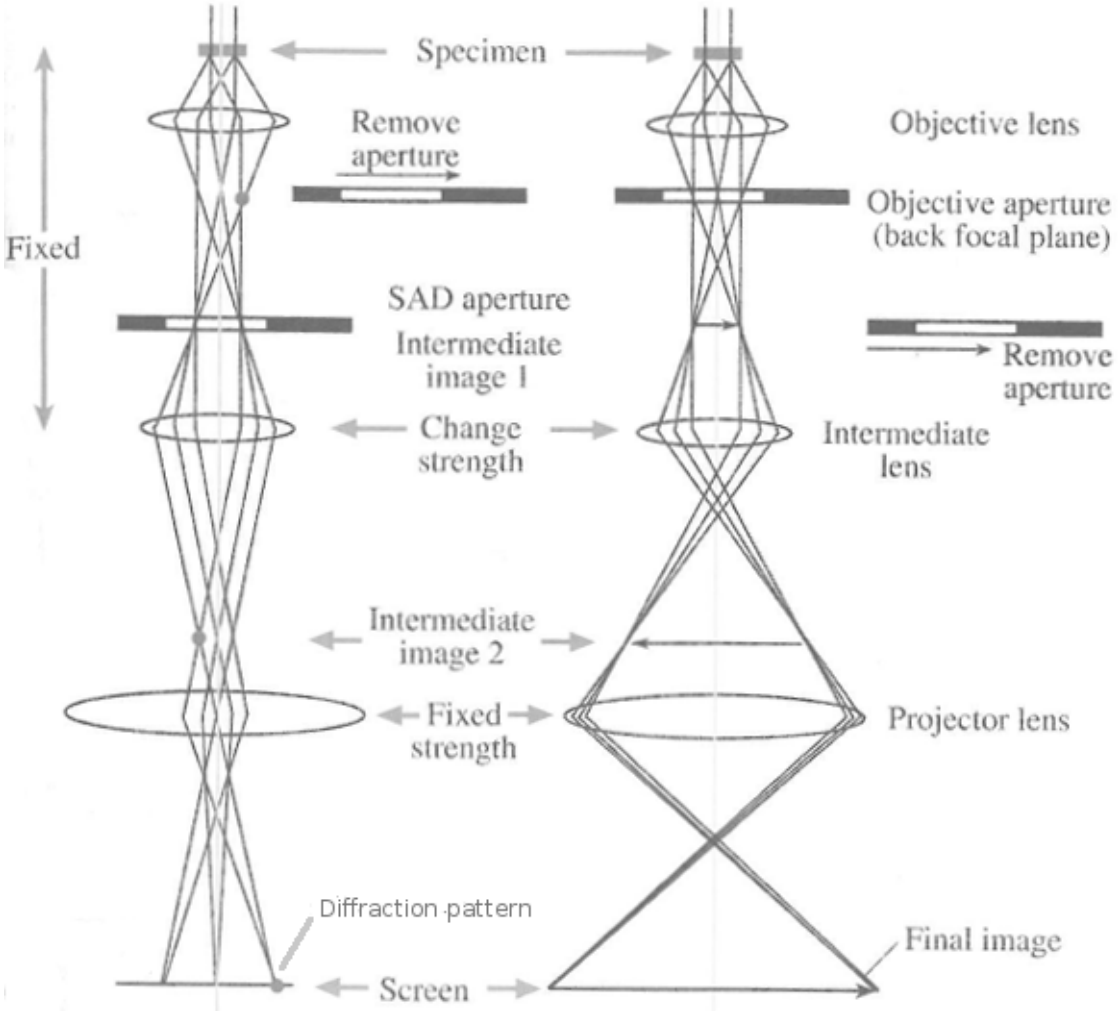

Figure 5.7: *Scheme of the two basic operations of the TEM imaging. The left panel represent the system operating in the diffraction mode, where the right one represents the image mode.*

EDX detectors are also available in most of the modern TEM, including the one at the *Universidad de Cantabria*. The basis of the technique is the same briefly exposed in SEM section (5.5.1), but just being aware of the size of the sample which is analysed. While in SEM we can use the EDX as a way to characterize the overall composition, in TEM, the EDX is used to check the chemical composition of particular features of the sample (or image).

In addition to the described equipment, modern TEMs (and also the microscope used in this work) offer the option to operate as a scanning TEM (STEM) which will be

described below. Additional elements (deflection coils) are needed to focus the e^- beam and move it across the sample are sited after the C2 lens. The transmitted electrons are collected by e^- detectors, before the CCD camera. This microscopy has two main appeals: firstly, the synchronisation of the e^- beam with other detectors (like a EDX or electron energy loss spectrometer) add spatial resolution to the information, allowing the composition of maps. The second one is that the electrons highly deflected produce images with a contrast proportional to the Z number, making negligible the diffraction contrast.

Before the beginning of any TEM session, a careful alignment of the equipment must be done. Since a TEM have such a great resolution, any perturbation in the ideal working conditions implies a loss in the resolution. Parameters like ambient thermal gradients during the session, noise or fluctuations in the current are critical in order to get good quality images. Also a precise alignment of the electron optics is necessary to get the best performance of the microscope. It is a routinary work that must be re-checked from time to time, and include tasks like aligning the apertures with the optical axis, setting the sample in the *eucentric* plane, correcting the astigmatism or focus the sample. It will not be described, since little physical insight of the microscope is earned and most of the users, perform it in a mechanical way. In these sense, it is worth to remark the help and teaching of *Prof. David McComb and Dr. Mahmoud Ardakani* of the department of materials of the *Imperial College*, London and *Dr. Lidia Rodríguez* from the SERMET of the *Universidad de Cantabria*.

5.5.2.2 Operation modes

Different possibilities are available in a TEM. Now we will describe the TEM experiments performed in this work, excluding other technical options.

5.5.2.2.1 Diffraction Electron diffraction is a very powerful technique to resolve the microstructure of a system and to identify compounds. As was described previously, a TEM can record e^- diffraction patterns. With the image at the viewing screen, the SAD

aperture is inserted to select the region of interest. Four different aperture diameters are available in the Jeol 2100 FX: 100, 50, 20 and 10 μm of diameter. Finally the e^- diffraction pattern can be recorded with the CCD-camera or the photographic paper.

5.5.2.2.2 Imaging Two main types of imaging are typically used: bright field (BF) or dark field (DF) image. Without the objective aperture, the image will be formed by the transmitted beam plus all the diffracted electrons (diffraction contrast), yielding to a poor contrast image. However, introducing the objective aperture some diffracted e^- can be chopped off. Once the region to image is selected, and in the diffraction mode, the objective aperture is inserted. Then, the objective aperture is placed, allowing the pass the direct beam, but absorbing diffracted electrons. This is called bright field image, and improves the contrast of the image. We can also move the objective aperture allowing some diffracted electrons go through the column and excluding the direct beam so the image will be formed with the diffracted electrons of the selected spot. This is very useful to observe the distribution of precipitates or different phases. This is the basis of dark field imaging. In this particular instrument, the sizes of the objective apertures are 120, 60, 20 and 5 μm.

5.5.2.2.3 HRTEM BF and DF image can not form a HRTEM image (which allows the observation of atomic columns). This is because the contrast in a HR image is given by phase contrast, that is, the contrast formed by the difference of the optical path of different electrons. This implies that at least the direct beam should be used as reference in combination with one diffraction spot to allow the interference process. Following ref. [4] the diffracted electron wavefunction, $\psi(\boldsymbol{\Delta k})$ is the Fourier transform of the scattering factor distribution in the material, f($\mathbf{r}$), which follows the atom arrangement in the material.

$$\psi(\boldsymbol{\Delta k}) = \frac{1}{\sqrt{2\pi}} \int_{-\infty}^{\infty} f(\boldsymbol{r}) e^{-i\boldsymbol{\Delta k r}} d^3\boldsymbol{r} \tag{5.3}$$

$$f(\boldsymbol{r}) = \frac{1}{\sqrt{2\pi}} \int_{-\infty}^{\infty} \psi(\boldsymbol{\Delta k}) e^{+i\boldsymbol{\Delta k r}} d^3\boldsymbol{\Delta k} \tag{5.4}$$

From 5.4 it can be deduced that a calculation of the Fourier transform for $\boldsymbol{\Delta k}$ from $-\infty$ to $+\infty$ is required to obtain the full information about the $f(\boldsymbol{r})$. Unfortunately the objective aperture truncates the $\boldsymbol{\Delta k}$, since not all the reciprocal space is available, as it is common for scattering in neutron and X-Ray experiments, so the resolution of the image is reduced. An estimate of the resolution is given by:

$$\delta x \simeq \frac{2\pi}{\delta k} \tag{5.5}$$

where δk is the k range selected by the objective aperture. Assuming δx equal to the typical interatomic distance, it is easily found that a k-range of the order of the first diffraction spot is needed, much large than the typical k-range allowed for a BF/DF objective aperture. Nevertheless, even without an objective aperture, there are other issues that could prevent a HR image. In this sense, δk is also especially sensible to the spherical aberration, and thus working without an objective aperture, does not warrant reaching a high resolution image.

5.5.2.2.4 STEM In the STEM mode the e^- beam is focused into a very fine probe (from 10 to 1 Å) and rasters the sample surface like in a SEM, but the image is still formed with transmitted electrons. One of the main applications is the possibility of recording compositional maps: the EDX detector is synchronised with the e^- beam and the composition of each point can be measured. However, the spatial resolution is limited by the beam size which is related with the crossover of the e^- in the gun (see subsection 5.5.2.1). Conventional BF imaging with transmitted electrons can be also performed. Moreover, electrons scattered to a very large angle can be equally collected and imaged with a *High Angle Annular Dark Field* detector. This is a technique that composes images with a contrast proportional to the Z number of the element, since at large angles the scattering mostly depends on the thickness of the sample and the Z number (Rutherford scattering) [4].

5.5.2.3 Sample preparation

The sample preparation for TEM is a demanding process. The ideal TEM sample is representative, thin, clean, flat, parallel-sided, conductive, free from segregation and self-supporting [5]. However, it is difficult (almost impossible) to achieve all these conditions simultaneously. The most important of those requirements is the representative: if the specimen for the TEM is not representative of the whole sample the obtained conclusions will be wrong. In our particular case we analysed TEM results of thin film samples. The main work was performed on thin layers deposited onto an amorphous carbon grid (only varying the time of deposition to obtain e^- transparency in the sputtering parameters). We will also describe the steps followed to obtain images from the samples deposited on a Si substrate. To prepare our samples deposited onto Si is a manual procedure, so there is a big chance of breaking the sample during the preparation process due to their brittle nature. The final shape of the films to be inserted in the TEM sample holder are 3 mm diameter disks with a region with a thickness low enough to allow the e^- transmission.

The details of the procedure are extremely important and frequently ignored in the literature. In the following, we will give details starting from the raw conditions of the film, just after it has been sputtered. Firstly the 3 mm disk needs to be cut. An ultrasonic disk cutter (*Gatan ultrasonic disk cutter 601*) is used to obtain a 3 mm Si disk. Basically, it contains a ultrasound generator and a cutting tool attached to it. The sample is glued with a low melting-temperature wax (*Electron Microscopy Sciences mounting wax 70*) on a glass slide and, subsequently, the glass is also glued onto a metallic base. The base has a spring and so, while the material is being cut, the spring pushes up the sample and the contact between the cutting tool and the sample is permanent. Additionally to that, a dispersion of SiC in water is needed to cut away the disks. The penetration depth of the cutter tool can be followed by a micrometer attached to this instrument. Incredibly, the most accurate way to know if the cutting is finished is the neat change of the sound when the glass begins to be cut!

Once the 3 mm disk is cut, the thinning process can be initiated. All the thinning process must be performed over the Si side, since the sample itself is only some nm thick

and any polishing attempt will destroy it. The first step is to thin the Si substrate (300 or 500 μm thick depending on the Si batch) in a homogeneous way, down to 100 μm approximately. This thickness has been selected because a 100 μm Si disk is resistant enough for further handling. For the process, the sample has been glued with wax to a plane metallic cylinder, which fits perfectly into a hole made in a flat metal grinder. There is a screw in the grinder that allows to tune the depth of the hole with an accuracy around 10 μm. It is important to align the sample surface with the flat surface of the grinder. In this sense, we put the sample surface well below the grinder surface. After it, a drop of water was deposited on the sample, and a glass slide on the grinder surface. Then, we begin to rise the sample slowly. When the drop of water begins to self-deformed by the contact with the glass slide, the sample will be roughly aligned with the grinder. Once the sample is aligned, we turn the grinder screw the desired depth to thin, and polish it with SiC paper, trying to perform it in a homogeneous way. The grinder should follow a path with a shape of an eight, and care should be putted on make it clock and anticlockwise.

Once the final thickness is achieved, the sample should be dimpled (that is, to thin more the sample in the middle with a shape of a half moon) with the aid of a *Gatan dimple grinder 656*. The depth of the dimple is related to the mechanical properties of the sample. In the case of a Si substrate a dimple of 70 μm in a 100 μm has proved to be stable. For the dimpling process, the sample should be waxed again in a metal cylinder. A rotating wheel with a limit lays over the sample. The limit is set with the aid of the micrometer in the depth that is desired to remove. Once the depth to dimple is set, diamond paste is placed on the sample and, the wheel begins to spin allowing the dimpling process. When the micrometer reaches its limit, the grinding wheel has come to an end. Again, the dimpling depth will be greater in the beginning, evolving to smaller steps towards the end.

The last step is the ion polishing (*Gatan PIPS 6 keV 691*). The ion polishing technique accelerates Ar^+ ions hitting the sample to produce a sputtering process which allows the removal of the material. The ion energy can be tuned from 500 eV to 6 KeV, and depends

on the sample, which is also spinning to assure an homogeneous hole. The ion polishing time depends on the remaining thickness of the substrate, therefore it is important to remove as much sample as possible with the mechanical methods. The ion polishing will be followed until a hole is present in the sample. Such a hole procures a region with a thickness below the 100 nm needed for the e^- transparency. In our particular case, the energy of the Ar ions was 4 KeV, the polishing angle 4.5 º and a typical time (varying from sample to sample due to thickness differences) of 2 h. Also, if the e^- transparent region is too small, we can try to polish the actual film with a lower angle. It is a risky process, since the e^--transparent region can be destroyed. It is important to remark that the ion polishing process is a very specific process depending on the material. The selected energy and angle, as well as other parameter in the sample preparation, like the Si thickness were chosen based on the experience of the *Dr. M. Ardakani*, of the *Imperial College, London.*

5.6 Polarised small angle neutron scattering

The neutrons are a typical probe for studying the matter. Because their lack of electric charge, the main interaction is by nuclear forces. Also, the neutrons are fermions, so a magnetic dipole is present. This fact makes that neutrons interact with magnetic fields, which obviously is very interesting for magnetic materials. In our particular case Small Angle Neutron Scattering (SANS) has been performed at the *Institut Laue-Langevin* in Grenoble. The SANS technique gives information about inhomogeneities in materials with a characteristic length in the order of tens to hundreds of Angströms [6]. The inhomogeneities can be structural, magnetic or both, since, as was previously said, the neutrons interact with the magnetic fields.

A conventional SANS experiment consist of a neutron beam arriving parallel to the sample and a large circular neutron detector. Usually, SANS experiments are carried out with cold neutrons (since we want to get information about large structure large wavelengths are better, $\lambda \sim 8$ Å), and the distance from the sample to the detector is large, considering that the larger sample-detector distance the smaller angle scattering.

In addition, the incoming beam can be polarised (using a supermirror in our case), and a spin flipper to change the neutron polarisation. The use of polarised neutrons give an extra contrast for the magnetic impurities: the angular dependence of the scattering is negligible in the detector direction forming 90° with the magnetic field, if the magnetic field direction and the spin of the neutrons are aligned (see Fig.5.6).

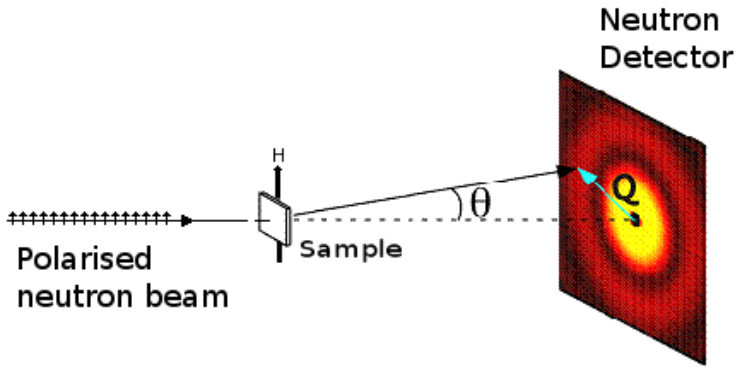

Figure 5.8: *Scheme of a polSANS experiment. The polarised incident neutrons reach the sample, where a static magnetic field is applied. After going through the sample, the scattering is recorded on a 2D detector. The nuclear part of the scattering does not depend on the applied field. However, the magnetic scattering does, so changing the relative orientation of the neutrons and the applied field, a neat contribution of the magnetic scattering can be obtained, and hence, information about the magnetic particles.*

The SANS experiment was performed at the instrument D22. The samples were mounted in an orange cryostat, with a temperature range between 1.5 K to 320 K. A set of coils could be used to generate a magnetic field up to $H = 8$ kOe. The wavelength used was 8 Å and the distance from the sample to the detector varied from 2, 8 and 17 m, to achieve the widest *q-range* available. Despite the experimental efforts, we were not

able to record the SANS signal of our samples. Due to the absence of actual results, we will not extend further the description of this very powerful and interesting technique.

This absence stems from the small thickness of the films. Some trials were performed during the beamtime available but finally this exigent experiment might need a better choice of the sample condition for the technique.

5.7 X-Ray Magnetic Circular Dichroism

5.7.1 Origin of the XMCD

5.7.1.1 Basics

Electron core energy levels of different elements are characteristic, and for transition metals lay in the range of the keV, as it was commented on section 5.5.1. Seizing this advantage, element selective spectroscopy can be performed with X-Rays in such an energy range. At high photon energies, the dominant process in the electromagnetic radiation-matter interaction is the photoelectron absorption. As a result, the energy of the incoming X-Rays will be absorbed by an electronic excitation, following the Beer-Lambert-Bouguer law [7]:

$$I = I_0 e^{-\mu x} \tag{5.6}$$

where I is the intensity after the sample, I_0 is the incoming intensity, μ is the absorption coefficient and x is the sample thickness. μ varies continuously with the energy, except when the X-Ray energy matches the core-energy levels, where rises drastically, since the photon will excite an electron from this core level to an unoccupied state. Usually, the transition probability will follow the Fermi's Golden Rule:

$$W = \frac{2\pi}{\hbar} | < f|H_{int}|i > |^2 \rho_f(\hbar_\omega - E_c) \tag{5.7}$$

where $|f>$ is the electron final state, $|i>$ is the initial state, H_{int} is the matrix element of the electromagnetic field operator between $|i>$ and $|f>$, $\rho_f(E)$ is the density of empty states at the energy E above the Fermi level and E_c is the energy of the excited electron.

Two main approximations are commonly used: the photo-absorption is a single electron process (that is, all the electrons of the system remains unaltered with the exception of the photo-excited electron), and the electric dipolar interaction is the responsible of the excitation. This implies that:

$$| < i|H_{int}|f > | \propto | < i|\epsilon \cdot \boldsymbol{r}|f > | \tag{5.8}$$

with ϵ the polarisation vector. The symmetry of the dipolar operator, leads to the electric dipole selection rules:

$$\Delta l = \pm 1 \text{ and } \Delta s = 0 \tag{5.9}$$

where Δl and Δs are the variation of the l and s quantum numbers among the initial and final electron state. In addition, when the incoming X-Rays are circularly polarised, another selection rule should be taken into account, due to the angular momentum that carry circularly polarised photons, depending on the helicity of the X-Ray:

$$\Delta m_j = \pm 1 \tag{5.10}$$

with the + sign for right circularly polarised light and the - for the left polarised light. X-Ray magnetic circular dichroism (XMCD onwards) is defined as the difference between the X-Ray absorption coefficient for both polarisation: XMCD = (μ^--μ^+). The magnetic information carried by the XMCD is thank to this additional selection rule. G. Schütz *et al.* [8, 9] propose the two step approach in order to understand the dichroism. The first step is the excitation of the core electron produced by a polarised X-Ray. In absence of spin-orbit coupling of the core-electrons, both left and right circularly polarised light (LCP and RCP respectively) will excite 50% of spin up and 50% of spin down electrons. When a spin-orbit coupling is present, the X-Ray can partially transmit its angular momentum to the electron spin. It will produce an actual spin polarisation in the excited photo-electron. Due to the Pauli exclusion principle, the photo-electron will probe the spin polarisation of the final state. This is the second step, which provides the magnetic properties of the sample.

If we name $\mu^+(E)$ the absorption produced by RCP light and $\mu^-(E)$ the absorption of the LCP light at a certain energy E, the transition probability will be:

$$\frac{\mu^- - \mu^+}{\mu^- + \mu^+} = P_e \frac{\Delta\rho}{\rho} \tag{5.11}$$

where P_e is the electron polarisation (Fano parameter), $\Delta\rho = \rho\uparrow - \rho\downarrow$, being $\rho\uparrow$ and $\rho\downarrow$ the majority and minority-like final state densities. In this particular work, the dichroism has been performed in the Au $L_{2,3}$ edge (transitions from 2p→3d states). Concretely, the L_3 will excite the $2p_{\frac{3}{2}}$ where the L_2 will promote the $2p_{\frac{1}{2}}$ electrons. If the Stoner model is used, the $3d$ states will not present a spin-orbit coupling, but the exchange interaction will split the band into spin-up and spin-down sub-bands. This will made five spin-up ($\rho\uparrow$) and five spin-down ($\rho\downarrow$) density of states (DOS).

The main interaction mechanism of the incoming X-Rays with the electrons is the dipolar. The dipolar operator, expressed in terms of spherical harmonics is:

$$\epsilon \cdot \mathbf{r} = \sqrt{\frac{4\pi}{3}} Y_1^1 \cdot r \quad \text{for RPC light} \tag{5.12}$$

and

$$\epsilon \cdot \mathbf{r} = \sqrt{\frac{4\pi}{3}} Y_1^{-1} \cdot r \quad \text{for LPC light} \tag{5.13}$$

The dipole operator does not act on the spin-state, so the matrix elements can be written in a $\mid l, m_l, s, m_s\rangle$ basis set. The dipolar selection rules states that the $2p$ with $|l, m_l\rangle$ state will transit to the $3d$ $|l+1, m_l \pm 1\rangle$ state. The possible matrix elements are obtained from:

$$\sqrt{\frac{4\pi}{3}} \langle l+1, m_l \pm 1 \mid Y_1^{\pm 1} \mid l, m_l\rangle R = -\sqrt{\frac{(l \pm m_l + 2)(l \pm m_l + 1)}{2(2l+3)(2l+1)}} R \tag{5.14}$$

where the radial part is given by:

$$R = \langle n', l+1 \mid r \mid n, l\rangle \tag{5.15}$$

is assumed constant for the considered transitions. On the order hand, the angular part:

$$I_{jm}^{\pm} = \left| \sqrt{\frac{4\pi}{3}} \langle j', m \pm 1 \mid Y_1^{\pm 1} \mid j, m\rangle \right|^2 \tag{5.16}$$

Table 5.1: *The angular part of the matrix elements for excitations from 2p core levels* $\mid jm_j\rangle$ *decomposed into* $\mid l = 1, m_l, s = 1/2, m_s\rangle$ *and catalogued with respect to spin and circular polarisation of light.*

j, m_j	m_l, m_s	I^+	I^-
$\frac{3}{2}, +\frac{3}{2}$	$\mid +1\uparrow\rangle$	$(\frac{2}{5})\uparrow$	$(\frac{1}{15})\uparrow$
$\frac{3}{2}, +\frac{1}{2}$	$\sqrt{\frac{1}{3}}\mid +1\downarrow\rangle + \sqrt{\frac{2}{3}}\mid 0\uparrow\rangle$	$(\frac{2}{15})\downarrow + (\frac{2}{15})\uparrow$	$(\frac{1}{45})\downarrow + (\frac{2}{15})\uparrow$
$\frac{3}{2}, -\frac{1}{2}$	$\sqrt{\frac{2}{3}}\mid 0\downarrow\rangle + \sqrt{\frac{1}{3}}\mid -1\uparrow\rangle$	$(\frac{2}{15})\downarrow + (\frac{1}{45})\uparrow$	$(\frac{2}{15})\downarrow + (\frac{2}{15})\uparrow$
$\frac{3}{2}, -\frac{3}{2}$	$\mid -1\downarrow\rangle$	$(\frac{1}{15})\downarrow$	$(\frac{2}{5})\downarrow$
$\frac{1}{2}, +\frac{1}{2}$	$\sqrt{\frac{2}{3}}\mid +1\downarrow\rangle - \sqrt{\frac{1}{3}}\mid 0\uparrow\rangle$	$(\frac{4}{15})\downarrow + (\frac{1}{15})\uparrow$	$(\frac{2}{45})\downarrow + (\frac{1}{15})\uparrow$
$\frac{1}{2}, -\frac{1}{2}$	$\sqrt{\frac{1}{3}}\mid 0\downarrow\rangle - \sqrt{\frac{2}{3}}\mid -1\uparrow\rangle$	$(\frac{1}{15})\downarrow + (\frac{2}{45})\uparrow$	$(\frac{1}{15})\downarrow + (\frac{4}{15})\uparrow$

is listed in Table 5.1. For the L_3-edge the RCP light favors the excitations of the spin-up electrons, contrary to the situation for the L_2-edge.

If the DOS of both sub-bands (spin-up and spin-down) of the 3d level is equal, both absorptions (μ^+ and μ^-) will be equal. However, materials with a net magnetisation present an unbalanced population of the sub-bands, and hence a dichroic signal due to the different transition probability from both light polarisations, as it is seen in Table 5.2.

Table 5.2: *The X-Ray absorption for RCP (LCP) light involves preferentially spin up (spin down) electron on the* $2p_{3/2}$ *core level (*L_3*-edge). The opposite situation is observed for the* $2p_{1/2}$ *(*L_2*-edge).*

	I^+	I^-	$\Delta I(\propto XMCD)$
L_2	$\frac{1}{3}\rho\downarrow + \frac{1}{9}\rho\uparrow$	$\frac{1}{9}\rho\downarrow + \frac{1}{3}\rho\uparrow$	$\frac{2}{9}(\rho\downarrow - \rho\uparrow)$
L_3	$\frac{1}{3}\rho\downarrow + \frac{5}{9}\rho\uparrow$	$\frac{5}{9}\rho\downarrow + \frac{1}{3}\rho\uparrow$	$\frac{2}{9}(-\rho\downarrow + \rho\uparrow)$

5.7.1.2 Sum-rules

The magneto optical sum rules, were firstly derived by Thole, Carra and coworkers [10, 11] for single ions in a crystal field with a partially filled valence shell. They were later extended for an independent particle approximation [12, 13]. The sum rules allow to

correlate, under certain approximation, the XMCD integrated spectrum of a specific shell with the orbital and spin magnetic moment of the ground state. A photoelectron is excited from the core state $j^{\pm} = c \pm \frac{1}{2}$ into the valence shell $l = c \pm 1$ with n electrons, where l and c are the orbital angular momenta values of the valence and the core respectively. The orbital sum rule estates that the integral over both spin-orbit-split absorption edges $j\pm$ is proportional to the orbital magnetic moment $\mu_l = -\langle L_z \rangle$:

$$\frac{\int_{j^+ + j^-}(\mu^- - \mu^+)d\omega}{\int_{j^+ + j^-}(\mu^- + \mu^+ + \mu^0)d\omega} = -\frac{1}{2}\frac{l(l+1) + 2 - c(c+1)}{l(l+1)(4l + 2 - n)}\langle L_z \rangle \tag{5.17}$$

In addition, the spin sum rule stands that the spin moment $\mu_s = -2\langle S_z \rangle$ is proportional to:

$$\begin{aligned}\frac{\int_{j^+}(\mu^- - \mu^+)d\omega - c(c+1)\int_{j^-}(\mu^- - \mu^+)d\omega}{\int_{j^+ + j^-}(\mu^- + \mu^+ + \mu^0)d\omega} &= -\frac{l(l+1) - 2 - c(c+1)}{3c(4l + 2 - n)}\langle S_z \rangle \\ &- \frac{l(l+1)[l(l+1) + 2c(c+1) + 4] - 3(c-1)^2(c+2)^2}{6lc(l+1)(4l + 2 - n)}\langle T_z \rangle\end{aligned} \tag{5.18}$$

where $\langle T_z \rangle$ is the magnetic dipole operator, which corresponds to the asphericity of the charge density of the l valence shell.

For the $2p \rightarrow nd$ transition, $(L_{2,3}, c = 1, l = 2)$ it results into:

$$\langle L_z \rangle = -2 \times \frac{\int_{L_3}(\mu^- - \mu^+)dE + \int_{L_2}(\mu^- - \mu^+)dE}{\int_{L_3 + L_2}\mu dE} \times n_h \tag{5.19}$$

and

$$\frac{2}{3}\langle S_z \rangle + \frac{7}{3}\langle T_z \rangle = -\frac{\int_{L_3}(\mu^- - \mu^+)dE - 2\int_{L_2}(\mu^- - \mu^+)dE}{\int_{L_3 + L_2}\mu dE} \times n_h \tag{5.20}$$

where n_h is the number of holes in the valence shell per atom, $\mu^0 = \frac{1}{2}(\mu^- + \mu^+)$ and $\mu = \frac{3}{2}(\mu^- + \mu^+)$ is the unpolarised cross-section. As it was previously mentioned, the sum rules are derived under several assumptions:

- The $2p \rightarrow ns$ dipole allowed transitions are ignored. Since the s band has a very small density of states, its contribution can be neglected.
- The sum rules assume that the electronic transitions occur between pure electronic levels.

- The radial matrix is taken constant.
- There is an ambiguity in the choice of the integration range and the definition of the number of holes.
- There is not interference between the two transition channels $j^{\pm}$. That is: the core hole must be well defined by quantum numbers jm. Only when the spin-orbit interaction is large compared to other interactions this assumption is valid.
- The term $\langle T_z \rangle$ is neglected for the $L_{2,3}$ edges.

5.7.2 Experimental

The XMCD spectra have been recorded in the BL39XU beamline at the SPring-8 (see Fig. 5.7.2) synchrotron. The experiments have been carried out in fluorescence (the transmission mode does not fit our purpose due to the large amount of Si substrate), with a PIN photodiode detector due to the thick Si substrate of the samples. The magnetic field (H = 50 kOe) was applied almost in the sample plane and the system was cooled down to 5 K in a He cryostat.

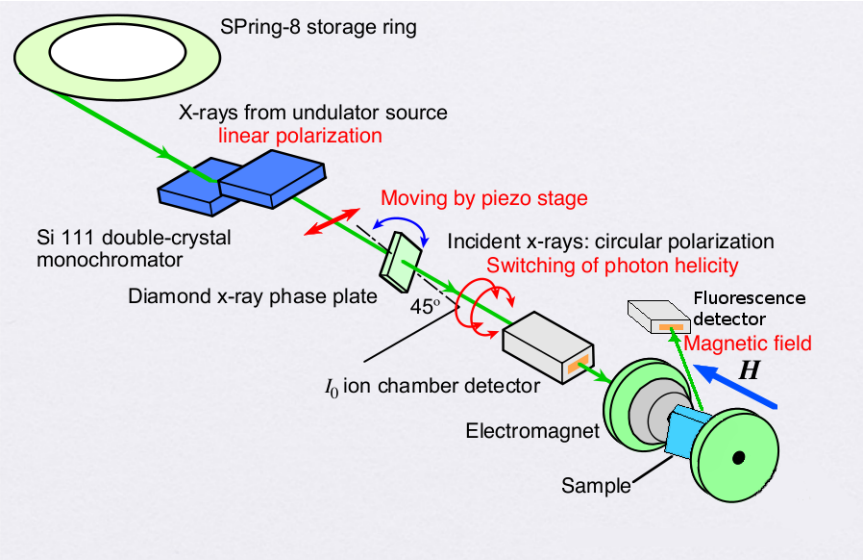

Figure 5.9: *XMCD dedicated BL39XU scheme, where the principal elements of the beam line (like the diamond X-Ray polariser) can be observed.*

Once the samples were at 5 K, XMCD L_2, L_3 at $H = 50$ kOe spectra were recorded. In addition, Element Specific Magnetisation (ESM) curves (that is, measure the dichroic signal as function of different magnetic fields) were acquired. Also the dichroic signal of the L_3 edge was measured at RT.

Bibliography

[1] N. W. Ashcroft and N. D. Mermin. *Solid state physics*. Thomson Learning, United States, 1976.

[2] L. de Broglie. *Recherches sur la théorie des quanta*. PhD thesis, Paris, 1924.

[3] D. B. Williams and C. B. Carter. *Transmission electron microscopy*. Plenum, New York, 1996.

[4] B. Fultz and J. M. Howe. *Transmission electron microscopy and diffractometry of materials*. Springer, Berlin, 2007.

[5] P. J. Goodhew. *Specimen preparation for transmission electron microscopy of materials*. Oxford University Press, Oxford, 2006.

[6] J. Baruchel, J. L. Hodeau, M. S. Lehmann, J. R. Regnard, and C. Schlenker, editors. *Neutron and synchrotron radiation for condensed matter studies*. Springer-Verlag, Berlin, 1993.

[7] G. Gauglitz and T. Vo-Dinh, editors. *Handbook of spectroscopy*. Wiley-VCH Verlag GmbH, 2003.

[8] G. Schütz, M. Knülle, R. Wienke, W. Wilhelm, W. Wagner, P. Kienle, R. Zeller, and R. Frahm. Spin-dependent photoabsorption at the L-edges of ferromagnetic Gd and Tb metal. *Z. Phys. B*, **73**:67, 1988.

[9] G. Schütz, R. Wienke, W. Wilhelm, W. Wagner, P. Kienle, and R. Frahm. Strong spin-dependent absorption at the L_2-edges of 5d-impurities in iron. *Z. Phys. B*, **75**:495, 1989.

[10] B. T. Thole, P. Carra, F. Sette, and G. van der Laan. X-ray circular dichroism as a probe of orbital magnetization. *Phys. Rev. Lett.*, **68**:1943, 1992.

[11] P. Carra, B. T. Thole, M. Altarelli, and X. Wang. X-ray circular dichroism and local magnetic fields. *Phys. Rev. Lett.*, **70**:694, 1993.

[12] M. Altarelli. Orbital-magnetization sum rule for x-ray circular dichroism: A simple proof. *Phys. Rev. B*, **47**:597, 1993.

[13] A. Ankudinov and J. J. Rehr. Sum rules for polarization-dependent x-ray absorption. *Phys. Rev. B*, **51**:1282, 1995.

Chapter 6

Experimental results of Fe_xM_{100-x} thin film

6.1 Scanning electron microscopy

The main goal related to the use of the SEM in this work is not to image the surface microstructure since, in principle, is homogeneous, but to measure the overall chemical composition. With the aid of an EDX spectrometer, this can be easily achieved. In Fig. 6.1 a great homogeneity down to the micrometer level can be observed. For all the alloys, the compositional homogeneity is excellent, with a difference no larger than 1% at. in the scanned areas. This general characteristic is relevant to employ the whole sample without worrying about the local composition. In Table 6.1 the chemical composition of the different samples is summarised. It is worth to remind the low Fe-content selected for the samples, as it was commented in the introduction. Bearing in mind that the study of the magnetic interactions is one of the aims of the present work, to deposit samples with a low Fe-content is an important landmark: it is expected that such a dilute Fe system implies a low amount of magnetic NP and a great distance between them. It is also remarkable that the samples present a great homogeneity (both, superficial and chemically) across them, since nor grain boundaries neither significant differences in the EDX spectra can be observed.

Table 6.1: *Summary of the chemical composition (EDX) of the thin films used in this work. Percentages are given in atomic fraction (% at.) and weight (% weight).*

Sample	% at. Fe	% at. M	% weight Fe	% weight M
FeAu	7 (1)	93 (1)	6 (1)	94 (1)
FeAg (1)	7 (1)	93 (1)	4 (1)	96 (1)
FeAg (2)	14 (1)	86 (1)	11 (1)	89 (1)
FeCu	9 (1)	91 (1)	9 (1)	91 (1)

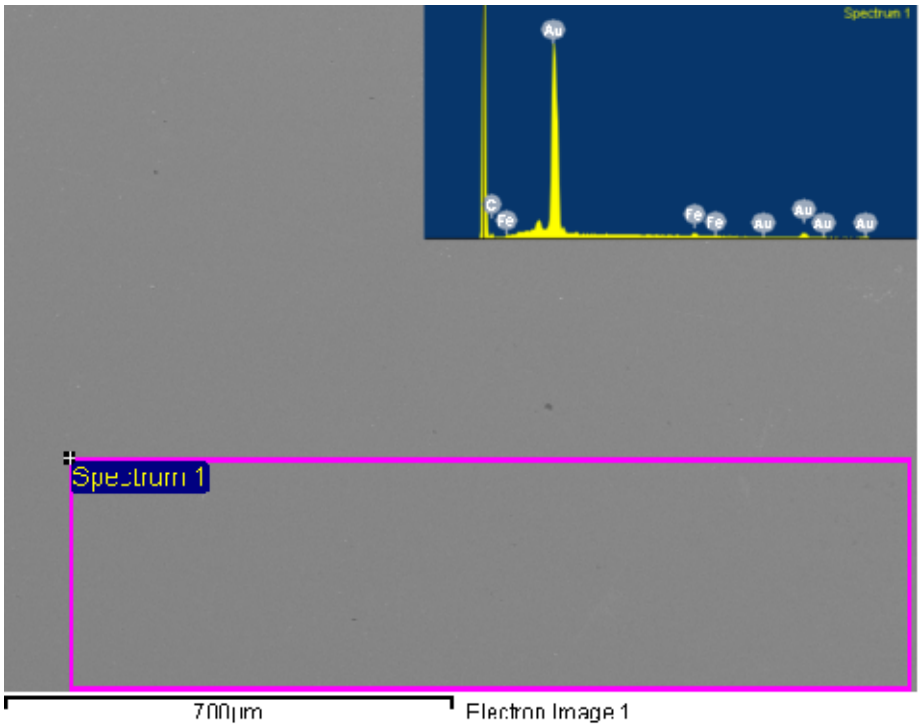

Figure 6.1: *SEM image of a typical region of Fe_7Au_{93} thin film. The homogeneity at the micro-scale is evident. The magenta rectangle marks the area where the EDX spectrum was acquired (shown in the inset).*

6.2 X-Ray diffraction

In this particular work, X-Ray diffraction (XRD) is mainly used to check the crystallinity of the samples and the possible presence of different (spurious) phases. In Fig 6.2 the diffraction patterns of three different thin films are presented.

The alloys display three (Cu film) or four (Ag and Au) different genuine peaks. The films containing Ag and Au are almost equivalent, since their share spacial group (*Fm-3m*) and their bulk lattice parameters are very close (a_{Au} = 4.0782 Å ; a_{Ag} = 4.0853 Å) displaying the main difference in the form factor which, for X-Rays, is proportional to the atomic number Z. In both cases, the first (111) reflection of the noble metal is found, followed by a double peak (not resolved) including the (200) reflection from the noble metal and the (111) reflection from the *bcc*-Fe. Although in the vicinities of the (400) reflection of the Si, lines from both the noble metal ((220) reflection, around $2\theta \sim 64.5^{o}$) and the Fe ((200 reflection, around $2\theta \sim 65^{o}$) are expected, they are completely masked by the huge contribution of the substrate. At higher angles, the (311) and (222) reflections of the noble metal are visible. It should also be present the (211) reflection from the Fe (2θ = 82.34 °). However, if we observe carefully the diffractogram of Fe_9Cu_{91}, it is clear that only 9% of Fe is not enough to produce a peak above the background and consequently, both peaks are ascribed to the noble metal. The position of the peaks corresponding to the noble metal is slightly larger (higher 2θ angle) than bulk counterparts. This points towards a possible dilution of Fe-atoms in the noble metal matrices.

It is pertinent to comment here that due to the low amount of sample mass in relation with the substrate (and the low amount of mass of the sample itself) it is very hard to get enough statistics to perform a Rietveld [1] refinement. Also the low amount of available peaks (linked to the high symmetry of the cubic group of the components) renders difficult such an analysis, since the number of parameters to adjust can be greater than the number of the peaks. A challenging difficulty in the current study is the overlapping of the Fe (*Im-3m*) diffraction lines with some of the noble metals (*Fm-3m*) (except in the case of the Cu) or with the Si (*Fd-3m*). This is added to the low Fe content and the higher

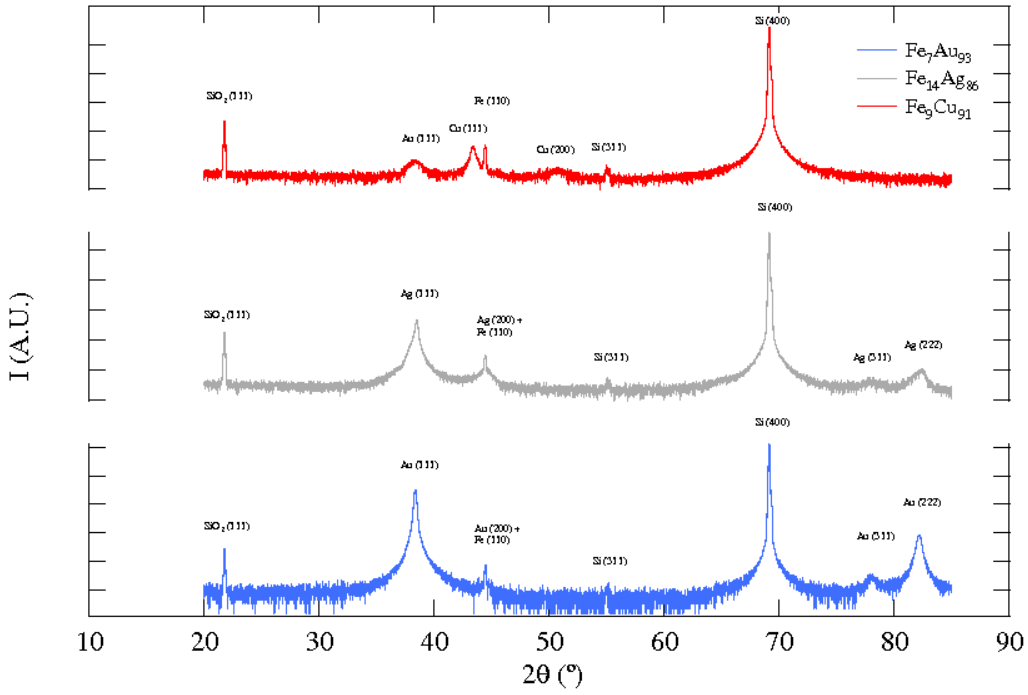

Figure 6.2: *XRD patterns of three different thin films. Note the logarithmic intensity, and that the patterns have been shifted up for the sake of clarity. Peaks are labeled with corresponding Miller indexes. The different form factors (proportional to the atomic number Z) for the different elements are evident across the series.*

form factor of the noble metals (especially Au and Ag; $Z_{Au} = 79$,$Z_{Ag} = 47$ vs $Z_{Fe} = 26$). Altogether these facts results in that is almost impossible to define unambiguously the crystallographic state of the Fe which is certainty present, since it is detected by EDX (TEM and SEM) and the samples present a magnetic response different than pure noble metals diamagnetism (see below). In the three samples the presence of the (400) Si reflection dominates the landscape. Also, a spurious reflection of the Si (311), observed at $2\theta \sim 55^{\circ}$ is observed, as well as a signal for the natural oxide layer of SiO_2 (SiO_2 (111), $2\theta \sim 21^{\circ}$).

Incidentally, the case of the Fe_9Cu_{91} is slightly different. The first film peak ($2\theta \sim 38^{\circ}$) comes from the Au coating layer. At higher angles, two consecutive peaks are observed: the (111) peak from the Cu and the (110) of the Fe. The latter peak is particularly

important, as it gives the evidence of a crystalline phase of the Fe, which can be taken as a symptom for the masked phase of Fe in the other samples. In this case, the angular position of the Fe (110) peak is extremely close ($2\theta = 44.45^{o}$) for that in the bulk Fe ($2\theta = 44.67^{o}$). Finally, the peak corresponding to the (200) Cu reflection is detected.

6.3 Transmission electron microscopy

In order to get a deeper insight of the details of the nanostructure, an exhaustive transmission electron microscopy study (and related techniques, like nano EDX, electron diffraction or scanning transmission electron microscopy STEM) has been performed.

6.3.1 Fe_7Au_{93}

In Fig 6.3 different TEM data can be seen simultaneously. The main figure corresponds to a high resolution image, where some atomic planes can be observed. The resolution of the system is limited by a coating amorphous-carbon (a-C) layer. In this particular case, since this set of samples was the first to be deposited, the a-C layer is too thick to allow high quality HRTEM images. In the upper left corner of the figure, an image with a lower magnification is presented. The photo evidences the nanogranular character of the sample. Despite the evident presence of NP, it is not possible to distinguish the chemical composition. At first sight, one is tempted to identify the darker particles as Au ones, since the scattering of the electrons produced by the Au is much greater than the Fe (it depends on the number of electrons, that is, the Z number). However, the existence of diffraction contrast makes that deduction false if we remind the influence of the nanoparticle orientation (see 5.5.2.2.2). In addition, the HRTEM image reproduces the same problem faced in the XRD. The HR contrast is given by the diffraction (as it was already explained), and again all the Fe diffraction rings match with a ring of the Au. The diffraction pattern (rings) shows the polycrystalline character of the sample down to the nanometric scale. The observation of brighter spots is originated by some particles oriented in Bragg condition.

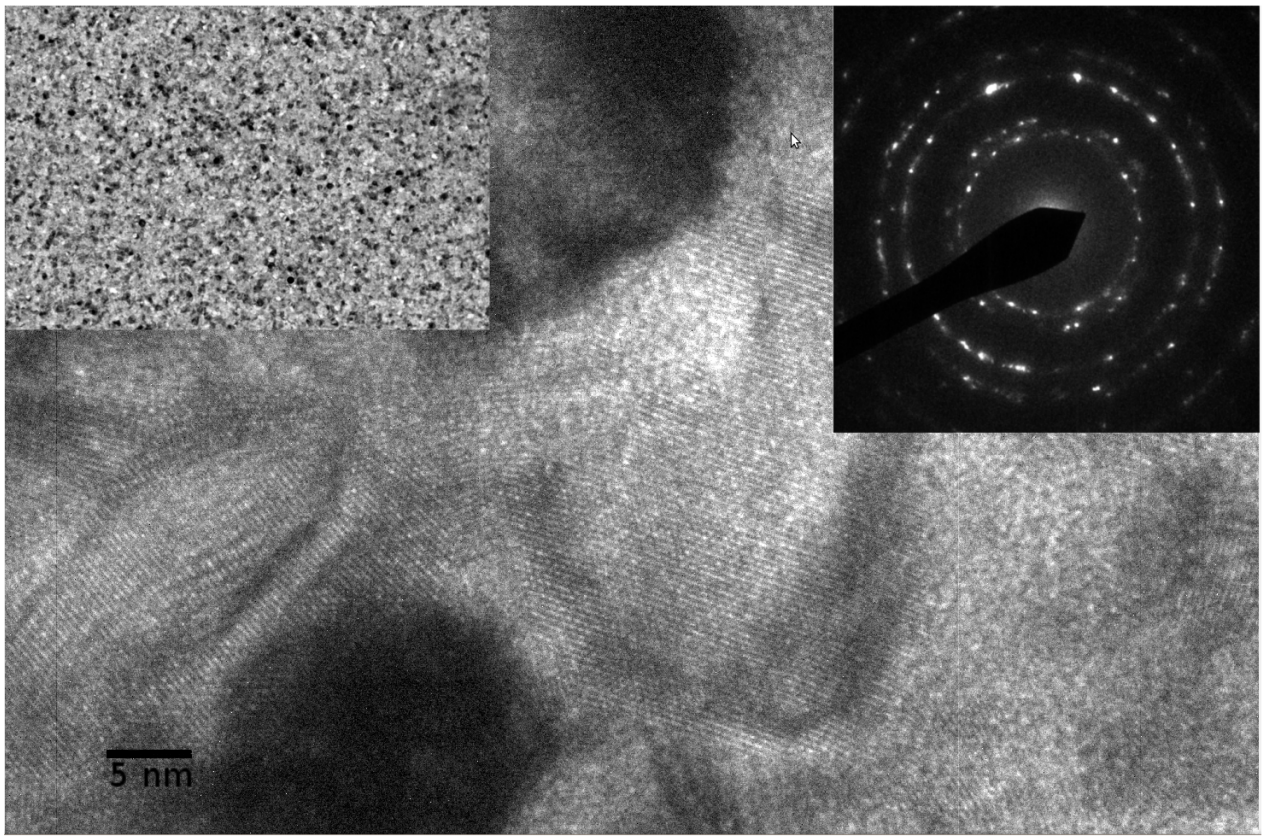

Figure 6.3: *HRTEM, TEM (upper left) images and electron diffraction pattern (upper right) of the Fe_7Au_{93} film. In this particular case, the diffraction pattern has been obtained in a Jeol 2000 FX electron microscope, which belongs to the Department of Materials of the Imperial College London, where both images (TEM and HRTEM) where acquired with a Jeol JEM 2100 at the Universidad de Cantabria.*

6.3.2 $Fe_{14}Ag_{86}$

The $Fe_{14}Ag_{86}$ system shares all the nanostructural characteristics of the previous alloy. However, due to the thinner *a*-C coating, the HRTEM pictures is of much better quality. In the HR image, atomic planes can be beautifully observed, showing, predominantly a typical (111) fcc face. However, due to the already mentioned drawbacks in 6.3.1, it is not possible to achieve a complete understanding of the nanostructure of the system, since

the Fe can not be unambiguously distinguished from the Ag.

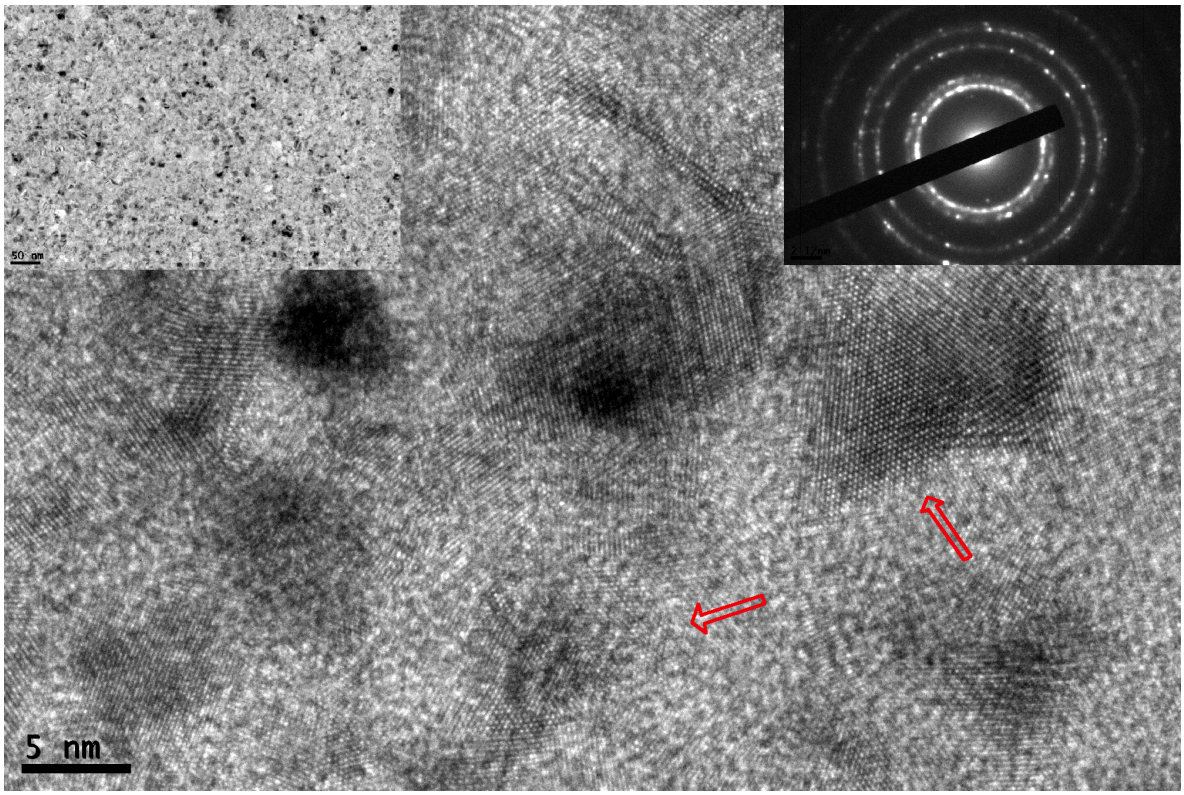

Figure 6.4: *HRTEM, TEM (upper left) images and electron diffraction pattern (upper right) of the $Fe_{14}Ag_{86}$ system. Some of the atomic planes are highlighted by red arrows. All the images have been recorded in a Jeol JEM JEM 2100 from the Universidad de Cantabria.*

6.3.3 Fe_9Cu_{91}

The same conclusions of the two previous subsections can be extracted for Fe_9Cu_{91}. In this case, although the (110) Fe reflection does not strictly overlap over the (200) Cu, the instrument resolution is not enough to separate them. In the diffraction mode the 110 Fe line is present, confirming again the XRD results.

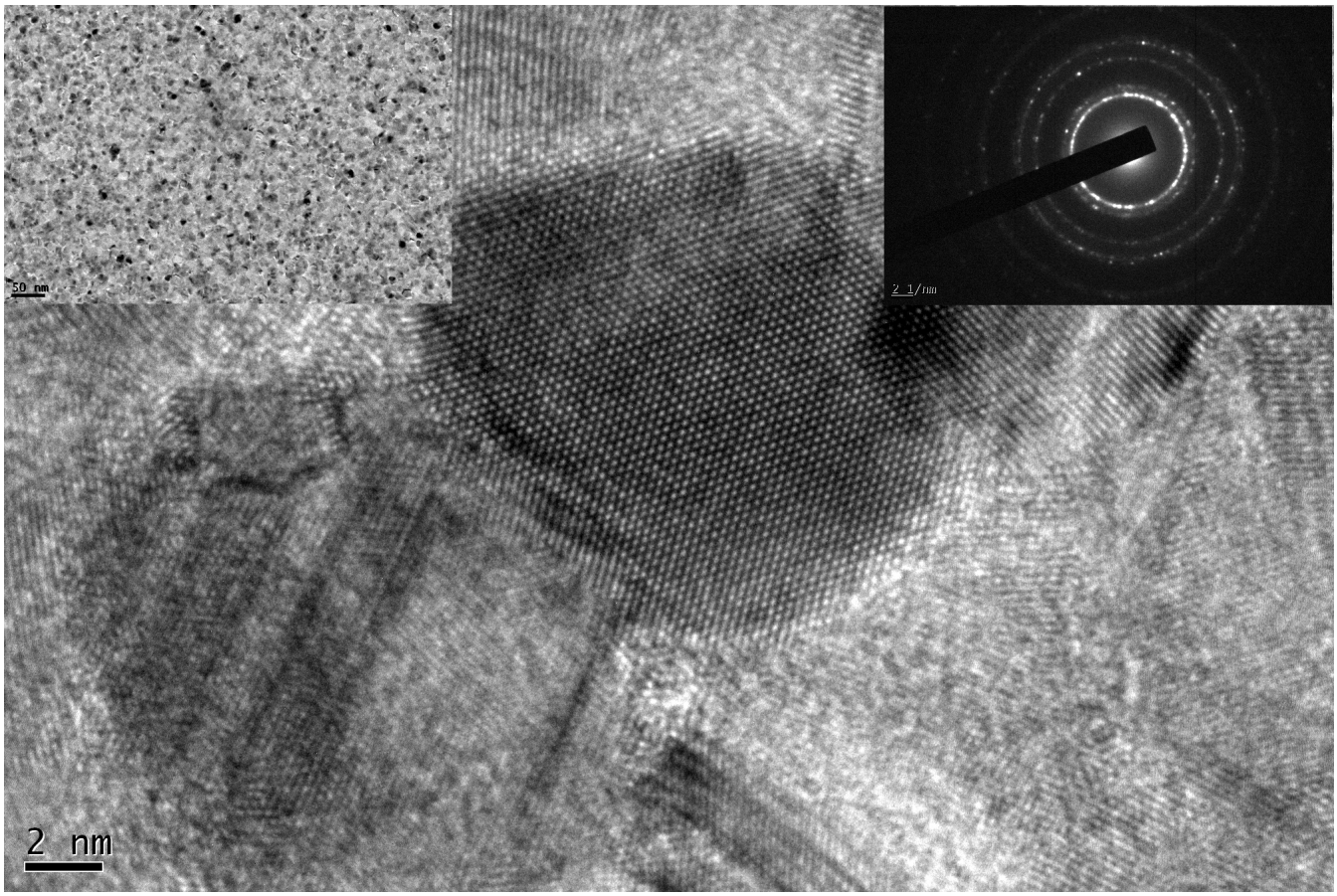

Figure 6.5: *HRTEM, TEM (upper left) images and electron diffraction pattern (upper right) of the* Fe_9Cu_{91} *system, acquired by the Jeol JEM 2100 at the Universidad de Cantabria.*

6.3.4 Dark Field Imaging

Conventional HRTEM and e^- diffraction techniques are not capable of providing a fully unambiguous results of the nanostructure of the alloys. The dark field (DF) technique is a useful approach for imaging minority phases or solid solutions in solids [2]. Again we are limited by the overlapped diffraction lines, so it is again risky to put forward the Fe location in the images. Despite this limitation, we recorded the images concentrating mainly on the (111) diffraction line of the noble metal (Fig. 6.6). A random distribution of the bright spots formed by the (111) reflection can be observed, pointing to a random distribution of all the phases across the sample. Respect the morphology, quasi circular

shape of the NP can be inferred (see Fig 6.6).

A trial to estimate the size and morphology of the Fe was pursued exhaustively. The supporting idea was to isolate the Fe (110) + M(200) reflection and produce its DF image. However this was not possible due to undefined resolution of the aperture.

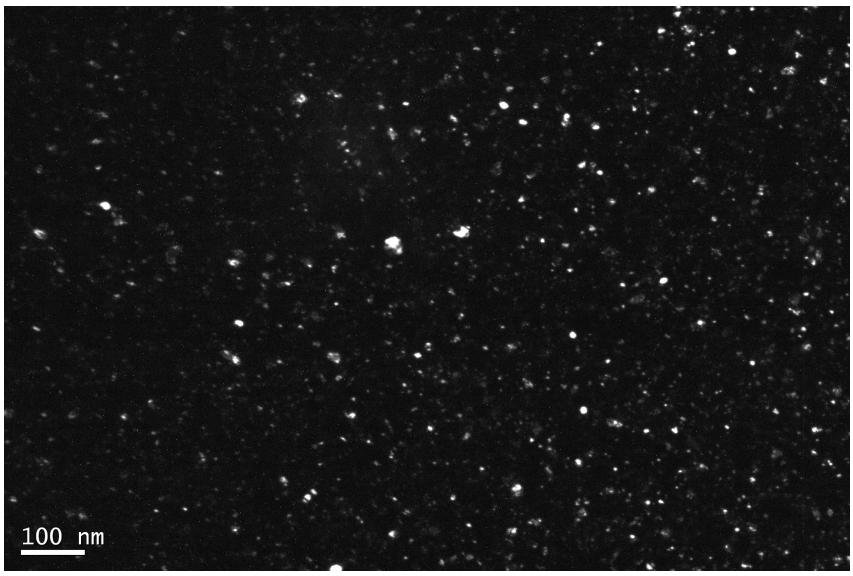

Figure 6.6: *Dark Field image of the (111) reflection of the Ag in the $Fe_{14}Ag_{86}$ system.*

6.3.5 STEM

A complementary point of view is brought by the HAADF STEM technique. This is, in principle, a very powerful technique to detect compositional variations at the nanoscale. If the sample has an homogeneous thickness, the image contrast only depends on the Z number of the particular atom. Thus, systems like Fe-Ag or especially Fe-Au with a very different Z number are good systems to deal with. However, the thickness inhomogeneities are enough to threaten a good resolution of the Fe nanostructure.

As it can be seen in Fig. 6.7, there is not a direct relation between the image color and the chemical composition. EDX spectra acquired at image points with a neat change in the contrast are almost equal: spectrum 2 (acquired in an almost black region, which

should be a Fe-rich region in a image with a pure Z contrast) is very close to spectrum 3 (acquired in a white region, which should correspond to a region richer in Au). In short, it is clear that the electron microscopy provides evidence of nanostructure in the alloys, but the identification of the Fe crystallites is still dubious.

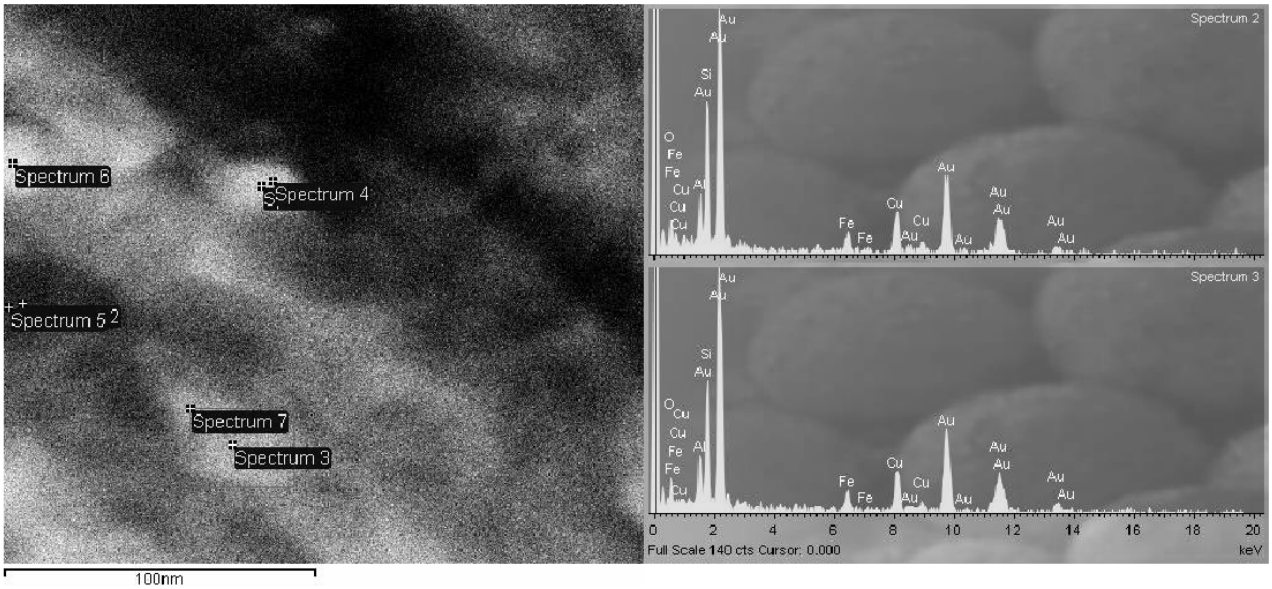

Figure 6.7: *HAADF image of the Fe_7Au_{93}. The EDX spectra from Spectrum 2 (dark area in the image) and 3 (bright part of the image) are shown in the right panel, up and down respectively. Spurious contributions of Cu (sample holder and the microscope), Si and O (substrate of the film) and Al (coming from from the sample preparation) are present in the EDX spectra. The similar chemical composition regardless the image contrast is a clear sign of thickness variation.*

6.4 SQUID magnetometry

In the following, our magnetometry results for the thin films will be described. Although some common features are present, the results are presented in sections, providing separately the results for each technique and film. In all the DC measurements (ZFC/FC and hysteresis loops) a correction of the diamagnetic signal from the substrate has been carefully applied. The susceptibility of the Si was measured at RT and 5 K, showing negligible temperature variation.

6.4.1 DC-Magnetisation: irreversibility

A common procedure to characterise the magnetic properties of a clustered/nanostructured material is to record the variation of the magnetisation in different field conditions when the temperature is changed. The typical zero field cooling (ZFC) process consist in a cooling down of the sample in absence of a magnetic field. Then a field at low temperature is applied and afterwards the magnetic response holding the field constant while the temperature increases is measured. In the field cooling (FC) process there is an applied magnetic field at high temperature and then the magnetisation is measured while the temperature is changing.

6.4.1.1 As deposited samples

A general inspection of Figs. 6.8, 6.9, 6.10 and 6.11 show that the ZFC/FC processes display a neat maximum at a certain temperature (blocking temperature, T_B in the following), a splitting between the ZFC and the FC branches (irreversibility) and a rapid fall above T_B. The most characteristic parameters have been inserted in table 6.2. It seems clear that the Fe-content increase results in concomitant elevation of the magnetisation values. This tendency also applies for T_{max} (K) and T_{irr} except for the Fe_7Au_{93}. The latter is probably signalling an enhanced magnetic contribution more visible in the Au matrix alloys. Respect the ZFC, the shape of the peaks changes with the applied field, as in other disordered magnetic alloys [3], the manganites [4] or the magnetic semiconductors [5] to cite some with different electronic character.

In m_{ZFC}, two contributions can be inferred. The first one, evident even at low fields, displaces towards higher temperatures when the field goes up. This result is expected since a larger field, in simple words, favours the magnetic order at higher temperatures. The second contribution is not observable at weak applied fields. However, when the field increases it becomes more and more important. This contribution shifts towards lower temperatures when the field increases, like in the ferromagnetic-spin glass transition of the reentrant spin glasses [3]. This behaviour is witnessing a growth of the FM cluster

Table 6.2: *Magnetisation parameters of the samples at H = 100 Oe.*

Sample	m_{300K}(emu/cc) x 10^2	m_{max}(emu/cc) x 10^2	T_{max} (K)	T_{irr} (K)
Fe_7Au_{93}	0.19	0.7285	29	25
Fe_7Ag_{93}	0.22	1.44	17	13
Fe_9Cu_{91}	0.40	9.47	26	17
$Fe_{14}Ag_{86}$	0.72	15.6	32	19

size mediated by the applied field: when the magnetic field is intense, the susceptibility curve is limited by the demagnetisation factor, constraining the rise in the susceptibility [3].

Turning our focus to the thermal variation of the m_{FC}, several striking features deserve particular attention. First of all, the FC process has a maximum, a minimum and a upturn of the magnetization at very low temperatures in the more diluted alloys (Fe_7Au_{93}, Fe_7Ag_{93} and Fe_9Cu_{91}). The drop of the susceptibility in the FC at low temperatures (T $<$ T_B) is usually attributed to the super spin glass (SSG) state [6], while the rise of the magnetization is attributed to the presence of subnanometric magnetic nanoparticles, at least when these are embedded in dielectric matrices (Al_2O_3) [7]. Last but not least, the magnetization decrease for T $>$ T_B does not follow a Curie law, as is expected for classical SPM, SG or SSG systems [8, 9] at low fields and high temperatures. Note that in ideal SPM and canonical SG systems, the FC branch is relatively temperature-constant at T $<$ T_B, T_f[1].

Now we turn our description to the FC thermal demagnetisation under a high magnetic field of $H = 45$ kOe shown in Fig 6.12. The temperature dependence of the magnetisation does not follow the expected spin-wave shape at temperatures [10] T $< 0.15\, T_C$ (supposing a bulk $T_C = 1015$ K for pure Fe). It has been reported that magnetic nanoparticles can show the magnon variation in very different materials produced by several routes, such as Fe-Cu-Ag [11] (metals) or BaFeTiO [12] (oxides).

[1]The T_B and T_f labelling is maintained ambiguous in the result section deliberately to remind the reader the ambiguity of the result, only using DC-magnetisation

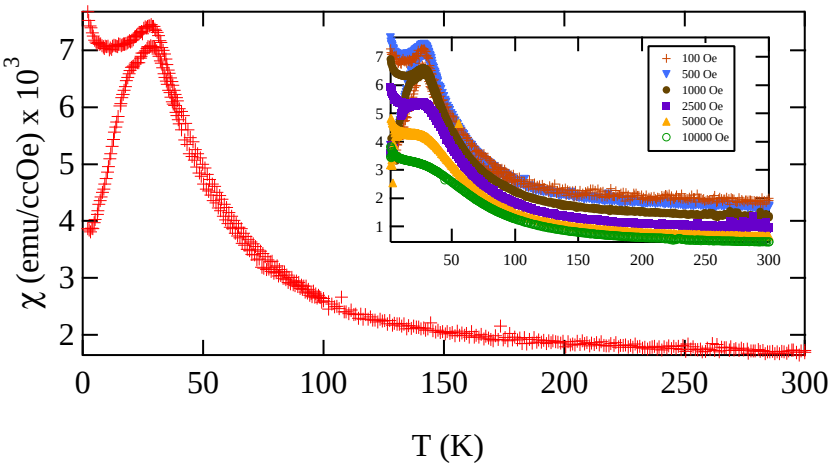

Figure 6.8: *ZFC/FC process of the Fe_7Au_{93} as-deposited with different applied fields. It is clear the presence of the FC upturn at low temperature an the double-peak structure. The irreversibility is almost destroyed at 10 kOe. The inset show the variation of the $M_{DC}(T)$ with different applied fields.*

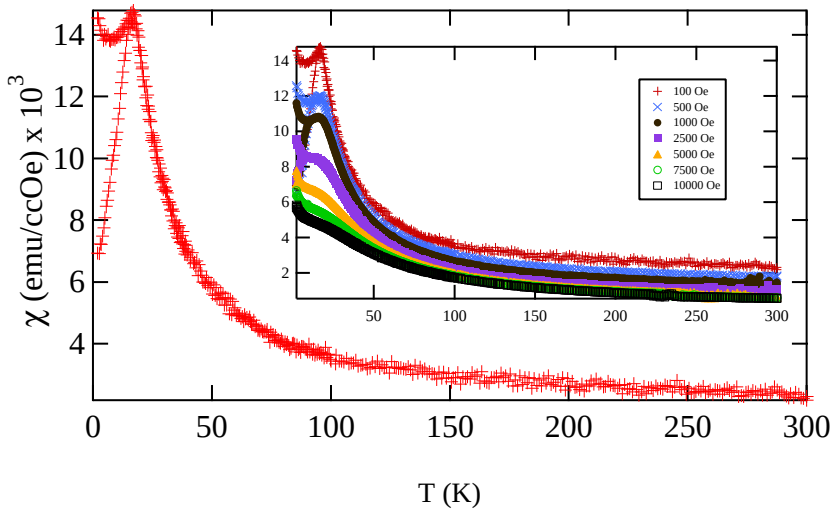

Figure 6.9: *ZFC/FC process of the Fe_7Ag_{93} with different applied fields. Here the peak structure is not visible at 100 Oe, although it appears at higher fields. The FC upturn is obviously present. The inset show the variation of the $M_{DC}(T)$ with different applied fields.*

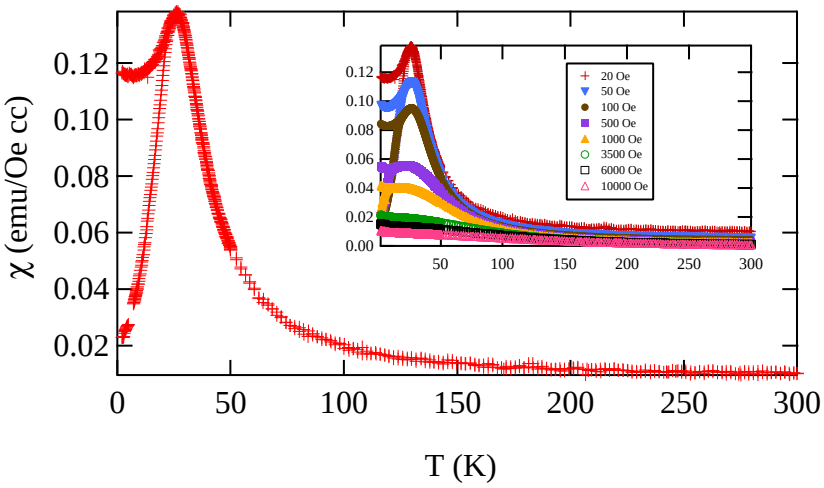

Figure 6.10: *ZFC/FC process of the Fe_9Cu_{91} with different applied fields. In this case the FC upturn is very subtle, although the fall of the FC magnetisation below T_f is evident. The inset show the variation of the $M_{DC}(T)$ with different applied fields.*

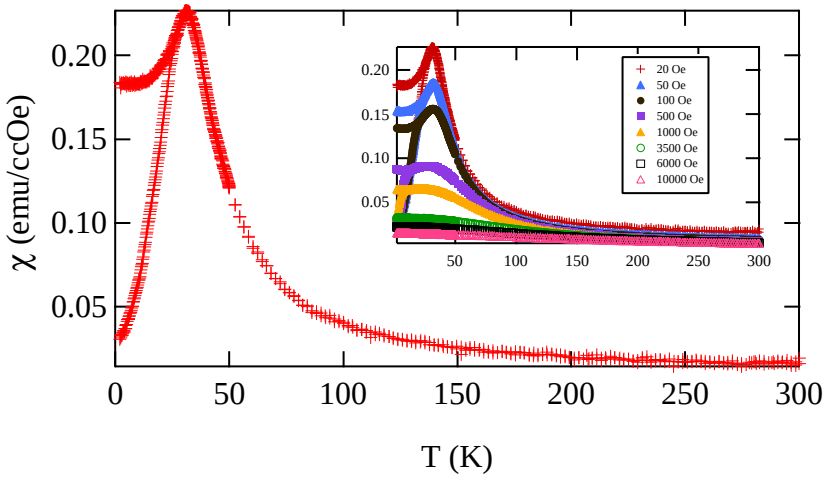

Figure 6.11: *ZFC/FC process of the $Fe_{14}Ag_{86}$ with different applied fields. It does not exist the FC upturn, but like in the Fe_9Cu_{91} there is a fall of the magnetisation below T_f. As in all the films, there is a plateau in the magnetisation peak when the field increases. The inset show the variation of the $M_{DC}(T)$ with different applied fields.*

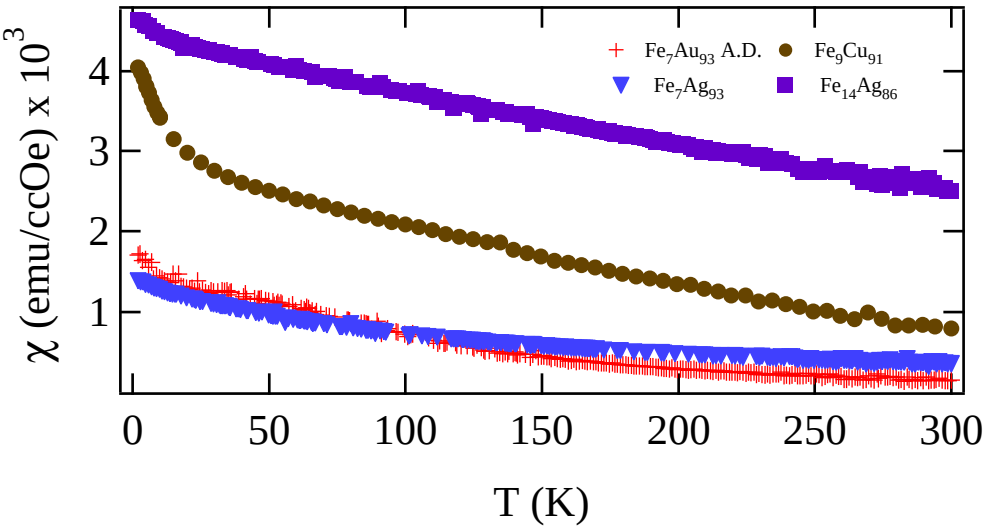

Figure 6.12: *FC measurement of the four films with an applied field of 45kOe. Different shapes are present, but no one follows a typical Bloch law.*

6.4.1.2 Annealed Fe_7Au_{93}

To gain a deeper insight about the effect of the nanostructure of the sample on the magnetic properties, an annealing treatment was performed on the Fe_7Au_{93} film. This was carried out under high vacuum to avoid oxidation of the Fe NP, and in successive temperature steps, measuring the magnetic properties after each one. After annealing the sample at 200 ºC during 1 hour, a significant change in the ZFC/FC process was found (see Fig. 6.13). At low applied fields, it is marked the onset of two different peaks. The low temperature peak has almost the same shape than in the as-deposited sample, and also occurs below 50 K. The susceptibility also present an increase of its absolute value. The second peak is located at much higher temperatures (around 110 K), and slightly above it, there is a rapid fall of the susceptibility. When the magnetic field is increased, the high temperature feature is destroyed, regaining the same initial shape as in the as-deposited film.

Further annealing (1h at 250 ºC) was carried out as well. As deduced from inspection of figure 6.14, the high temperature peak gains intensity and displaces towards higher

temperatures (170 K). Again, there is an increase of the susceptibility, and the magnetic field does not affect very much the low temperature peak, while the high temperature one is broadened and finally destroyed, when $H > 1$ kOe. Finally it is worth commenting that the FC upturn is still present, although is much less pronounced than in the as-deposited system.

As it was already commented, there is a remarkable difference between the as-deposited and annealed Fe_7Au_{93} systems at low magnetic applied fields. However, as observed in Fig. 6.15, the shape of both curves at $H = 45$ kOe is almost equal, and the absolute difference between the susceptibility at 300 K and 2 K is the same. The most salient change is the addition of an offset ($\sim 10^{-3}$ $emu/ccOe$) to the magnetisation.

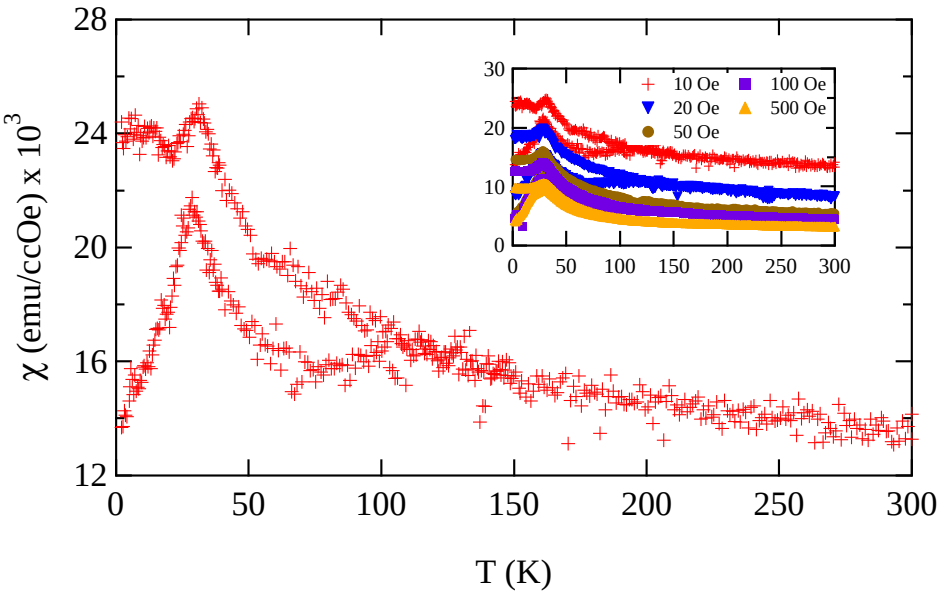

Figure 6.13: *ZFC/FC process of the Fe_7Au_{93} annealed at 200 ^oC with different applied fields. The ZFC/FC present a clearly separated double-peak. The upturn is still present, although is much less clear. The inset show the variation of the $M_{DC}(T)$ with different applied fields.*

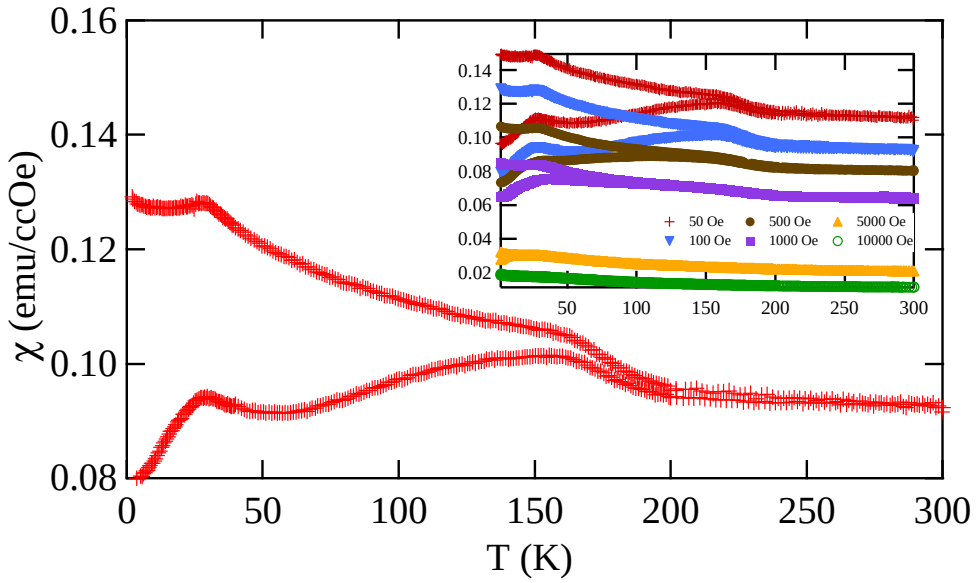

Figure 6.14: *ZFC/FC process of the Fe_7Au_{93} annealed up to 250 °C. The high temperature peak is now more intense and at higher temperature. The inset show the variation of the $M_{DC}(T)$ with different applied fields.*

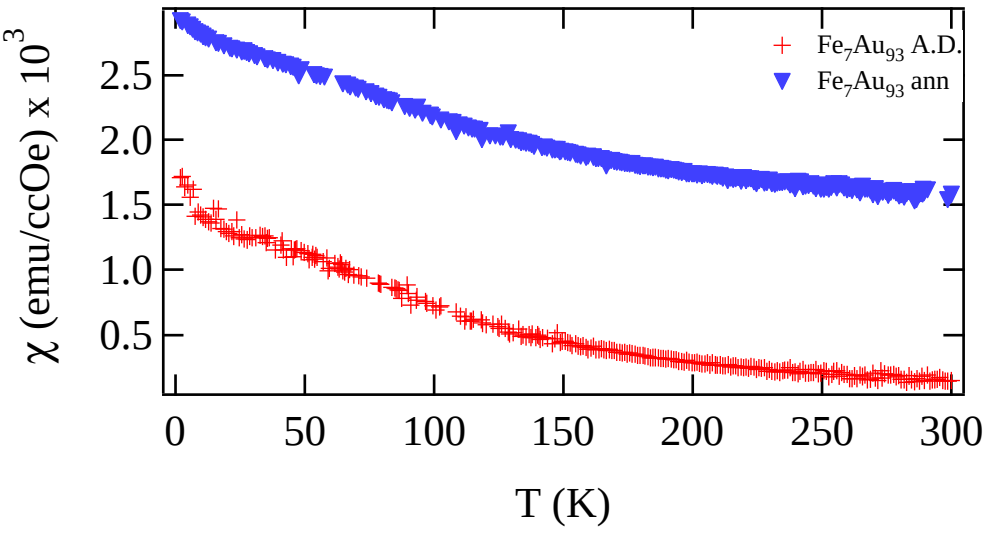

Figure 6.15: *FC measurement of the Fe_7Au_{93} as-deposited and annealed samples at H = 45 kOe. The shape and the susceptibility variation are almost equal, although a susceptibility offset is present for the annealed film.*

6.4.1.3 Mechanically alloyed $Fe_{14}Au_{86}$

As commented before we have fabricated $Fe_{14}Au_{86}$, $Fe_{10}Cu_{10}Au_{80}$ and $Fe_{15}Cu_{11}Au_{74}$ alloys by mechanical alloying from powdered elements. The initial idea was to compare the results coming from both kind of production routes and sample morphology: thin films and powdered alloys. In Fig. 6.16 (only one curve of the system $Fe_{14}Au_{86}$ is shown, but all the milled alloys are quite similar), the mechanically alloyed powders present a completely different behaviour, close to a classical RSG as is expected for its chemical composition [9], with the para-ferro transition above 300 K. The marked difference with the curves of the thin films is striking but it is true that the RSG-like behaviour in milled alloys has been investigated in detail. Nonetheless the difference appear huge and we have postponed a direct comparison. Such a comparison appears out of the scope of the present work.

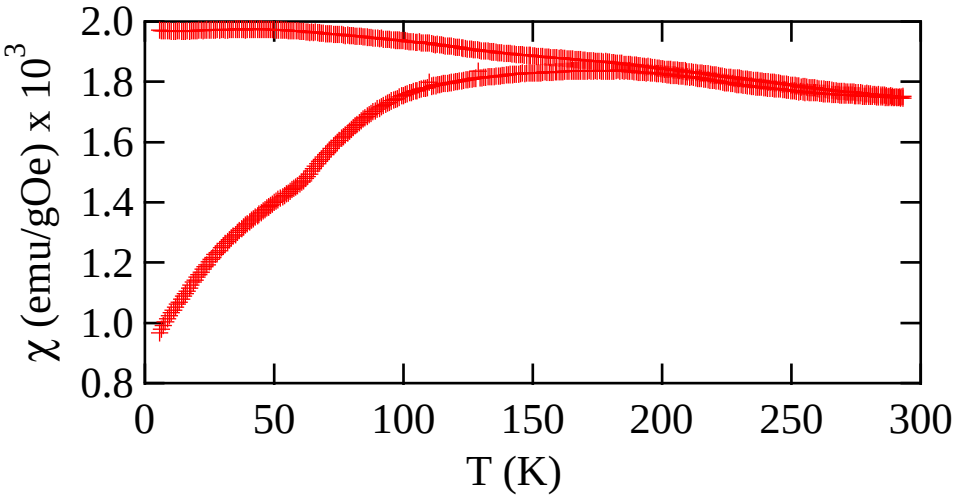

Figure 6.16: *ZFC/FC process of the $Fe_{14}Au_{86}$ powdered alloy at H = 100 Oe. As is expected from its chemical composition and the Mydosh phase diagram [9], a RSG behaviour is present, although with a much greater glassy temperature ($T_f \sim 180$ K).*

6.4.2 Magnetisation vs field loops

Hysteresis loops have been performed in order to get information about the anisotropy and the absolute magnetic moment of the alloys. Since the results obtained are rather similar for every film, we will describe in detail both, the Fe_7Au_{93} as-deposited sample and the annealed counterpart. Whenever it is necessary a distinct mention to the particular features detected in other samples, it will be described.

6.4.2.1 As-deposited samples

In Fig. 6.17 the M(H) loops at different temperatures of Fe_7Au_{93} as-deposited, Fe_7Ag_{93}, Fe_9Cu_{91} and $Fe_{14}Ag_{86}$ are plotted. The first striking detail is the existence of hysteresis even at 300 K. This rules out the existence of SPM at room temperature (RT), showing that the magnetic interactions among the nanoparticles are more important than expected in principle for such a dilute Fe-concentration. The coercive field is high ($H_c \sim 150$ Oe) if it is compared with the bulk *bcc*-Fe ($H_c = 0.9$ Oe) [10], or more striking, to the absence of hysteresis at RT in the canonical spin glasses [9] or in Fe_xAg_{100-x} (x = 20, 35, 39 and 45 sputtered films) [13]. There is a lack of saturation of the samples up to $H = 45$ kOe, compared to the few Oe needed to saturate the *bcc*-Fe [10]. As occurs in conventional magnetic materials, the saturation magnetisation decreases with increasing temperature, as well as the remanent magnetization. However, the variation of the coercive field with the temperature presents a minimum. This striking behaviour can be attributed to the grow/decrease of clusters formed by of magnetic nanoparticles, as we will discuss later (see section 7.2). It is also observed that the saturation magnetisation value does not arrive to that corresponding to *bcc*-Fe bulk. This detail may reveal or the existence of diluted Fe atoms in the matrix.

In a quick glance of the results, at low temperatures, the susceptibility of the Fe_7Au_{93} seems to be higher than that of Fe_7Ag_{93}. However, if the susceptibility is normalised to the Fe volume, the corresponding values scale perfectly. The coercive field for the Fe_7Ag_{93} (H_c= 190 Oe) is marginally larger than in the Fe_7Au_{93} ($H_c = 170$ Oe), while the

remanent magnetisation (M_R = 0.40 (8) *emu/cc*) is lower than in the Fe_7Au_{93} (M_R = 0.68 (12) *emu/cc*). The same variation of the coercive field with temperature is found in the Fe_7Au_{93} alloy.

Respect to the Fe_9Cu_{91} film, the susceptibility (even normalized to the Fe volume in the sample) is much greater, arriving to a value around 1500 *emu/cc* of Fe, close to the 1745 *emu/cc* of the bulk *bcc*-Fe. The coercive field is in the same order of magnitude than the previous samples (H_c = 170 *Oe*), and still much greater than the bulk, and it also presents a minimum in H_c(T) curve. In this case, the magnetisation rises up quicker than in the less-concentrated samples.

Finally, the saturation magnetisation of the more concentrated $Fe_{14}Ag_{86}$ is largest, reaching M_s = 208 *emu/cc* due to the higher Fe-content. In parallel to the other Fe_7Ag_{93} sample, there is a temperature (around 30 K) where the coercive field is below the detection limit of the SQUID. In this particular sample, the magnetic moment per cubic centimetre of Fe is around 2000 *emu*, larger than the 1745.88 *emu/cc* of the *bcc*-Fe. If the value of the saturation magnetisation is transformed in a volume percentage of Fe in the sample, it results in a 11.8% of Fe. Although the actual figure is larger than that measured by EDX, 11 (1) % is in the uncertainty range. The shape of this hysteresis loop is a proof that the higher the Fe-content, the quicker rise in the magnetisation, since it is more rapid than in the Fe_9Cu_{91} system, getting closer to the *bcc*-Fe bulk (although still far away!).

To sum up, the lack of saturation even at 50 *kOe* supports the presence of magnetic nanoparticles in the matrix; the RT coercivity leads to the idea that the SPM model can not be applied on these alloys. Finally the variation of the H_c with temperature point to a coupling/decoupling process of the ferromagnetic nanoparticles tuned by the temperature.

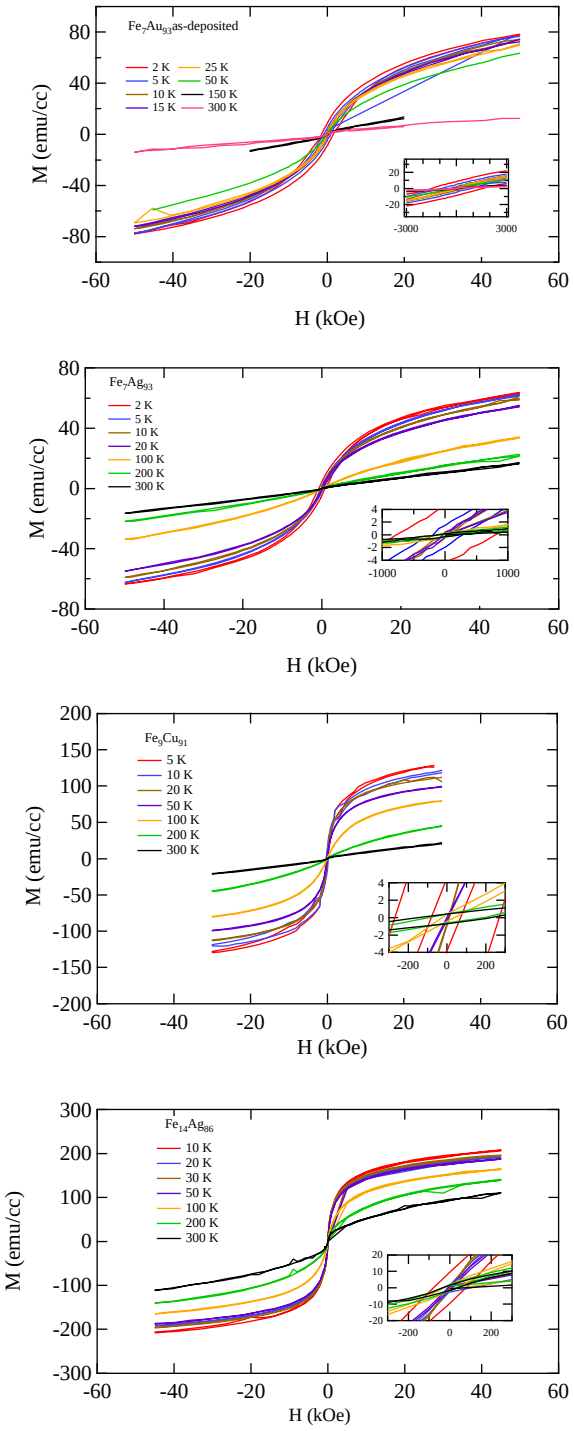

Figure 6.17: *Hysteresis loop of the Fe_7Au_{93} as-deposited, Fe_7Ag_{93}, Fe_9Cu_{91} and $Fe_{14}Ag_{86}$ alloys (respectively) at different temperatures. No saturation at the maximum field available is reached and there exist coercivity and remanent magnetisation even at 300 K (see the insets).*

6.4.2.2 Annealed films

The magnetisation response to an external field of the annealed sample at 250 °C is very different (see Fig. 6.18). The magnetisation value at 45 kOe increases respect to that of the as-deposited sample. Surprisingly, this very large value ($\sim$ 150 emu/cc) obtained taking into account the EDX Fe-content cannot be explained in a simple form. This value exceeds the magnetisation value of the pure Fe. Signals of this effect was pointed in the $Fe_{14}Ag_{86}$.

Similarly to the as-deposited bunch of films, a $H = 45\ kOe$ is not enough to saturate the magnetisation, especially at low temperatures. This is a clear sign for the existence of disorder and frequently connected to surface spins on the nanoparticles [14]

Another attractive difference is the absence of a minimum in the thermal variation of the coercivity which was found in every as-deposited alloy. The coercivity is lower (softer) than the as-deposited one which suggest bigger Fe regions. In the annealed sample the magnetisation growth is more pronounced than in the as-deposited one, and even faster than in the $Fe_{14}Ag_{86}$. This fact should be connected to the existence of larger FM regions or exchange coupled ensembles of clusters, originated by the NP growth due to the thermal treatment.

To sum up, the main values obtained from the hysteresis loops are presented. It can be clearly observed that the saturation magnetisation follows the increase of concentration of Fe. No clear correlation can be defined in the case of the coercive field in table 6.3 .

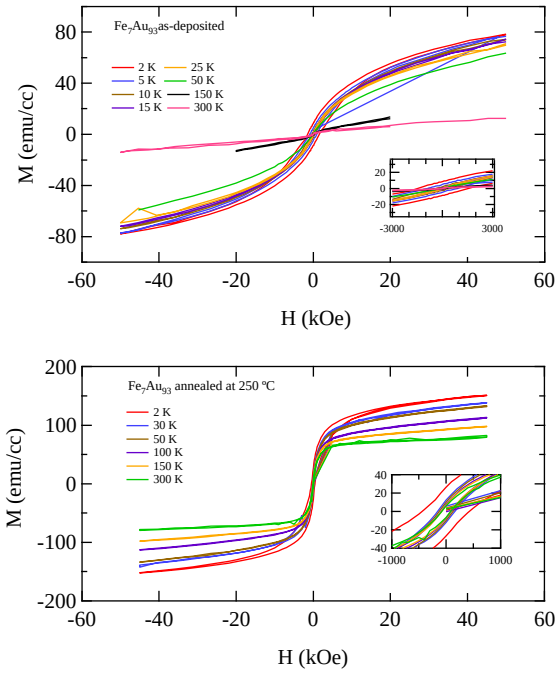

Figure 6.18: *Hysteresis loop of the Fe_7Au_{93} as-deposited, and Fe_7Au_{93} annealed at 250 ^oC alloys (respectively) at different temperatures. After the thermal treatment, the magnetisation at 45 kOe and the remanent magnetisation grow, while the coercive field decreases.*

Table 6.3: *Summary of the main parameters of the hysteresis loops at 10 and 300 K. H_c is the coercive field and M_s the saturation magnetisation. The values used for the Fe_7Au_{93} annealed at 250 ^oC (Fe_7Au_{93} Ann) have been extrapolated using the data at 5 and 15 K.*

Sample	H_c^{10K} (Oe)	H_c^{300K} (Oe)	M_s^{10K} (emu/ccOe)	M_s^{300K} (emu/ccOe)
Fe_7Au_{93} AD	417	170	113	12
Fe_7Ag_{93}	48	191	98	22
Fe_9Cu_{91}	70	170	121	21
$Fe_{14}Ag_{86}$	78	36	208	111
Fe_7Au_{93} Ann.	233	81	237	123

6.4.3 AC susceptibility

One of the most typical and efficient techniques for the study of glassy magnetic phases is the AC susceptibility (χ_{AC}). The application of a very low ($h = 3.58\ Oe$) oscillating magnetic field at different frequencies permits to record very minor magnetic changes. In modern SQUIDs it is a helpful technique since it covers nearly 5 decades of frequency in a single instrument, giving a deep insight into the dynamic magnetic response of the samples. Unfortunately, as was mentioned before, one of the main difficulties of the current work is the extremely weak magnetic response of the samples ($10^{-7} emu$) originated by the low amount of mass available, constrained by the samples itself. This creates difficulties when recording signals which are small for the quality required to perform a complete critical slowing down analysis. Indeed, in the samples with 7 % at. of Fe without annealing, it was impossible to obtain any reproducible signal and, for the other cases, the susceptibility values are in the very limit of the SQUID detection. Despite the inherent limitations of our samples, the AC susceptibility information is relevant. In Figs. 6.19 (Fe_9Cu_{91}) and 6.20 ($Fe_{14}Ag_{86}$), the position of the peak in the real part of the susceptibility (χ') shift up to higher temperatures when the frequency (ω) increases, and a reduction of the magnitude of the $\chi'(T)$ is also observed. This behaviour is typical in the spin glass alloys [2], and in the present case, confirms the influence of the interactions in this NP system despite the low Fe content. The $Fe_{14}Ag_{86}$ has enough signal to record the imaginary part of the susceptibility (χ''), related to the magnetic losses. Commonly for the χ'', its value rises with the frequency, and the maximum position shifts up to higher temperatures. The peak temperature also matches roughly with the peak temperature observed in the ZFC/FC measurements at H $< 100\ Oe$. A study with different biasing H_{DC} fields would be very interesting, however the application of biasing fields reduces the raw signal, making impossible the detection with the available instruments.

[2]Note that the SG term is now *extended* to systems with magnetic disorder and presence of irreversibilities.

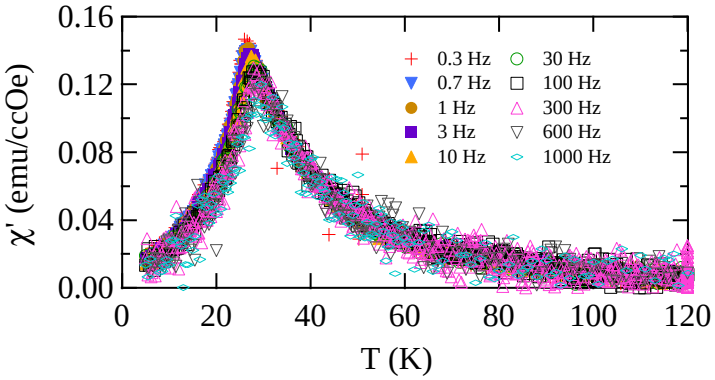

Figure 6.19: *AC susceptibility curves of Fe_9Cu_{91} at different frequencies. There is a definite trend marking the reduction and the displacement of the peak to higher temperatures when the frequency increases.*

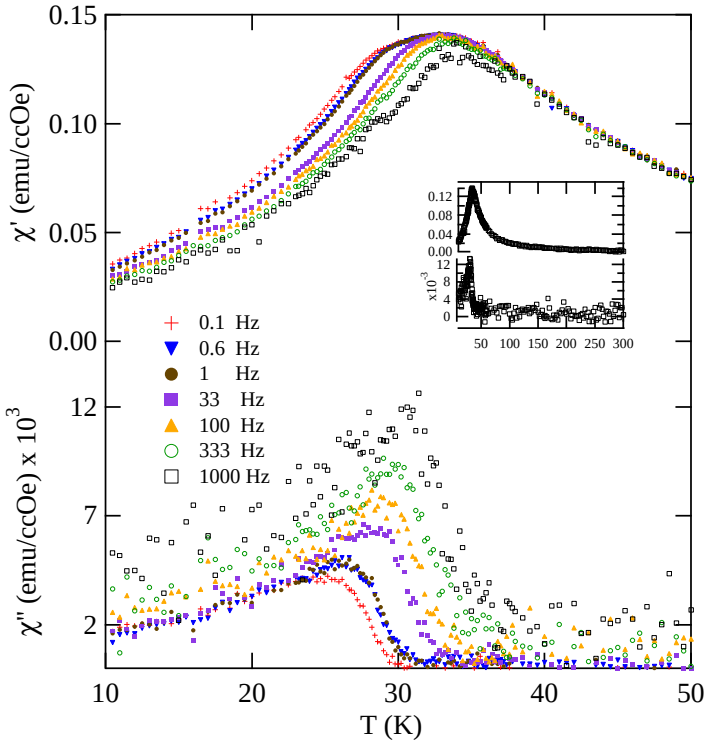

Figure 6.20: *AC susceptibility curves of $Fe_{14}Cu_{86}$ at different frequencies. The upper part of the graph shows the real component χ', while the figure at the bottom displays the imaginary one χ'' . The shows displays the whole thermal variation.*

In Fig. 6.21 (corresponding to the Fe_7Au_{93} annealed sample at 200 and 250 °C) two peaks can be observed at different temperatures. The comparison with the ZFC branch of M_{DC} at $H = 10$ and 50 Oe respectively is a beautiful example of a good correlation between χ_{AC} and static M_{DC}. Due to the low signal to noise ratio, it is impossible to assure the dynamic response of the alloys.

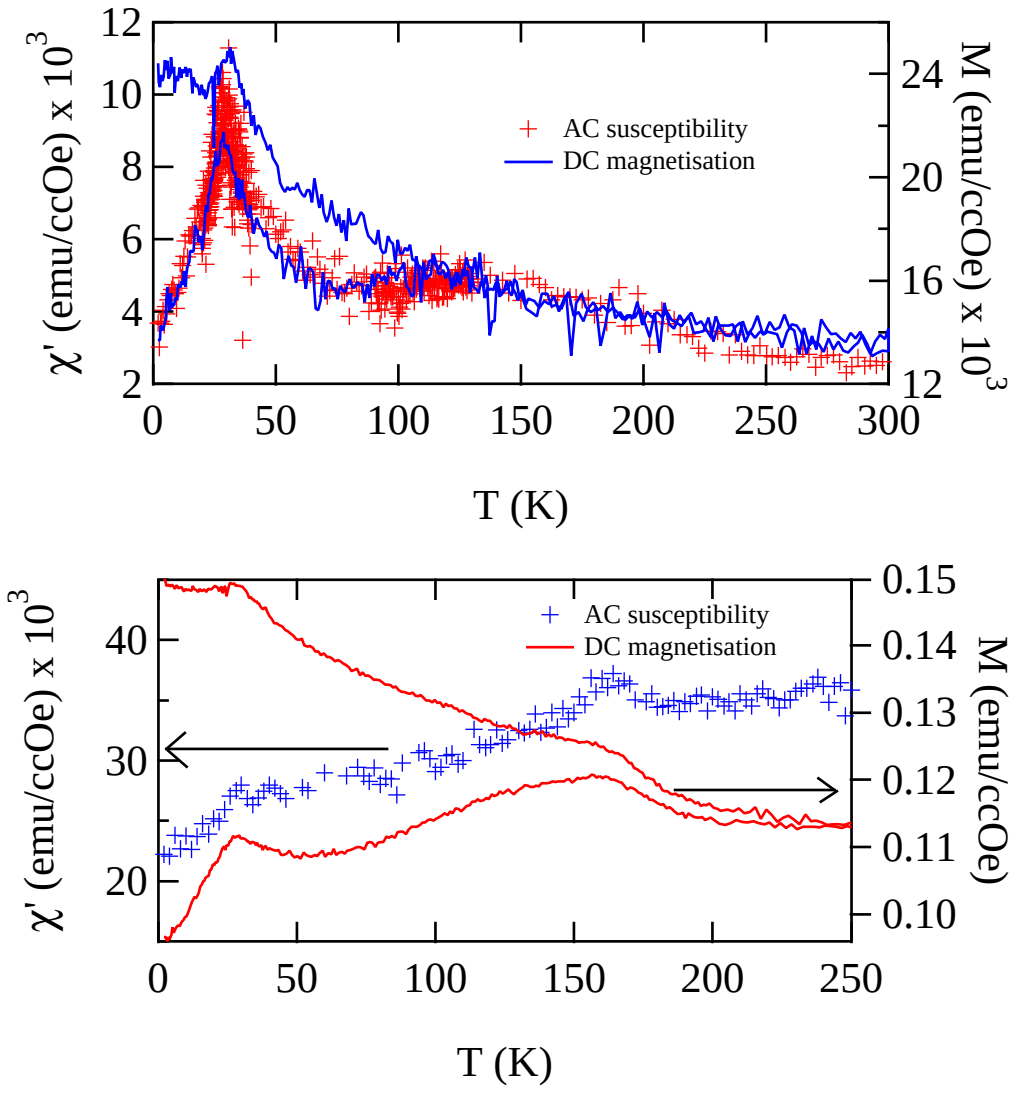

Figure 6.21: *AC susceptibility curve at $\omega = 1$ Hz of Fe_7Au_{93} annealed at 200 °C (up) 250 °C (down), superposed to the M_{DC} magnetisation. It is remarkable the matching of the susceptibility recorded in static and dynamic conditions.*

6.5 AC electrical resistivity

For many years, the electrical resistivity (ρ) of conducting solids has been used to investigate the micro(nano) structure of metals [15]. The combined use of the electronic transport with diffraction techniques (X-Ray, neutrons and electrons) provided excellent results [16]. In the following, we will present results of the thermal dependence of the resistivity at a fixed field and the magnetic dependence at a fixed temperature.

6.5.1 Thermal dependence

The thermal variation of the resistivity between 2 and 300 K at different magnetic fields (H = 0, 10 and 20 kOe) has been measured. As expected for metals, the resistivity increases monotonically with increasing temperature. The effect of a static magnetic field is a decrease of the resistivity. This is more evident at low temperatures, while at high temperatures the variation is much reduced. In fig. 6.22 the resistivity of the different as-deposited samples is presented. Regarding the residual resistivity, it is orders of magnitude greater than in the bulk raw noble metals and the shape is different as well. The residual resistivity must be related to the nanogranular character of the film with a presence of grain boundaries increasing the electronic scattering due to the increase of the structural disorder.

When the resistivity of the as-deposited and annealed Fe_7Au_{93} samples is compared (see Fig. 6.23), the main difference is the decrease of the residual resistivity in the treated sample ($1\mu\Omega cm$). Certainly, this is originated by the reduction of the density of grain boundaries. On the other hand, the shape is almost the same.

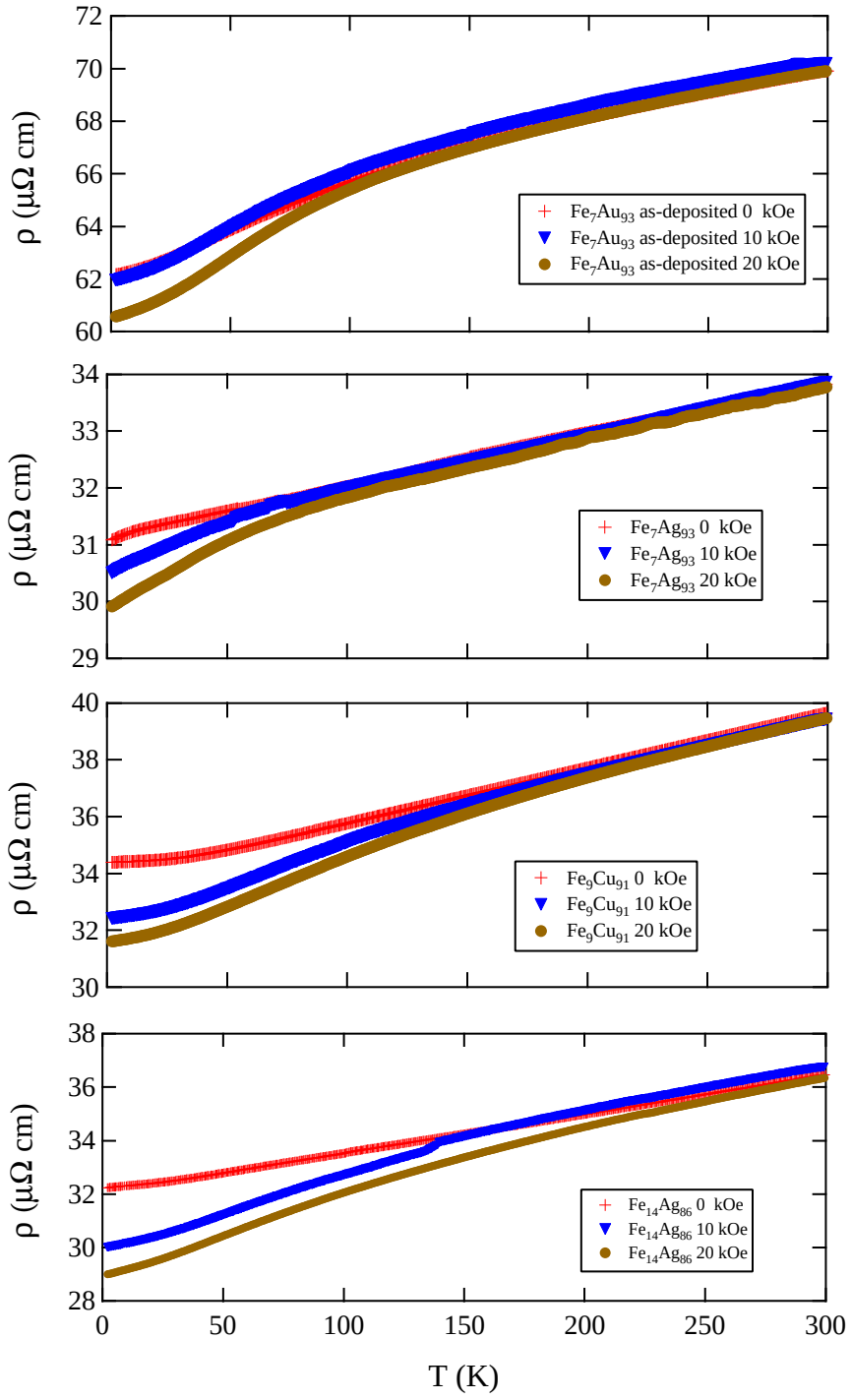

Figure 6.22: *Thermal dependence of the resistivity of the as-deposited films. All the alloys (despite the applied field) present a increase of the resistivity with temperature.*

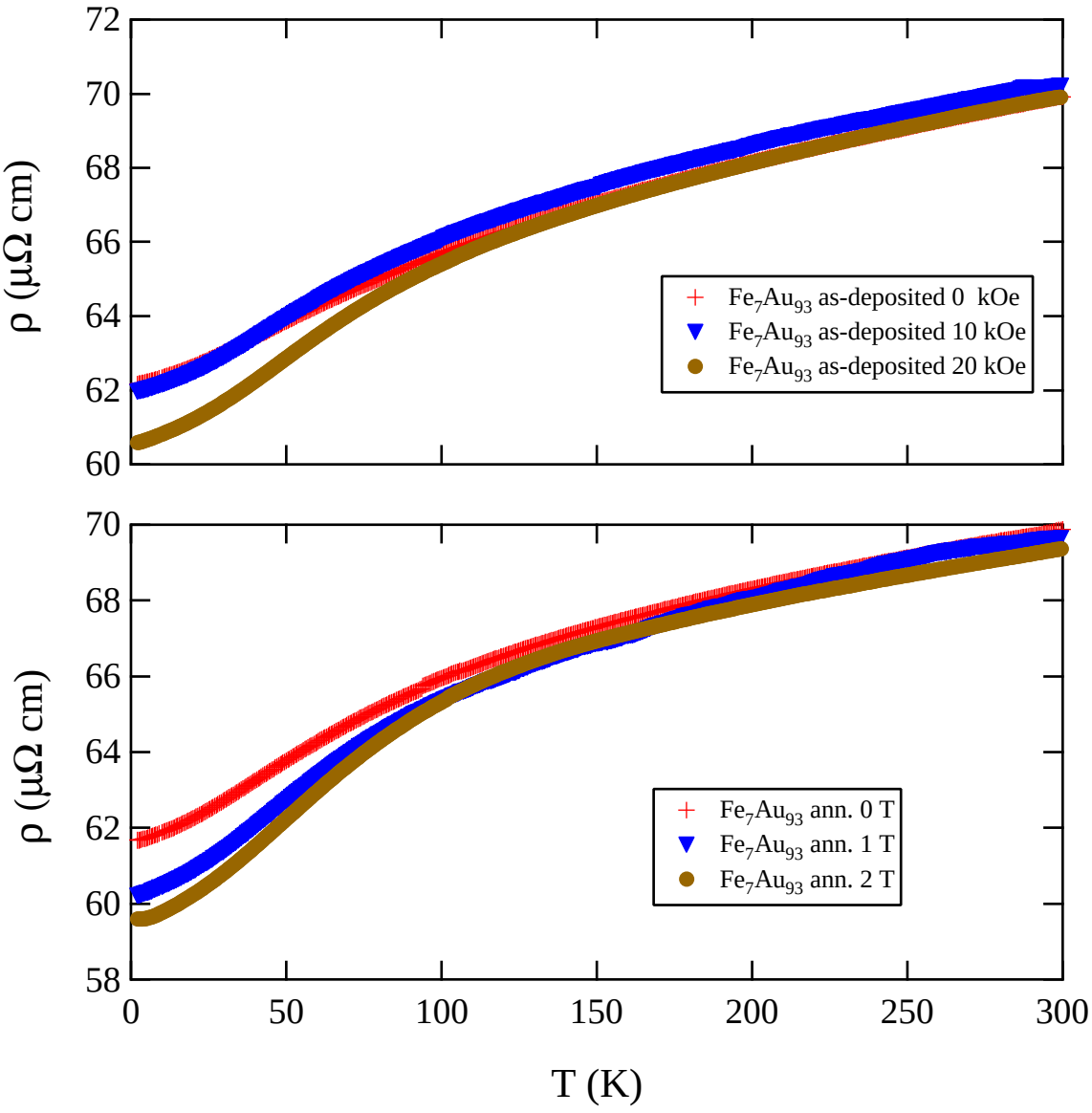

Figure 6.23: *Thermal dependence of the resistivity of both Fe_7Au_{93} as-deposited and annealed at 200 ^oC samples. The main difference between the samples is the reduction of the residual resistivity.*

It is remarkable the existence of an inflexion point (convex-concave variation) in the thermal dependence of the resistivity in almost all cases. For the Fe_7Au_{93} system (both, as cast and annealed) the inflection points are around 50 K; 44 K without a field, 48 K with $H = 10$ kOe and 50 K with $H = 20$ kOe. The Fe_7Ag_{93} does not present a inflection point

without an applied field, but there exists a point where the slope of the curve changes drastically: this is at 15 K. The inflection point is at 90 K at $H = 10$ kOe and 110 K for $H = 20$ kOe. The Fe_9Cu_{91} film presents the inflection points at 10, 70 and 70 K for $H =$ 0, 10 and 20 kOe respectively, where in the $Fe_{14}Ag_{86}$ they are at 11, 54 and 54 K.

6.5.2 Magnetic dependence

The field dependence of the ρ_{AC} (magnetoresistance), has been measured at fixed temperatures and between $H = 0$ and 50 kOe. At room temperature, the field does not have a significant effect on the resistivity. However, at lower temperatures, a negative magnetoresistance is manifest. The existence of a great negative magnetoresistance is a proof of the existence of magnetic nanoparticles [17, 18] in granular systems. It is related with the existence of an interface between the non-magnetic conductive matrix and the magnetic surface of the magnetic NP. The magnetic dependence of the systems can be observed in Fig. 6.24.

If the samples with and without a heat treatment are compared (Fig. 6.25), the same conclusion than for the as-deposited films is drawn: after the heat treatment there is a defined presence of magnetic nanoparticles, as the magnetoresistance value is still important.

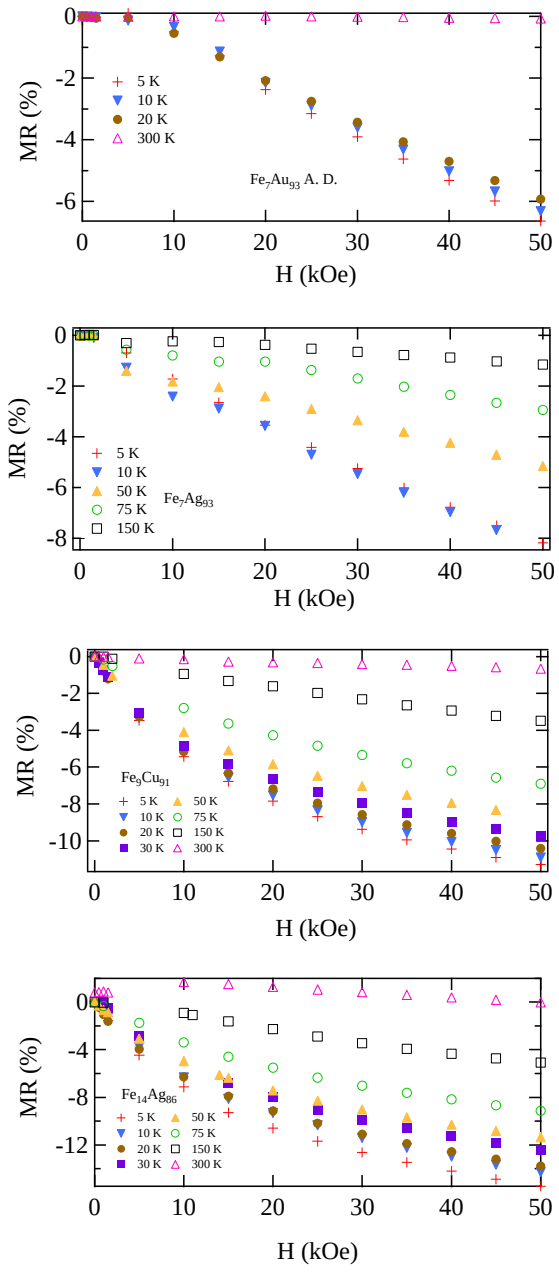

Figure 6.24: *Magnetic dependence of the resistivity for the Fe_7Au_{93} as-deposited (top),Fe_7Ag_{93} (middle top), Fe_9Cu_{91} (middle down) and $Fe_{14}Ag_{86}$ (down) alloys. Note that all the systems achieve a GMR larger than 6%, proving the existence of nanoparticles.*

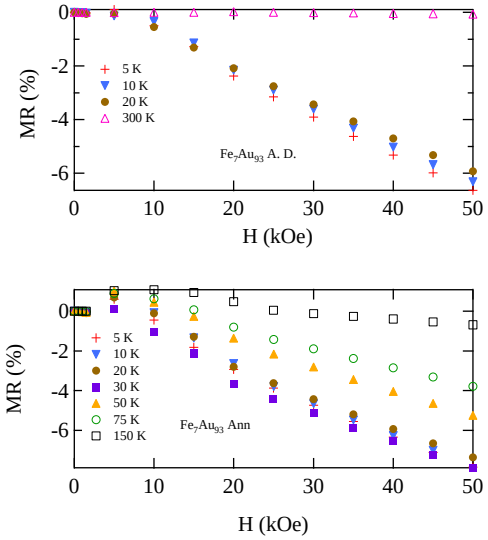

Figure 6.25: *Magnetic dependence of the resistivity for the Fe_7Au_{93} as- deposited (top) and Fe_7Au_{93} (bottom) annealed alloys.*

6.6 X-Ray magnetic circular dichroism

The X-Ray Magnetic Circular Dichroism (XMCD) is a powerful technique that combines magnetism and element specificity. In this work we have performed XMCD measurements in the Au edge of the Fe_7Au_{93} alloys as deposited and annealed at 200 °C. The normalised XMCD signal obtained at $T = 5$ K and $H = 50$ kOe of the Au-$L_{3,2}$ edges is shown in Fig. 6.26. No significant differences between both samples can be appreciated at first sight.

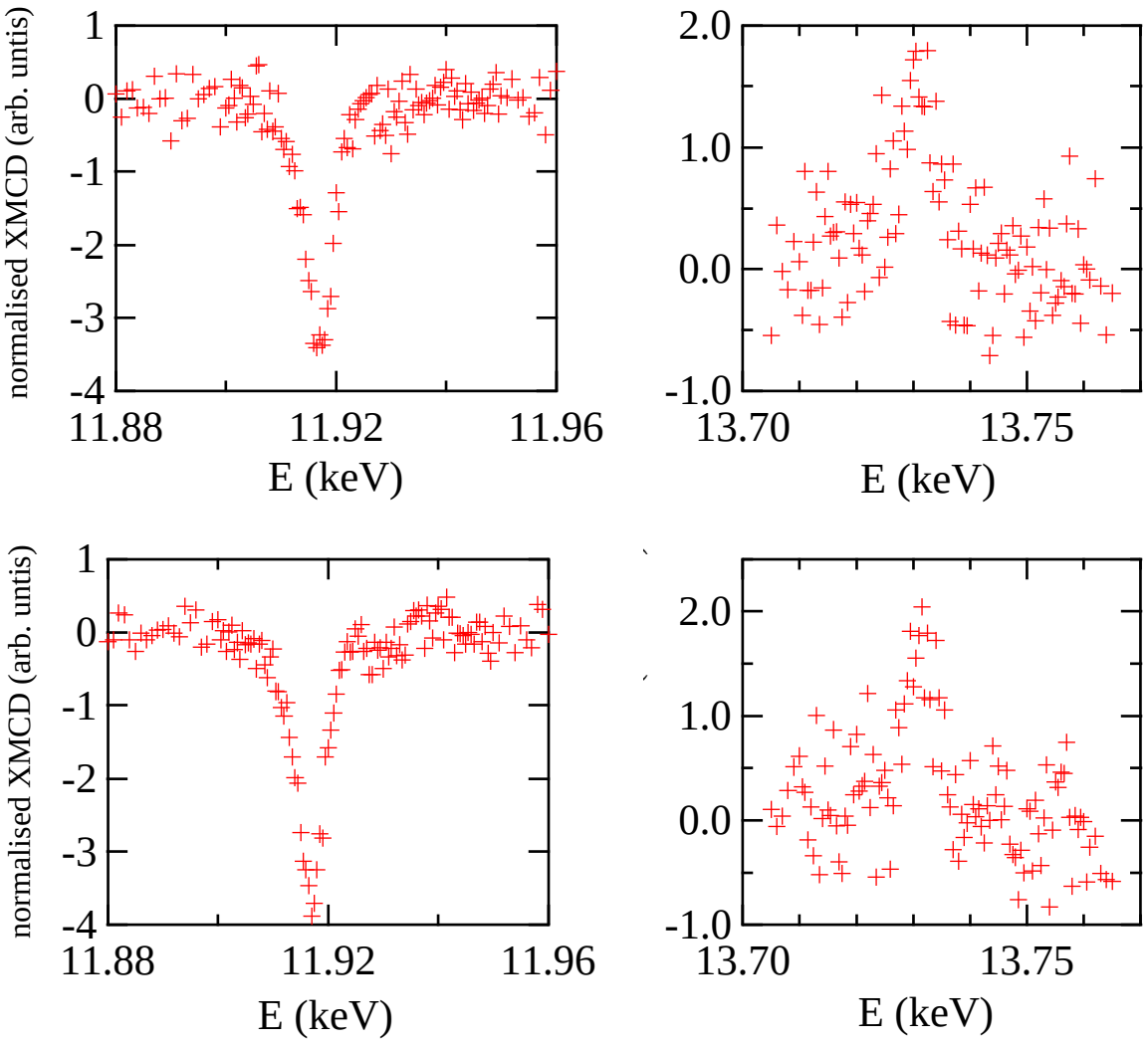

Figure 6.26: *Normalised XMCD spectra obtained at $T = 5$ K and $H = 50$ kOe. The upper panels represent the as deposited sample (L_3-edge left, L_2-edge right), where the annealed alloy is presented at the bottom part (again L_3-edge at the left and L_2-edge at the right).*

In addition, element specific magnetometry (ESM) has been performed at 5 K (see Fig. 6.27 and 6.28), being again both curves almost equal.

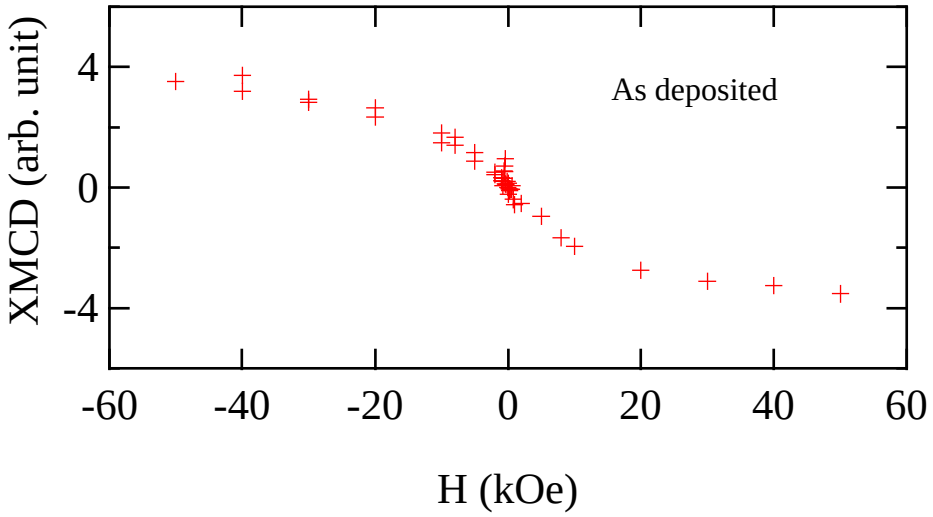

Figure 6.27: *Element specific magnetometry of the as-deposited film at 5 K. Note that the inversion of the picture in comparison with the regular hysteresis loops is originated by the negative XMCD signal of the L_3-edge.*

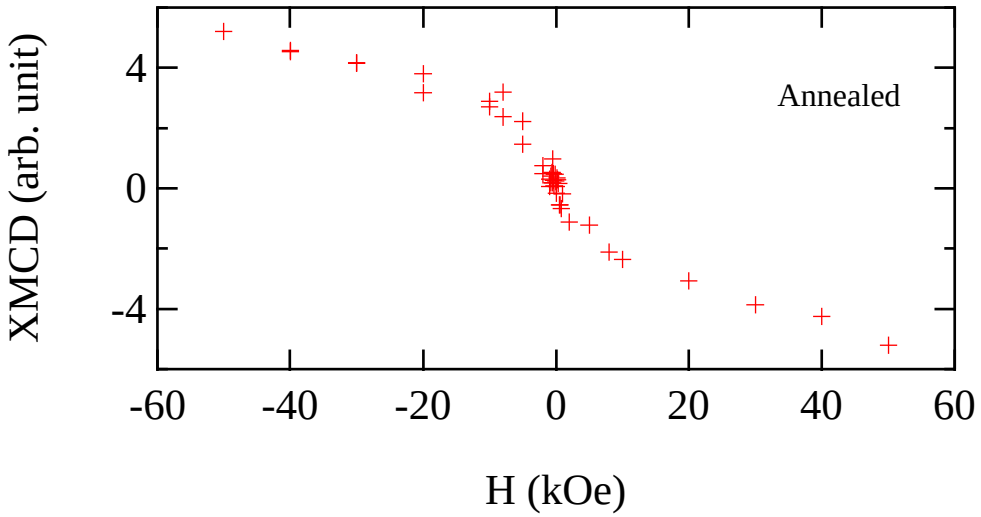

Figure 6.28: *Element specific magnetometry of the annealed alloy at 5 K.*

Finally, the Au L_3-edge was measured at RT (Fig. 6.29), without noticeable deviations between the as deposited and the thermal treated film.

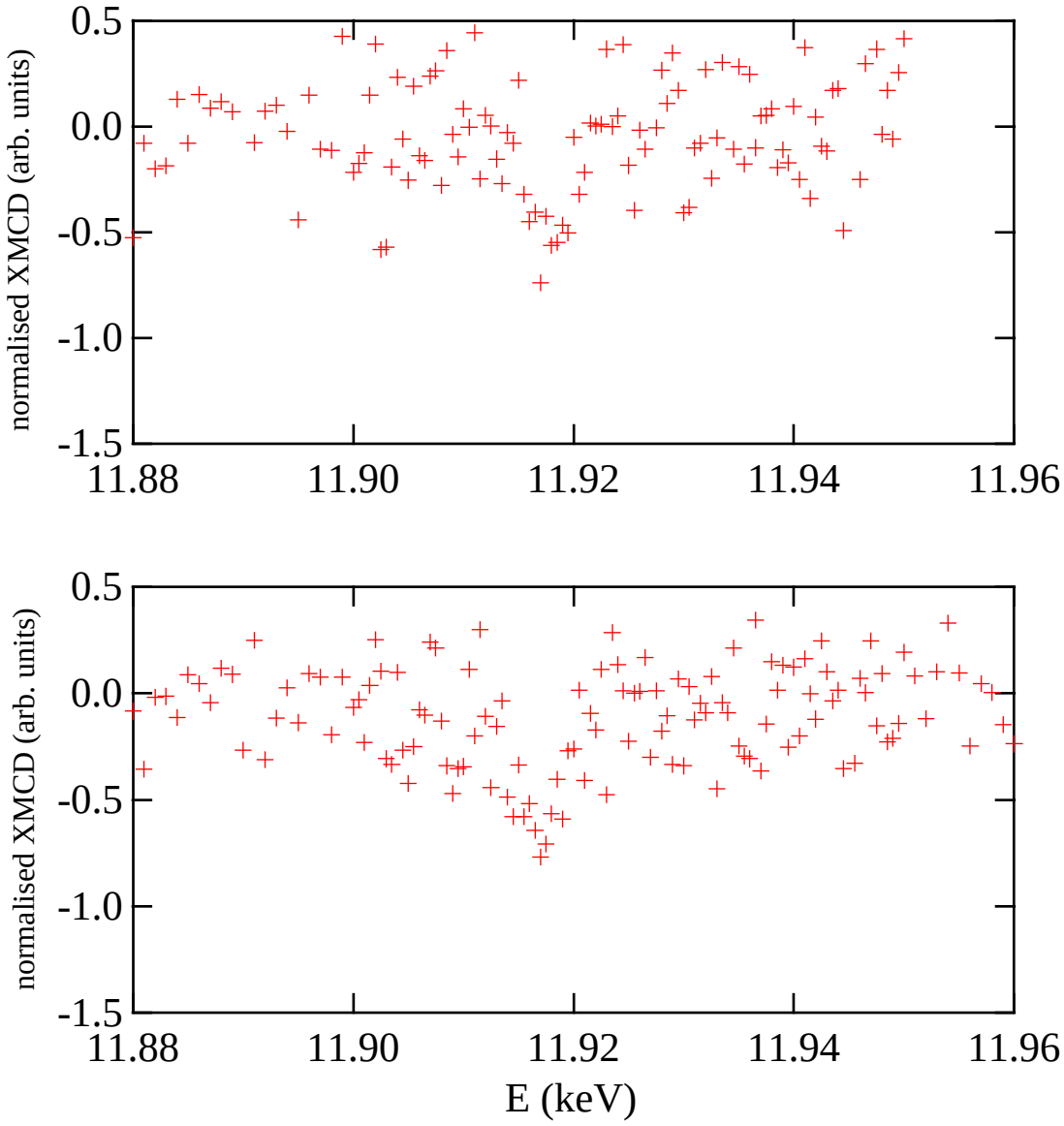

Figure 6.29: *XMCD spectra of Fe_7Au_{93} as deposited (upper panel) and annealed at 200 °C (lower panel). Again no clear differences are visible.*

All the XMCD measurements show similar values, without any significant deviation between the as-deposited and the annealed films.

Bibliography

[1] R. A. Young, editor. *The Rietveld Method*. Oxford university press, Oxford, 1993.

[2] D. B. Williams and C. B. Carter. *Transmission electron microscopy*. Plenum, New York, 1996.

[3] S. N. Kaul, V. Siruguri, and G. Chandra. Magnetization and Mössbauer study of the reentrant amorphous $Fe_{90}Zr_{10}$ alloy. *Phys. Rev. B*, **45**:12343, 1992.

[4] E. Dagotto. *Nanoscale phase separation and colossal magnetoresistance : the physics of manganites and related compounds*. Springer, Berlin, 2003.

[5] E. L. Nagaev. *Colossal magnetoresistance and phase separation in magnetic semiconductors*. Imperial college press, London, 2002.

[6] O. Petracic, X. Chen, S. Bedanta, W. Kleemann, S. Sahoo, S. Cardoso, and P.P. Freitas. Collective states of interacting ferromagnetic nanoparticles. *J. Magn. Magn. Mat*, **300**:192–197, 2006.

[7] S. Bedanta, T. Eimuller, W. Kleemann, J. Rhensius, F. Stromberg, E. Amaladass, S. Cardoso, and P. P. Freitas. Overcoming the dipolar disorder in dense CoFe nanoparticle ensembles: Superferromagnetism. *Phys. Rev. Lett.*, **98**:176601, 2007.

[8] L. Néel. Théorie du trainage magnétique des ferromagnétiques en grains fins avec applications aux terres cuites. *Ann. Geophys.*, **5**:99–136, 1949.

[9] J. A. Mydosh. *Spin Glasses: An Experimental Introduction*. Taylor and Francis, London, 1993.

[10] R. M. Bozorth. *Ferromagnetism.* IEEE Press, New Jersey, 1993.

[11] D. H. Ucko, Q. A. Pankhurst, L. Fernández Barquín, J. Rodríguez Fernández, and S. F. J. Cox. Magnetic relaxation in the nanoscale granular alloy $Fe_{20}Cu_{20}Ag_{60}$. *Phys. Rev. B*, **64**:104433, 2001.

[12] X. Batlle, X. Obradors, M. Medarde, J. Rodríguez-Carvajal, M. Pernet, and M. Vallet-Regí. Surface spin canting in $BaFe_{12}O_{19}$ fine particles. *Journal of Magnetism and Magnetic Materials*, **124**:228 – 238, 1993.

[13] J. Alonso. *Collective magnetic behaviours of Fe_xAg_{100-x} ($20 \leq x \leq 55$) granular thin films ans their structural characterization.* PhD thesis, Universidad del Pais Vasco, 2010.

[14] B. Martınez, X. Obradors, Ll. Balcells, A. Rouanet, and C. Monty. Low Temperature Surface Spin-Glass Transition in γ-Fe_2O_3 Nanoparticles. *Phys Rev. Lett.*, **80**:181, 1998.

[15] P. L. Rossiter. *The electrical resistivity of metals and alloys.* Cambridge university press, London, 1987.

[16] T. Sun, B. Yao, A. P. Warren, V. Kumar, S. Roberts, K. Barmak, and K. R. Coffey. Classical size effect in oxide-encapsulated Cu thin films: Impact of grain boundaries versus surfaces on resistivity. *J. Vac. Sci. Technol. A*, **26**:605, 2008.

[17] J. Q. Xiao, J. S. Jiang, and C. L. Chien. Giant magnetoresistance in nonmultilayer magnetic system. *Phys Rev. Lett.*, **68**:3749, 1992.

[18] A. E. Berkowitz, J. R. Mitchell, M. J. Carey, A. P. Young, S. Zhang, F. E. Spada, F. T. Parker, A. Hutten, and G. Thomas. Giant magnetoresistance in heterogeneous cu-co alloys. *Phys. Rev. Lett.*, **68**:3745, 1992.

Chapter 7

Discussion

7.1 Structural arrangement of the sputtered Fe_xM_{100-x} thin films

In the nanoscience world, the emergent new effects can not only are related to the chemical properties, but to the structural arrangement of the different components, which plays a fundamental role. In this sense, we have performed a deep work characterising the structure of the alloys down to the nanometric scale. We will start describing the results obtained by the TEM, especially the nanoparticle size distribution. Usually, the information gained by the electron microscopy should be complemented by a microstructural technique which spans a more representative sample volume, typically the XRD. This is used basically to check the crystallinity of the alloys, as well as the lattice parameters. Finally, the magneto transport will give further details of the structural arrangement of the magnetic (Fe) particles, which could not be obtained by means of the former techniques due to particular issues detailed below. An interpretation of the physical properties of the metallic nanostructures here described is only possible with the combination of data provided by the different techniques used in this work.

The "classical" structural techniques in nanoscience include frequently XRD and TEM. Here they also provide the frame on which the magnetoelectronic properties are inter-

preted. The XRD and the TEM show the nanocrystalline character of the different sputtered films, ruling out amorphous phases, at least in a significant amount. This contrasts with similar FeAg alloys fabricated by *Pulsed Laser Deposition* technique, which seems to favour the existence of an amorphous interface [1, 2].

XRD patterns reveal a (111) preferential orientation of the noble metals in the matrix since it intensity in comparison to those of the rest of the peaks is larger than in the case of polycrystalline powders. Besides, taking into account the scarce Fe amount in relation with the element of the matrix and its low atomic number ($Z_{Fe} = 26$ vs $Z_{Ag} = 47$ or $Z_{Au} = 79$), being the form factor proportional to Z, the Fe contribution is expected to be low and intricate to extract.

The TEM shows the presence of nanoparticles beyond doubt (see left inset of Figs. 6.3, 6.4 and 6.5). The size distribution assuming a circular shape of the particles, and considering a particle a region at the same Bragg condition, of the different system have been extracted and are shown in Figs. 7.1, 7.2 and 7.3.

The Ag-based film presents the smallest mean size ($D = 5.0$ nm and $\sigma = 0.49$), while the Au particle mean size distribution ($D = 6.2$ nm) is the narrowest ($\sigma = 0.37$). The Cu-based alloy present both, the biggest particle size and the broadest size distribution ($D = 9.5$ nm; $\sigma = 1.43$). Whether these effects are a product of the growing conditions, the selected matrix or both is unclear, and deserves further study concentrated more in metallurgical issues rather than in the magnetic properties.

In Fe_7Au_{93} and $Fe_{14}Ag_{86}$ systems the size distribution follows almost perfectly a log-normal distribution, as is expected for nanoparticles, including insulators [3] semiconductors [4] or metallic [5] produced by different routes. The Fe_9Cu_{91} size distribution follows better a simple Gaussian law. In this case the most probable diameter is large enough, so it is feasible to eliminate the constraint for the lowest value of the probability distribution function down to zero. This size distribution is less common but it has been found in Pt nanoparticles synthesised by chemical routes [6]. The size distribution obtained with the Dark Field (DF) (not shown) images matches roughly the sizes obtained by the conventional Bright Field (BF) images. However the number of counted particles is much lower

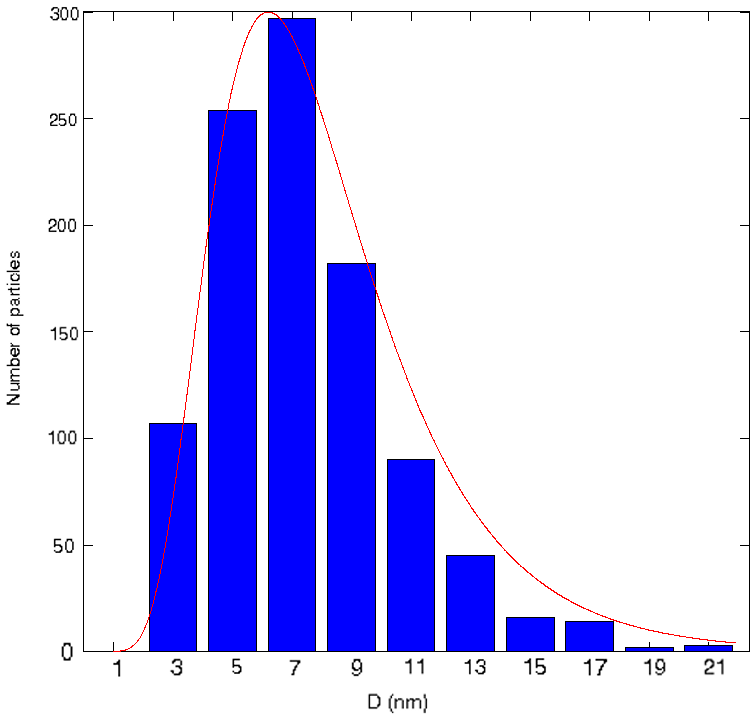

Figure 7.1: *Diameter distribution of the Fe_7Au_{93} obtained by TEM. The red line is the fit to a log-normal distribution, centred at 6.2 nm and with a $\sigma = 0.43$.*

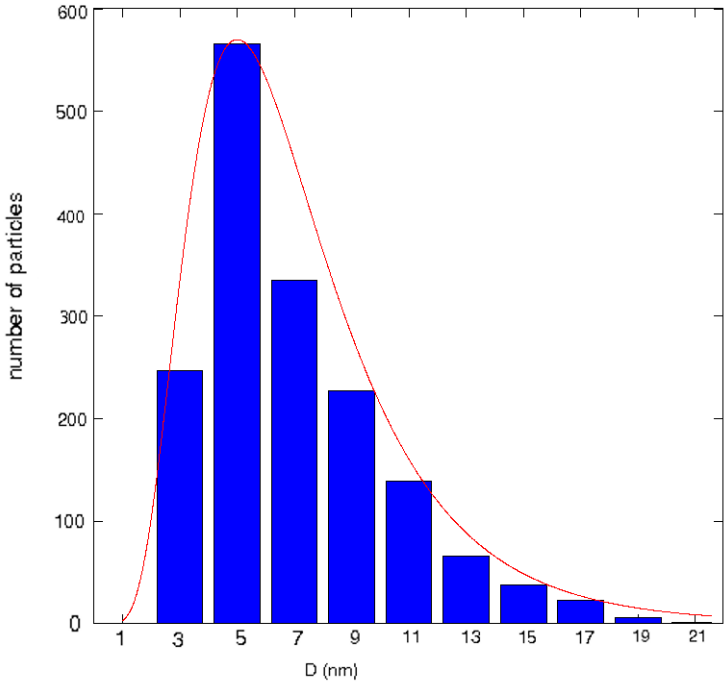

Figure 7.2: *Diameter distribution of the Fe_7Ag_{93} obtained by TEM. The red line is the fit to a log-normal distribution, centred at 5.0 nm and with a σ = 0.49.*

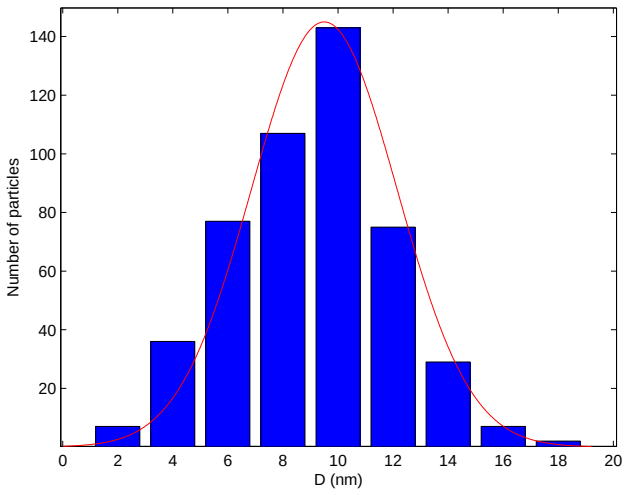

Figure 7.3: *Diameter distribution of the Fe_9Cu_{91} obtained by TEM. The red line is the fit to a Gaussian distribution, centred at 9.5 nm and with a σ = 1.43.*

implying an ill-defined statistics.

The definition of the exact size of the particle in relation to the boundary is somewhat blurred through out the TEM images. Our criterion was the selection of particles which are oriented in the same Bragg condition. To be rigorous, it should be reminded that the size of the Fe (magnetic) nanoparticles should not be related in a direct way with the obtained size distribution. In this sense, all the *electron-related* (imaging, diffraction or spectroscopy) techniques included in the Transmission Electron Microscope, have shown a great intermixing between the matrix and the Fe. Moreover, in the FeAu alloys there is some degree of mutual solubility (x $\simeq$ 1 % at RT), making the task even tougher. Previous works on arc melted Fe_xAu_{100-x} bulk alloys ($1 \leq x \leq 23$ % at.) [7, 8, 9, 10] discuss on the structure with the aid of various structural and magnetic techniques, including Mössbauer spectroscopy, TEM, diffuse scattering, SANS and SAXS. They debate thoroughly about the existence or not of Fe clusters leading to the onset of the ferromagnetism at relatively high x values, without reaching a consensus. The present work with continuous films is affected by a lack of definition of the TEM results, even if an exhaustive work has been performed (see section 5.5.2). Z. G. Li and coworkers reported the need of a discontinuous film to count with element sensitivity with the HAADF technique [11].

Moving forward to the HRTEM results, the mean interatomic distances are d_{Au} = 0.229 (2) nm, d_{Ag} = 0.252 (3) nm and d_{Cu} = 0.220 (6) nm. It is important to remember that the same selection rules applicable in the diffraction patterns should be taken in the the HRTEM images, since the contrast is given by the diffraction. The three metallic matrices present a $Fm-3m$ structure and thus, the first allowed reflection is the (111) plane. Transforming the measured distances into lattice parameters, they results in a_{Au} = 3.96 Å, a_{Ag} = 4.36 Å and a_{Cu} = 3.81 Å. The main advantage and the most serious drawback of the HRTEM is its local character. Although the resolution is high enough to separate atomic columns, only a very little portion of the sample is being examined. To overcome this problem it is a must to work with other techniques like the XRD, where the microscopic information obtained comes from the whole sample.

The XRD results provide a sensible structural information, but the overlapping of

diffraction lines between the components of the alloys is a serious obstacle for the discussion. In all the films, the most intense line is the Si (400), since the mass of the substrate is much greater than the metal deposition quantity. It is also present a (311) reflection from the substrate and a SiO_2 (111) reflection coming from the natural Si oxidation [12]. The Si (400) plane is used for calibrating the zero of the goniometer, since the substrate is a high purity single crystal buffer. The main information obtained by the XRD is the confirmation of the expected *fcc* structure for the noble metals and the *bcc* for the Fe and interatomic distances of the matrices. In addition, the presence of Fe is clear in the Fe_9Cu_{91} alloy. The values obtained for the noble metals are a_{Au} = 4.06 (2) Å, a_{Ag} = 4.06 (2) Å and a_{Cu} = 3.56 (2) Å compared to a_{Au}^{bulk} = 4.078 Å, a_{Ag}^{bulk} = 4.085 Å and a_{Cu}^{bulk} = 3.615 Å respectively. This may indicate that the surface of the particles is deformed, hence varying the crystallographic distances, but it should also be reminded the possible presence of some minor-quantities of Fe atoms in the noble metal. This solubility has also been reported in films of FeAg [13] and FeCuAg milled alloys [14]. The peak corresponding to the Fe phase is a_{Fe} = 2.88 (3) Å, marginally larger than a_{Fe}^{bulk} = 2.867 Å of the bulk. In consequence this reflect a Fe-environment.

The relative intensity of the peaks shows a preferential growth of the noble metal (111) face, since the intensity of the reflection is larger than that expected for a truly random polycrystalline distribution. In nanoparticle systems, the width of the peaks is an important parameter, it is a fingerprint of the mean size of the particle and the strain, the latter very much important in massive fabrication route such as mechanical milling [15, 16]. In films, the strain contribution is not supposed to be so important, and we roughly assume that all the peak width is caused by the size of the particles. The Scherrer formula can be applied to perform a simple estimation of the mean size of the nanoparticle:

$$D = \frac{\lambda}{\beta cos\theta} \tag{7.1}$$

where λ is the wavelength of the incoming X-rays, β is the width of the peak at the half maximum (in radians) and θ is the peak angle. Using this approximation, we obtain D_{Au} = 42 (5) nm, D_{Ag} = 30 (5)nm and D_{Cu} = 7 (2) nm. The values for the Au and Ag are

larger than the measured by TEM, but the value estimated by the XRD for the Cu matrix is smaller than the measured by TEM. Any other consideration (like inserting the strain of the samples and/or the instrumental width) will lead to an increase of the particle size, thus modifying the final result. It is a well-known feature to find different particle sizes for XRD and TEM. This discrepancy is often overlooked and justified by the different portion of sample analysed with both techniques. The core of the basic explanation to respond this is an intricate question is related to diffraction and crystallography which can be followed in specific reports [17].

To sum up, the discordance between both techniques is rather upsetting for both, interatomic distance and particles size. In the following we will use the XRD results for the interatomic distance and the TEM for the particle size. The XRD is chosen for the lattice constant: the number of measured lattices is several orders of magnitude larger in the XRD, and various reflections are taken into account. On the other hand, the TEM provides a direct measurement of the size distribution and enough number of particles, whereas in the XRD, that is a very indirect measure, affected by other parameters not used in this work, namely the instrumental broadening or the strain.

The XRD and TEM do not provide a clear cut conclusion about the magnetic nanostructure of the films, since they are not capable of determine Fe state. Despite this, the magneto-transport measurements are of greatest help to assure the presence of magnetic nanoparticles. In this sense the fundamental support is provided by the mechanism giving rise to Giant MagnetoResistance (GMR). GMR was discovered in stack of multilayers [18, 19], but it is also present in granular [20, 21] and spinodal decomposed systems [22]. The GMR in granular structures is typically explained by two different models. One of them, [23] attributes the spin dependent scattering to the s conducting electrons with the magnetic d electrons of the magnetic impurity. The other [24] attributes the spin dependent scattering to the existence of an interface between a non magnetic matrix and the magnetic nanoparticle. Both of them are connected on the one hand to the model of A. Fert regarding the spin-dependent scattering (band), and in the other hand the existence of clusters (nanoparticles). The latter is a must to observe GMR. As a reference,

bulk systems of Fe_xAu_{100-x} with almost the same composition, but comprising solved Fe atoms instead of Fe nanoparticles, present a magnetoresistance value one order of magnitude lower ($\Delta R/R = 0.8$ %) [25]. In our case (see Fig. 6.24), the $\Delta R/R$ is at least of 7% at 5 K, which contrast clearly with the just mentioned value. Hence, we can demonstrate the presence of nanometric Fe clusters. The values of the GMR present a great dispersion through literature, as it is a phenomenon related to the nanostructure of the sample and not purely related to the chemical composition, making difficult direct comparisons of the values. Systems with similar chemical composition present values comparable to our systems (24 % at 5 K for $Fe_{14}Ag_{86}$ thin films [26]) or much greater (50 % at 1.5 K for Fe_8Ag_{92} [27] or 3 % at 300 K for $Fe_{10}Ag_{90}$). The values of the GMR in the analysed films are not impressive but provide a very important result to conclude the nanogranular character of the Fe.

Another valuable analysis to ascertain the thin film nanostructure stems from the study of the variation of the resistivity with magnetic field (see. Fig. 6.24). For the most diluted samples (as-deposited Fe_7Au_{93} and Fe_7Ag_{93}), the magnetoresistance is almost constant at relatively low fields (below 5 kOe) and then there is a linear drop with the applied field. This result suggests the growth of the magnetic clusters with the applied field: when the field is low, the magnetic (spin) scattering centres are at random, so there is no spin dependent scattering. When the field is strong enough, there is a subtle magnetic cluster growth, triggering the GMR behaviour. For more concentrated samples (Fe_9Cu_{91} and $Fe_{14}Ag_{86}$) the MR follows almost perfectly a $H^{0.5}$ trend, like in many nanogranular systems [28], [29].

From an intuitive point of view, Gittleman *et al.* [30, 31] proposed that the magnetoresistance is proportional to the average value of the product of the magnetic moments of neighbouring grains:

$$MR \propto \frac{\langle \boldsymbol{\mu}_i(H_T) \cdot \boldsymbol{\mu}_j(H_T) \rangle}{\mu^2} \tag{7.2}$$

where $|\mu_i| = |\mu_j| = \mu$ are the magnetic moments of the $i-th$ and $j-th$ neighbouring grains and H_T is the total field experienced by the particle, including interactions with other grains. It is evident that: $\frac{\langle \boldsymbol{\mu}_i(H_T) \cdot \boldsymbol{\mu}_j(H_T) \rangle}{\mu^2} = \langle cos\phi_{ij}(H_T) \rangle$. The parameter govern-

ing the MR is the average angle between the moments. It is usually assumed that the anisotropy of the particles is random, the particles are noninteracting and the magnetic moments are uncorrelated [32], becoming eq. 7.2:

$$MR \propto \langle cos\theta_i \rangle^2 = (\frac{M}{M_S})^2 \tag{7.3}$$

where θ_i is the angle between the magnetic easy axis of the particle i and the applied magnetic field. In Figure 7.4 the variation of the magnetoresistance as a function of the square of the reduced magnetisation has been derived with the aid of the $M(H)$ data described in the section 6.4.2, presenting different behaviours. The Fe_9Cu_{91} follows well the previously described behaviour in eq. 7.3, whereas the other alloys (especially Fe_7Au_{93} and $Fe_{14}Ag_{86}$ films) present a deviation. This deviation is usually ascribed to magnetic interactions among the nanoparticles, as has been found in $Cu_{100-x}Co_x$ (x = 5, 10, 15) alloys [33].

In view of the above discussion, it is plausible to propose that the DC-magnetron sputtered nanometric films are formed by a collection of nanoparticles, predominantly of noble metal, together to some other of Fe-nanoparticles giving rise to GMR behaviour.

7.2 Magnetic behaviour of the sputtered Fe_xM_{100-x} thin films

In this work we have dedicated a great deal of attention to the understanding of the magnetic properties of these alloys. This task is delicate as several interconnected mechanisms may play a key role. Among these, the existence of interparticle interactions, the role of scattered spins in the interfaces, the random distribution of the magnetic single-domain particles and the contribution of the metallic matrix are necessary ingredients. In the following we will start with the magnetisation results in FC procedures at high fields and then we will follow with the details regarding the Curie-Weiss behaviour. The most valuable data for the magnetic nanostructures stems from the ZFC-M_{DC} and χ_{AC} will be presented subsequently. Finally, the thermal dependence of the coercivity reveals clearly

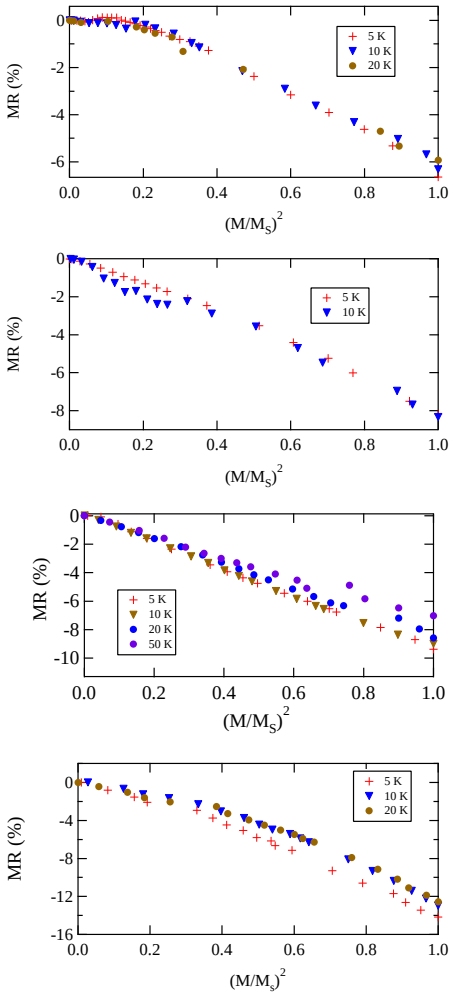

Figure 7.4: *Magnetoresistance versus* $(\frac{M}{M_S})^2$ *of the* Fe_7Au_{93} *as-deposited,* Fe_7Ag_{93}*,* Fe_9Cu_{91} *and* $Fe_{14}Ag_{86}$ *films respectively, at different temperatures below the transition (see below). Deviations from purely linear behaviour are patent.*

the weak coupling of the magnetic nanoentities and XMCD provides a local demonstration of the local polarisation of the noble metal (Au) particularly.

Since we are dealing with magnetic nanoparticles ferromagnetically coupled, it is convenient to pay some attention to the the magnetic excitations. For that purpose, FC measurements have been recorded under an applied field of $H = 45\ kOe$ (high enough to saturate most of the Fe nanoparticles) in order to study the thermal demagnetisation which should be governed at $T << T_c$ by the spin-wave. Magnons follow a $T^{\frac{3}{2}}$ law in bulk

materials [34]:

$$\frac{\Delta M}{M(0)} = 1 - BT^{\frac{3}{2}} \tag{7.4}$$

where B is a coefficient related to the exchange stiffness constant and T is the absolute temperature. In the case of bulk Fe, $B = 3.42$ x 10^{-6} $K^{-\frac{3}{2}}$ [35]. However, in nanoparticle systems, due to their finite size the spin waves present a discrete spectrum [36]. This is produced by an energy gap between the ground state and the first excited state, since the spin waves of less energy correspond to the larger wavelength excitations and those are truncated by the finite size of the FM nanoparticles. In general it is assumed that up to 0.15 T_C, such systems of nanoparticles follow :

$$\frac{M}{M_S} = A(1 - BT^{\alpha}) \tag{7.5}$$

where $\frac{3}{2} \leq \alpha \leq 3$ is a phenomenological parameter which reduces its value when the size of the particle grows, until reaching the bulk ($\alpha = \frac{3}{2}$) value. There is a wide range of α values for different NP systems [37]. An assembly of metallic $Fe_{0.78}Co_{0.22}$ with a mean diameter of 4.7 nm present $\alpha = 1.86$ [38]; in $BaFe_{10.4}Co_{0.8}Ti_{0.8}O_{19}$ oxide NP with platelet shape α is also greater than 3/2 ($\alpha = 2.7$) [36]. The discussion on the exponent variation has also brought in using Fe-based nanoribons produced by cold-rolling from Fe-Cu nanowires. In the latter case the $T^{\frac{3}{2}}$ dependence is modified and a linear dependence is reported when the shape changes [39]. This reduction was later theoretically explained adding a term corresponding to the chemical potential to the number of magnons excited at a certain temperature [40]. However, these interpretations are not conclusive; the influence of the spin-wave state discretisation has alternatively been observed in a large B prefactor (larger than in bulk) rather than exponent modification in 2 nm α-Fe nanoparticles dispersed in a SiO_2 matrix [41].

As shown in the previous chapter, even at $H = 45$ kOe, there is an upturn of the magnetisation at low temperatures. This behaviour (also observed in other systems comprising magnetic nanoparticles [41, 42, 43, 44, 45]) seems to be superposed to the classical spin wave relaxation. This fact is not yet fully understood. Some authors attribute the upturn to the existence of a very anisotropic shell of spins [42], others to the existence of

paramagnetic particles in the whole range of temperatures and fields [44] or this upturn is simply overlooked [41].

A straightforward approach is to fit the variation of the thermal variation of the "almost-saturated" magnetisation to a superposition of spin-wave plus a Curie-Weiss term [44].

$$M(T) = M(0)_{SW}(1 - BT^{\alpha}) + \frac{C}{T - T_C} \tag{7.6}$$

where C is obviously the Curie constant. The last term would take into account the mentioned upturn. Actually, a similar fit has been tried out in (C:Fe) nanoparticles in a carbon matrix. There, the Curie-Weiss term was attributed to a localised spin contribution of the C-matrix. The results of the fitting can be seen in Fig. 7.5. The fit was performed between 2 and 100 K, to assure the validity of the spin-wave relaxation (0.15 T_C [36]). In the plots the experimental points (cross markers), the fit (solid blue line), and the two different contributions: the spin wave (dotted line) and the Curie-Weiss one (lined/dotted line) are shown altogether. The fit results are summarised in table 7.1. The first salient result is that $\alpha = \frac{3}{2}$ is obtained in all cases, in agreement with Fe-SiO_2 [41]. Respect to the B coefficient, there is a tendency to decrease with the Fe-content, closing in to the bulk value, but still two orders of magnitude higher. Without an inelastic neutron experiment (which is non-viable in these films due to the low available mass and with the current neutron sources) that could determine accurately the spin wave excitation spectra, it is difficult to establish what of the previous models fits better to reality.

For C and T_c the variation is less clear, although it is true that the most Fe-concentrated alloy is the one with highest value for both parameters. Interestingly, two alloys with the same Fe-concentration present radically different values of C and T_c. This point towards a role of the metallic matrix. In this sense, the presence of such a Curie-Weiss upturn might be linked to the existence of a polarisation of the matrix and/or the presence of isolated Fe atoms. This will be described in detail later, when we discuss the mentioned XMCD results.

It is much more conclusive in nanomagnetic systems to discuss the ZFC/FC M_{DC} curves. This is due to the usual irreversivilities detected, which are related to the clus-

Table 7.1: *Summary of the results of fitting the thermal variation of the magnetisation at H = 45 kOe according to eq. (7.6).*

Sample	M(0)$_{SW}$ (10^{-3} $\frac{emu}{ccOe}$)	B (10^{-4} $K^{-\frac{3}{2}}$)	C (10^{-2} $\frac{emuK}{ccOe}$)	T$_C$ (K)
Fe_7Au_{93} AC	1.33 (3)	4.9 (2)	0.18 (8)	-2 (2)
Fe_7Ag_{93}	0.61 (13)	3.0 (2)	4.2 (18)	-50 (10)
Fe_9Cu_{91}	2.07 (5)	1.26 (13)	3.3 (3)	-14 (1)
$Fe_{14}Ag_{86}$	3.14 (7)	0.34 (11)	14.3 (7)	-97 (5)

tering. At low fields (or more strictly at the lowest available field to get a reproducible magnetic response), the main characteristic for all the as-deposited samples is the presence of a neat peak at low temperatures (ranging from 17 to 32 K for the different samples, see Table 6.2). This is typical in SPM and SG systems [46, 47]. For conventional spin glasses and SPM systems, the susceptibility above the peak is expected to follow a conventional Curie-Weiss law [46, 48, 49]:

$$\chi = A + \frac{C}{T - T_C} \tag{7.7}$$

with A an offset constant, C the Curie constant and T_C the Curie temperature. Despite the apparent quality of the fit (see Fig. 7.6), there are some important details which modulate the validity of the model.

If the magnetic nanoparticles were behaving as ideal SG or SPM there should be clear indications respect the fitted parameters. However we find serious drawbacks which are commented in the subsequent paragraphs. Firstly, the susceptibility does not fall to a zero value, A = 0, as it should be in a system at the ideal SPM (SG) state well above the transition temperature, showing that the systems are not completely relaxed at temperatures 250 K above the ZFC peak. Also, the values of the Curie temperatures obtained from the fits are much lower than the temperatures where the maximum value of the susceptibility is observed. In conventional ferromagnetic-paramagnetic transitions, the Curie temperature marks the phase transition temperature in a mean-field model. In NP systems, the blocking temperature is related with the point where the *superspins* begin to flip freely due to the large thermal energy compared to the anisotropy barrier. It

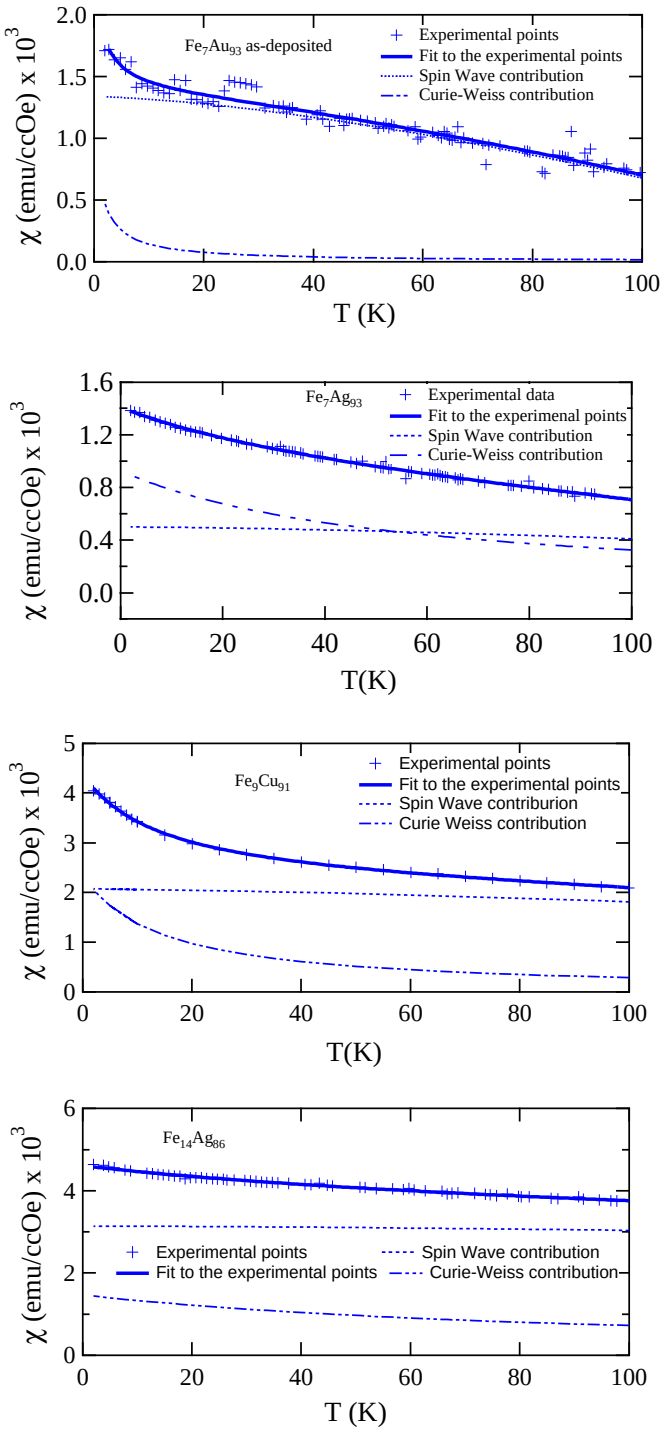

Figure 7.5: *Thermal dependence of the DC magnetisation at H = 45 kOe of the Fe_7Au_{93} as-deposited, Fe_7Ag_{93}, Fe_9Cu_{91} and $Fe_{14}Ag_{86}$.*

is evident from the ZFC M_{DC} measurements that both systems at such a low temperature are in a blocked/frozen state, where the *superspins* are trapped due to the existence of anisotropic barriers. Last but not least, the value of the Curie constant is related to the size of the nanoparticle:

$$C = \frac{xVM_s^2}{3k_b} \tag{7.8}$$

where C is the Curie constant, x the volume concentration of the magnetic nanoparticles, k_b the Boltzmann constant, M_s the saturation magnetisation and V the volume of each nanoparticle, respectively. Using (as in other Fe nanogranular systems [50]) $M_s = 1745$ emu/cc values for the NP radius of 4.4 and 5.1 Å are found. These values do not have any physical sense: supposing the Fe bulk anisotropy and a SPM behaviour, such small particles will not be magnetically stable above 0.075 K, which is obviously false. In the more Fe-concentrated samples ($x = 9$, 14), the Curie-Weiss law reproduces the experimental points, as can be seen in Fig. 7.7. Although the values are more realistic (especially the T_c), the C lead to particle sizes around $D \sim 1.5$ nm. This diameter is closer to reality but still too low.

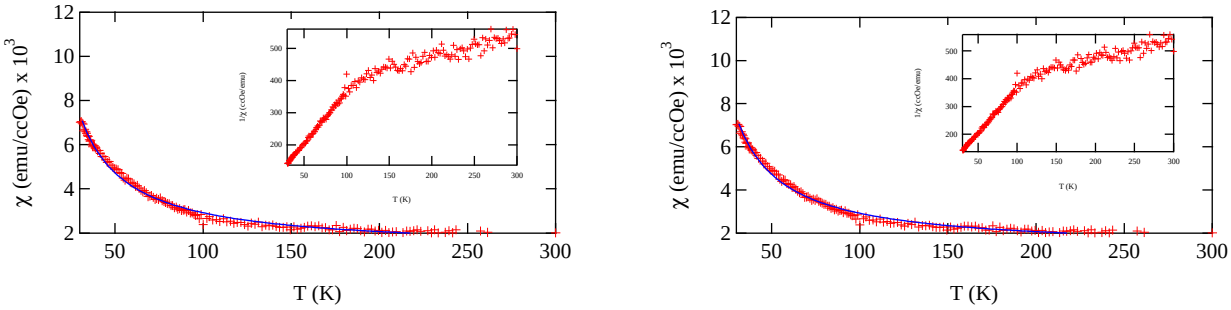

Figure 7.6: *Curie-Weiss fit of the susceptibility above the peak for the Fe_7M_{93} (M=Au, left; Ag, right). The markers represent the experimental points, while the line is the fitting. The values of the fit are $A^{Au} = 0.0013\ \frac{emu}{ccOe}$, $A^{Ag} = 0.0016\ \frac{emu}{ccOe}$, $C^{Au} = 0.137\ \frac{emuK}{ccOe}$, $C^{Ag} = 0.20\ \frac{emuK}{ccOe}$, $T_C^{Au} = 2.9$ K, $T_C^{Ag} = 3.0$ K.*

Another tool to evaluate the blocking/unblocking processes is provided by a model elaborated by E. P. Wohlfarth which is best applicable in SPM. The model uses a 3D magnetic relaxation and a uniaxial anisotropy. The expression for the susceptibility is:

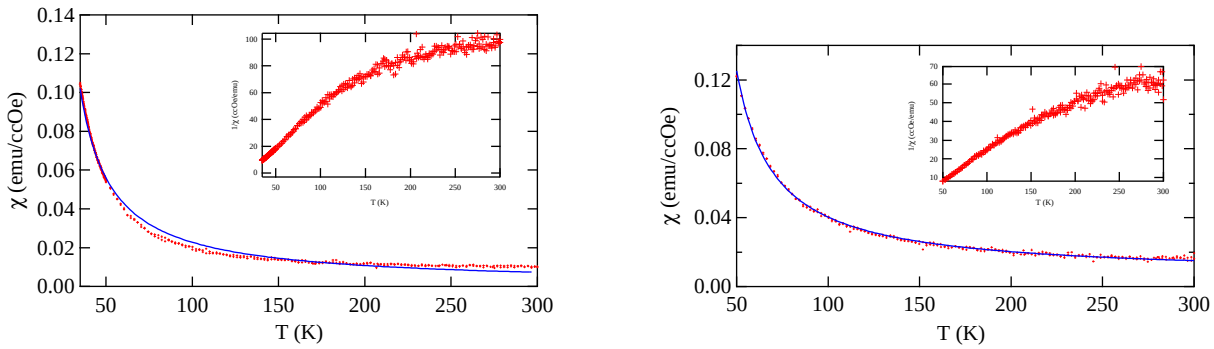

Figure 7.7: *Curie-Weiss fit above the peak for the Fe_9Cu_{91} (left) and $Fe_{14}Ag_{86}$ (right). The markers represent the experimental points, while the line is the fitting.The values of the fit are A^{Cu} = -0.002 $\frac{emu}{ccOe}$, A^{Ag} = -0.003 $\frac{emu}{ccOe}$, C^{Cu} = 1.2 $\frac{emuK}{ccOe}$, C^{Ag} = 2.2 $\frac{emuK}{ccOe}$, T_C^{Cu} = 22.3 K, T_C^{Ag} = 26.7 K.*

$$\chi_{ZFC}(T,t_m) = \frac{1}{\rho}\frac{m^2}{3K}\left[\frac{E_{bm}}{k_bT}\int_0^{\frac{T}{T_{Bm}}} yf(y)dy + \int_{\frac{T}{T_{Bm}}}^{\infty} f(y)dy\right] \tag{7.9}$$

where ρ is the density of the nanoparticles, m the static magnetisation, E_{bm} is the median of the energy barrier ($E_{bm} = KV_m$, with V_m the median of the volume of the particles), T_{Bm} is given by $T_{Bm} = \frac{E_{bm}}{k_bLn(\frac{t_m}{\tau_0})}$ where t_m the typical measurement time of the magnetometer and τ_0 the relaxation time of a single spin. The equation is composed by two different terms. The first one represents the contribution of the particles in the SPM state, where the second represents the blocked particles. $f(y)$ is the size distribution of the particles, and that is supposed to follow a log-normal dependence.

In our fittings we have fixed several obvious parameter, as $t_m = 100$ s, $\tau_0 = 10^{-9}$ s and $\rho = 7.874$ $\frac{g}{cc}$. The best fit gives a value of $D = 2.7$ nm, $K = 5.2$ x 10^6 erg/cc and $\sigma = 0.4$ (σ is the standard deviation of the size distribution). That value is close to that obtained in $Fe_{20}Ag_{80}$ (K = 3 x10^6 $\frac{erg}{cc}$) using the variation of the freezing temperature with the applied field [13, 51]. It is also in the range of the values obtained with the Wohlfarth fit for Fe(Cu) NP diluted in a Ag matrix fabricated by ball milling [21]. The fit is not working for our alloys, as it can be checked in Fig. 7.8, with a fit using a particle size distribution fixed at $D \sim 3$ nm. However the comparison between the calculated curve

and the experimental data help to understand that our diluted Fe_xM_{100-x} (M=Au, Ag, Cu), do not follow a SPM behaviour and, by contrast, the magnetic transition appears sharper, closer to what it is found in glassy systems.

The parallel work performed in Fe_xAg_{100-x} ($20 < x < 40$) produced by DC-magnetron sputtering provides an excellent comparative picture [50]. The ZFC M_{DC} curves present a relatively similar variation to those presented here. The freezing temperature ranges in Fe_xAg_{100-x} from $T = 86.5$ K for $x = 20$ to $T = 262.5$ K for $x = 45$, clearly larger, reflecting the higher Fe-concentration. In addition, there is also a decrease of T_B with the applied field, which will be explained later. In such films, an important finding was revealed connected to the change of SSG when $x < 35$ to SFM for higher concentrations.

Another more subtle unexplained feature is that the calculated Wohlfarth curve is not able to reproduce the shoulder appearing in the proximity of the peak maximum. This also should be explained by a more complicated picture, outside the assumptions of such a model.

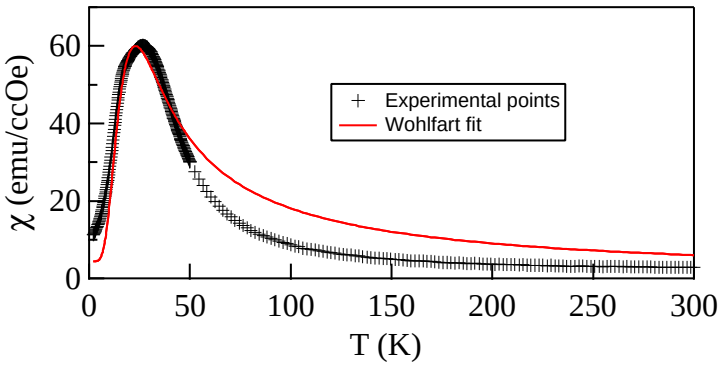

Figure 7.8: *ZFC data points of Fe_9Cu_{91} at 100 Oe and the Wohlfarth fit. Note that the experimental points fall much quicker than the proposed model, and that the structure of the peak is not reproduced.*

Finally and for the sake of completeness, it is also productive to take into account the maximum temperature of the ZFC process (see table 6.2). A very rough estimation of D based on the Néel-Arrhenius relaxation law can be rapidly estimated by means of the

Table 7.2: *Calculated diameters of the magnetic nanoparticles supposing an ideal SPM ensemble through the formula (7.10).*

Sample	T_B (K)	D (nm)
Fe_7Au_{93} A.D.	29	7.4
Fe_7Ag_{93}	17	6.2
Fe_9Cu_{91}	26	7.1
$Fe_{14}Ag_{86}$	32	7.6

formula:

$$T_B = \frac{KV}{25k_B} \tag{7.10}$$

where T_B is the blocking temperature, K the magnetic anisotropy, which will be supposed to be equal than in the bulk, V is the volume of the nanoparticle and k_B is the Boltzmann constant. As it can be inspected in table 7.2, the values are in the same order of magnitude ($\sim$ 7 nm) of that measured TEM nanoparticles. Nevertheless these values have to be treated as a rude approximation: we are not dealing with SPM systems, and has been proved beyond any doubt the enhancing of the magnetic anisotropy when the size is reduced. In any case it is a fair indication of the existence of magnetic clusters.

We now turn our attention to a striking detail which is the presence of an upturn in the FC magnetisation at very low temperatures. Some authors relate the FC upturn to solved atoms/subnanometric particles in the matrix [32, 52]. The variation of the slope with the field does not follow a particular trend, although it is true that the upturn is more pronounced in the Fe_7Ag_{93}. A microscopic interpretation is not clear but the previous explanation can also be applied in our case, with a finite presence of magnetic spins in the matrix.

In nanomagnetic systems it is expected that very small field changes provoke visible variations in the magnetic signals. In this sense, when the applied field in the DC-magnetisation measurements increases, there is a big broadening of the ZFC+FC (Fig. 7.9) peaks. This behaviour is common in other nanogranular systems [21, 47, 50, 53]. Usually the width of the ZFC peak is associated with the width of the size distribu-

tion of the magnetic nanoparticles. In addition, systems of magnetic NP with magnetic interactions (mainly dipolar) can also present broad peaks. At a fixed field, two different particles with different volume will have their blocking/freezing temperature slightly displaced, producing the mentioned broadening.

The field variation modifications can be explained in an intuitive form bearing in mind the effect of the applied field in a system with uniaxial magnetic anisotropy. When a magnetic field is applied, the degeneracy of the two fundamental magnetic states is lifted (remind Fig. 3.2). As it was already said, in the ZFC, the system is cooled down in the absence of a magnetic field, so the initial population of both magnetic states, in principle, should be the same. After that cooling, when a magnetic field is applied there is a lifting of the energy degeneration but then, the thermal energy is not enough to produce the magnetic transition of the superspins, pinned by the anisotropy.

While the system is warmed, at some point, the thermal energy will be sufficient to allow the transition of the superspins pinned in the excited state to the ground level. At high enough temperature, the thermal energy will be enough to allow the free fluctuation of the superspins. In SPM particles, the thermal energy needed to allow the transition from the excited to the ground magnetic state will be lower than in the absence of field ($\Delta E = KV$ - MH), since the energy barrier for those spins is smaller. The second effect is that the temperature needed to produce a free transition between both magnetic states will be greater ($\Delta E = KV + MH$), resulting in an increase of the blocking temperature.

If a moderate magnetic field is applied, the shape of the the ZFC peak changes (see Figs. 6.8-6.11). The well defined peak becomes flatter, and the shape resembles that of reentrant spin glass (RSG) systems. The magnetic field in our sample overcomes the anisotropy and enables a strong magnetic coupling among the nanometric magnetic entities (*bcc* Fe). As it was commented in the introduction, this phenomenon is nowadays interpreted within the so-called superferromagnetic behaviour (SFM).

Interestingly this cluster growth is not restricted to these particular nanostructured alloys. A similar claim has been reported in CeNiCu alloys [54] or in the exhaustively studied field of colossal magnetoresistive (CMR) oxides [55, 56]. In the latter, the clus-

tering effects stem from a competition between a ferromagnetic and an antiferromagnetic phases. When a static field is applied, there is a growth in the ferromagnetic phase, leading to a broadening in the peaks [57]. As in our system there is no antiferromagnetic phases, the mechanism of the cluster growth should be different. Another archetypal RSG alloy is amorphous Fe_xZr_{100-x} when $x > 90$ [58]. The interpretation of the glassy behaviour has been attributed to the existence of spin clusters as deduced from temperature-dependent Mössbauer analysis [59]. The cluster can become coupled as it was recently demonstrated by the variation of the spin correlation length estimated in SANS experiments [60].

Our proposition is that the lack of a clear Curie-Weiss, the shape changes with field and the shoulder of the ZFC peaks at low field are pointing towards the existence of a two-phase material in which there is a mayor presence of Fe-rich regions together with an interface of Fe-poor phase with different magnetic properties, consequence of different environments. At low applied fields the Fe-rich ensembles of ferromagnetic clusters are easy to be oriented. Where the magnetic field is larger, the surrounding Fe-poor regions become polarised, overall constituting a large ferromagnetically-coupled region. In this sense, the general behaviour is then close to that also concluded for the mentioned amorphous FeZr alloys [58, 59, 60]. In consequence, our nanostructured alloys behave as (cluster) super spin glasses in *modern* terminology.

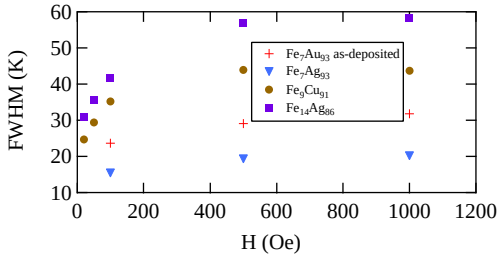

Figure 7.9: *Broadening of the ZFC peaks with the applied field. Despite having measures at higher fields, the decrease of the magnetization is not enough to have a measure of the FWHM of the peak.*

In this context, the ZFC process of a SPM and a SSG are very similar, both presenting maximum [47]. However, the FC response is different: in ideal SPM the FC magnetization

grows when the temperature decreases, while in SSG the FC magnetisation tends to saturate or even decrease [61]. In our particular case, the Fe_7Au_{93}, Fe_7Ag_{93} and the Fe_9Cu_{91}, after arriving to a maximum value at the same temperature than the ZFC, there is a little drop of the magnetisation followed by a rise at very low temperatures (although in the case of the Cu film the rise is feeble), just resembling other nanogranular systems [52]. On the other hand, the $Fe_{14}Ag_{86}$ only presents a more pronounced decrease in the magnetization at temperatures below the ZFC maximum. As commented above, both behaviours are characteristic of SSG systems, that is, the magnetic interactions among the nanoparticles are random and intense. In Fig. 7.10 the difference between the ZFC and the FC magnetisation can be more easily interpreted thanks to the plot of the χ difference: $\Delta\chi = \chi_{FC} - \chi_{ZFC}$. Thus it is possible to ascertain fine details of the disordered magnetic alloys, showing occasionally the presence of unexpected peaks as occurs in polycrystalline $Ni_{75}Al_{25}$ [62]. In most cases the FC and the ZFC merge at temperatures below or near the ZFC maximum. In Fe_7Au_{93} there is a small contribution between 20 and 80 K which may indicate a progressive blocking from some aggregated particles not detected with the structural techniques. Another variation is the abrupt change in the very low concentrated alloys (almost a linear increase), whereas in Fe_9Cu_{91} and $Fe_{14}Ag_{86}$ the variation of $\Delta\chi$ is more progressive, which may be linked with the mentioned upturn above commented. As expected, the irreversibility temperature is reduced when the strength of the magnetic field increases, being destroyed at high enough fields.

The obtention of T_f with a large number of fields enables us to discuss their implications according to different standpoints. In SPM the variation of the irreversibility, there observed as a blocking/unblocking process (T_B, blocking temperature) has been reported to follow a H^2-dependence as result of the use of the well-known expression [63]:

$$T_B = \frac{KV}{25k_bT}\left[1 - \frac{HM_s}{2K}\right]^2 \tag{7.11}$$

An alternative view is to consider a disordered magnet as a SG. In such a case, an Ising mean-field theory developed by Almeida an Thouless [64] predicts $\Delta T_f \propto H^{\frac{2}{3}}$. Agreement with this theory has been reported in metallic AgMn [65] and in nanometric γ-Fe_2O_3 [66].

More recently the discussion on this dependence has been revisited using multilayered sputtered films of Fe/Si_3N_4, in which a dependence of $T_B \propto H^{\frac{3}{2}}$ has been discussed [67]. The analysis of our data shows that neither of both ΔT_f dependence provide a good fit (see inset of Fig. 7.10). By contrast, a simple $T_{irr} = A'$ - $B'log(H)$ reproduces correctly the data. There is no explanation for this phenomenological dependence as fas as we are concerned, and consequently this issue remains as an open question. The values obtained in the fit are summarised in the table 7.3.

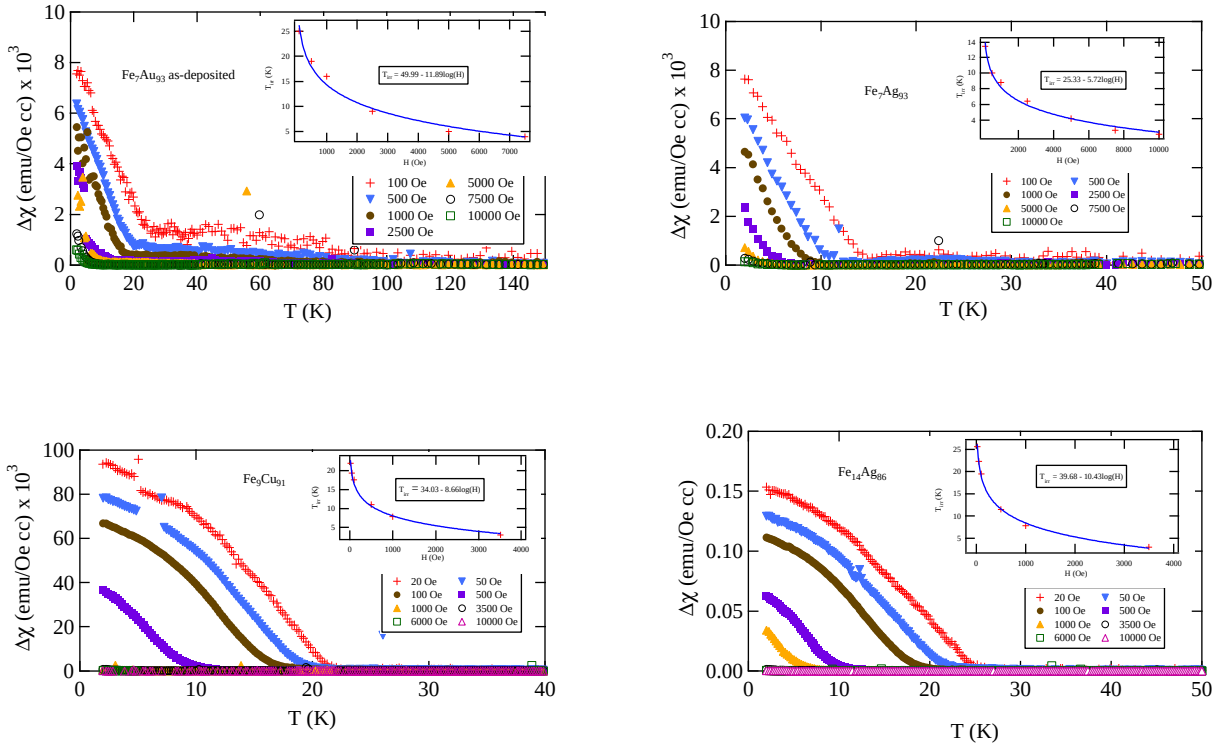

Figure 7.10: $\Delta\chi$ *of the different systems. The inset of the figures show the variation of the irreversibility temperature with the applied field which enables the observation of subtle details of irreversibilities behaviour.*

After discussing the variation of the relevant features in the ZFC-FC M_{DC} magnetisation, it is very instructive to interpret the hysteresis loops of the alloys. In nanomagnetic alloys comprising single-domain nanoparticles in a matrix following a SPM behaviour, it is expected that the M(H) variation follows a Langevin equation. In addition, for $T > T_B$,

Table 7.3: *Parameters of the fit for the phenomenological law* $T_{irr} = A'$ - $B'log(H)$.

Sample	A' (K)	B' (K/Oe)
Fe_7Au_{93}	50 (1)	12 (1)
Fe_7Ag_{93}	25 (1)	6 (1)
Fe_9Cu_{91}	34 (1)	9 (1)
$Fe_{14}Ag_{86}$	40 (1)	10 (1)

there should appear a perfect M/M_s vs H/T matching for the M(H) branches. Finally, the H_c should be zero above such a temperature. As it has been remarked previously, our films are not obeying the expectations of the ideal SPM and the hysteresis loops confirm such an statement. Fits to a distribution of Langevin equations are possible, but yield unrealistic values (for example, particle diameters $D \sim 0.6$ nm). Another more recent procedure (initially reported by P. Allia [68]) also predicts a temperature match of M(H) branches plotting M/M_s vs H/M_s for $T > T_f$. From figure 7.11 it appears evident that such a procedure does not produce a collapse of the curves. To end up, the coercive fields are $H_c^{Fe_7Au_{93}} = 169$ Oe, $H_c^{Fe_7Ag_{93}} = 191$ Oe, $H_c^{Fe_9Cu_{91}} = 170$ Oe and $H_c^{Fe_{14}Ag_{86}} = 36$ Oe at RT. All these statements confirms that no superparamagnetic behaviour is found in any of the alloys. This clear result contrasts with that obtained in Fe_1Ag_{99} [53] where a perfect SPM behaviour is claimed (the M/M_s vs H/T collapse is clearly observed). It should be noted that the deposition method of their films is totally different and it has been observed that different preparation routes result in a radical change of the particular magnetic properties, the latter intrinsically related to the changes in the nanostructure. Other analysis in more concentrated Fe_xAg_{100-x} films with a fabrication very close to the described in this thesis, have been reported showing very small coercivities (a few Oe) at RT [13]. These alloys present (in function of x) a crossover from SSG to SFM state, already commented [50].

The saturation magnetisation is not reached at fields up to $H = 50$ kOe, something usual for nanoparticle systems, since the Fe atoms on the surface of the nanoparticles present an enhanced anisotropy [43, 66, 69]. An estimation of the high-field susceptibility

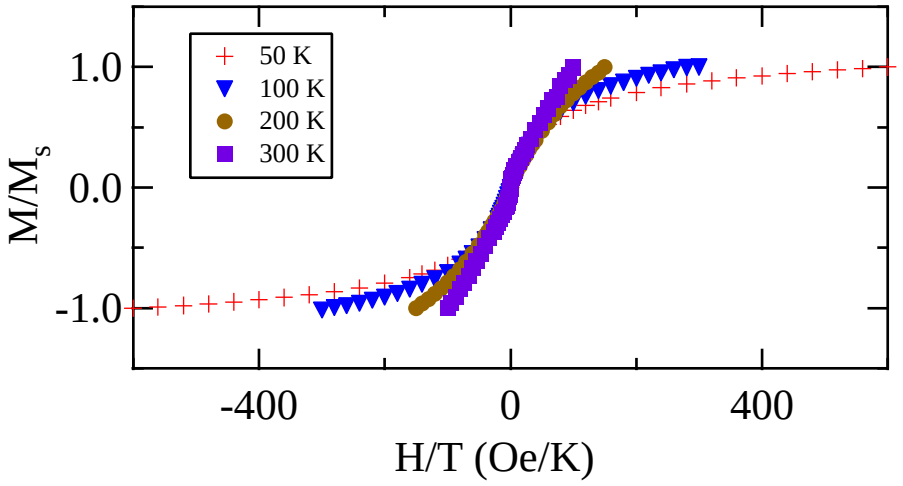

Figure 7.11: *Normalised magnetisation versus H/T is a common plot to check the SPM behaviour. In this graph absence of a collapse in the Fe_9Cu_{91} is presented as example.*

at $T = 5$ K is $M_{hf}^{Fe_7Au_{93}} = 10.7$ x 10^{-4} emu/ccOe, $M_{hf}^{Fe_7Ag_{93}} = 7.5$ x 10^{-4} emu/ccOe and $M_{hf}^{Fe_{14}Au_{86}} = 7.9$ x 10^{-4} emu/ccOe. The saturation magnetisation gives information about the total number of magnetic quantity that contributes to the system. Supposing that the sample is fully saturated and that the Fe in our samples conserve the bulk saturation magnetization (1745 emu/cc at 0 K) at such a high field it is possible to estimate the Fe quantity in the sample. This is interesting since our direct measurement of the sample composition through the EDX allows an estimation about how much Fe is magnetically *active*. The results have been inserted in table 7.4. Both, the EDX measurements and the estimation through the SQUID magnetometry are close, especially if we remind that the saturation is not fully reached. Although in the $Fe_{14}Ag_{86}$ the Fe content estimated by the magnetometry is higher than the measured by EDX, the values are within the experimental error.

We have suggested from DC- magnetisation that the films are formed by two regions with different Fe-contents. To establish this claim with a deeper support we now discuss the thermal variation of the coercivity. The coercive field is mainly linked to the magnetic anisotropy of the system and hence the coupling among the magnetic nanograins is a driv-

Table 7.4: *Comparison of the Fe volume in the sample obtained by EDX and by the saturation magnetisation. The measure and the estimation are close, taking into account the experimental error. The Fe_7Au_{93} film is in as-deposited condition.*

Sample	% vol (EDX)	% vol (SQUID)
Fe_7Au_{93}	6 (1)	4.4
Fe_7Ag_{93}	5 (1)	3.6
Fe_9Cu_{91}	9 (1)	8.0
$Fe_{14}Ag_{86}$	11 (1)	11.8

ing factor. In all samples, firstly there is an exponential fall of H_c when the temperature increases (see Fig. 7.12), followed by an attractive increase of the coercivity approaching RT. The higher value of the coercivity is linked to an increase in the effective anisotropy of the system.

In common magnetic nanogranular systems, the effective anisotropy falls strongly with increasing temperature. The fact that the $H_c(T)$ presents a minimum in the 2-300 K range points to the existence of a coupling/decoupling process. This minimum was also observed in FeNiCu melt spun ribbons, and was explained by the existence of two different ferromagnetic species, one with a low Curie temperature and the other with a Curie temperature above room temperature [70]. It also occurs in FeCu (metastable) alloys with spinodal decomposition [71, 72]. In consequence, this behaviour conducts to a confirmation of two different Fe environments, Fe-rich and Fe-poor (as shown in the thermal dependence of the magnetisation at high fields), since in principle a pure noble metal host would present a diamagnetic behaviour. Spinodal decomposition is excluded by the TEM pictures: there are no signs of modulation at the typical spinodal decomposed distances [22]. However, other disordered magnetic systems $Fe_{90}Zr_{10}$ in amorphous state present two different phases mediated by density fluctuations at the nanoscale [59]. The two phase behaviour has points in common with the *ultrasoft* nanocrystalline materials FeNbCuSiB [73] and the random anisotropy model. In the ultrasoft alloys, the exchange correlation length is greater than the actual particle size. This fact produce an averaging

of the anisotropy which should be scaled by the number of grains involved. In the case of this diluted thin film, when one phase (the *Fe-poor* phase, most likely) transits to the paramagnetic behaviour, the correlation length diminishes, provoking the rise in the average anisotropy.

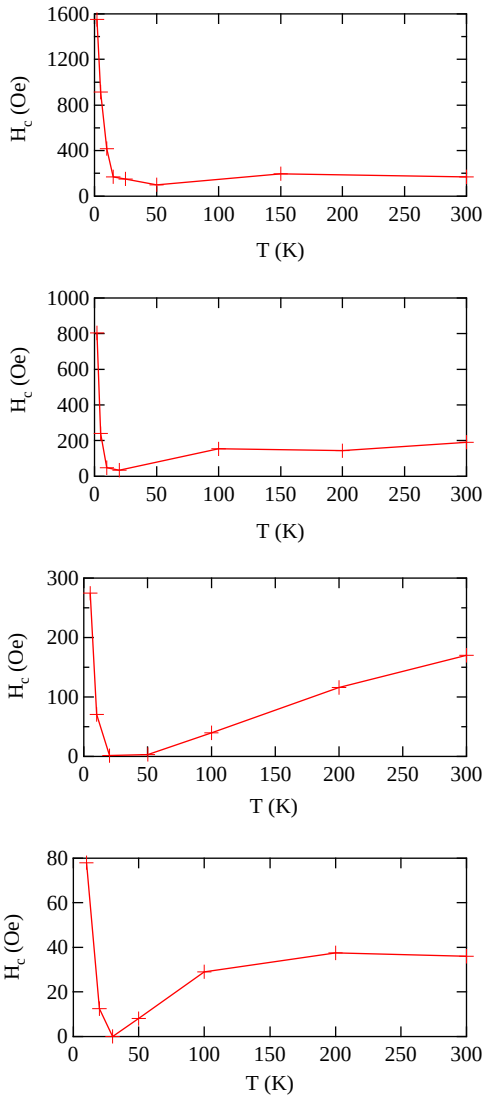

Figure 7.12: *Variation of the coercive field. The upper panel shows the Fe_7Au_{93} as-deposited, the middle-upper Fe_7Ag_{93}, the middle-lower Fe_9Cu_{91} and the lower the $Fe_{14}Ag_{86}$ samples. The increase of the coercive field above certain temperature is a particular and appealing behaviour related to the coupling/decoupling among nanograins. The lines are guides for the eye.*

The SSG state established at low temperatures is obviously presenting a spin dynamics which can be analysed by $\chi_{AC}(T)$. The low signal (SQUID detection limit) only allow us to measure the χ_{AC} in the most concentrated films: Fe_9Cu_{91} and $Fe_{14}Ag_{86}$. There is a neat frequency dependence of the freezing temperature. If the magnetic interactions are negligible or absent the spins rotation in the uniaxial anisotropy is produced by a thermal activation process, following the Arrhenius-Néel law (see eq. 3.3). However, when the magnetic interactions play a role (as it has been demonstrated beyond any doubt) the magnitude of the variation of the T_B with the frequency is reduced. The deviation is defined as [46]:

$$\delta = \frac{\Delta T_B}{T_B \Delta log\nu} \Rightarrow log\nu = \frac{1}{\delta} lnT_B + constant \tag{7.12}$$

In our particular case, the δ value obtained for the Fe_9Cu_{91} is $\delta = 0.0143$ (4) and $\delta = 0.0137$ (6) for the $Fe_{14}Ag_{86}$, close to spin glass (0.01 for the archetypal FeAu spin glass [46]), lower than the $Fe_{91}Zr_9$ cluster glass ($\delta = 0.066$) [74] or the CMR manganite $La_{1-x}Sr_xMnO_3$ ($\delta = 0.04$ [75]). Clearly it is very far from the predicted value of $\delta =$ 0.13-0.24 for non-interacting SPM systems. It is then clear that the alloys are entering into a frozen state at low temperatures. In this case, it is mandatory to look for a critical slowing down behaviour, very frequently reported in SSG materials [76, 77, 78]. Within this framework, it is expected that the spin correlation should diverge at the freezing transition following [79]:

$$\tau = \tau_0 (\frac{T - T_f}{T_f})^{-z\nu} \tag{7.13}$$

where τ_0 is the relaxation time, T_f is the freezing temperature and $z\nu$ a critical dynamical exponent. In Fig. 7.13 the excellent fit (R = 0.9919) can be inspected.

The parameters give $T_f = 31.5$ (2) K and $z\nu = 9.3(4)$ if $\tau_0 = 10^{-13}$ is assumed as a fixed value [80]. The high value of $z\nu$ lays within the *fragile* regime ($5 < z\nu < 11$) and it is common in other disordered magnets [76]. A free fit provides $\tau_0 = 4$ (2) x 10^{-10} s, $z\nu =$ 5.3 (5) and $T_f = 32.1$ (1), within the $z\nu$ laying in the same regime and τ_0 slightly larger. A Heisenberg spin glass model provides $z\nu = 5$ [81] and in Monte Carlo simulations of 3D Ising model $z\nu = 7.9$ [82]. Even larger values of τ_0 have been reported in the literature,

for instance $\tau_0 = 10^{-9}$ s have been reported in FeAg films [50] and $\tau_0 = 10^{-6}$ s in FeC interacting ferrofluids [83]. In some sense, the results of the free fitting suggest that the system follows a relaxation rate of the nanoparticles slightly lower than in conventional SG.

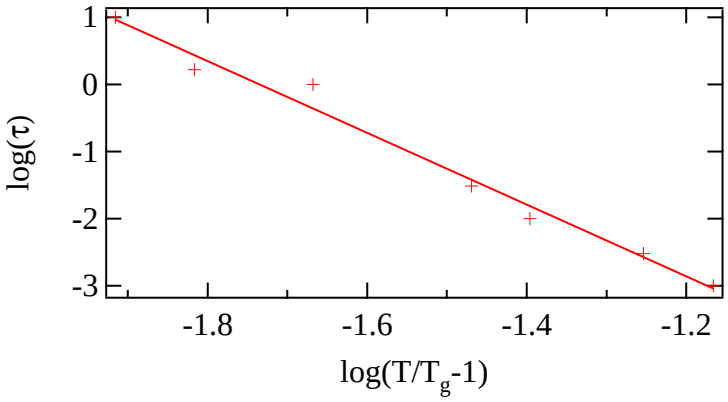

Figure 7.13: *Analysis of the $z\nu$ critical exponent according to a critical slowing down at the freezing transition. The red crosses represent the experimental points, while the solid line is the fit according to eq. (7.13).*

A Cole-Cole plot of χ'' vs χ' does not provide any clear result, although the semicircle expected for ideal SPM materials is clearly absent (see Fig. 7.14).

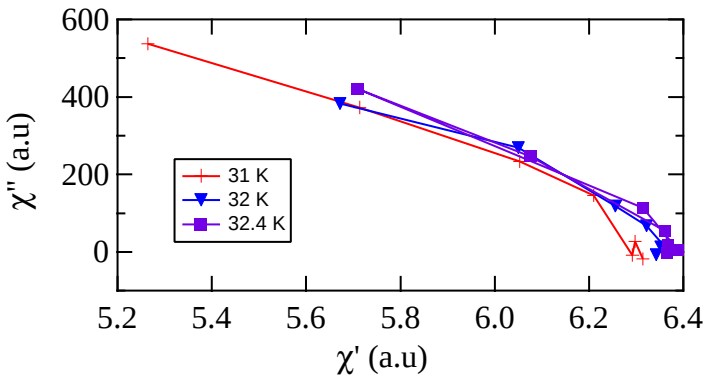

Figure 7.14: *Cole-Cole plots of the $Fe_{14}Ag_{86}$ film. As it is clearly deduced, the experimental points do not follow the semi-circle expected for SPM. Lines are guide a for the eye.*

It is a pity that we were not been able to record data in all the alloys, avoiding the

establishment of a trend. However, the results at hand indicate a dynamic spin behaviour close to a glassy relaxation, of nanometric entities in this case. The value of the $z\nu = 5.3$ is very close to the canonical spin glass ($z\nu_{CuMn4.6at.\%} = 5.5$ [46]) while the relaxation time ($\tau_0 = 10^{-10}$ s) is much slower than in the canonical systems.

As was shown in the previous chapter (see Fig. 6.26 and Fig. 6.29) the Fe influences the Au and induces a net magnetic moment. A microscopic analysis can be carried out with the aid of the the XMCD spectra and calculate the magnetic moment per Au atom. For this, the sum rules (see subsection 5.7.1.2) have been applied, as in other systems of metallic nanoparticles embedded in metallic non-magnetic matrices [84]. XMCD signals coming from both Au L_3 and L_2-edges can be well fitted by a Lorentzian profile, as it is shown in Fig. 7.15.

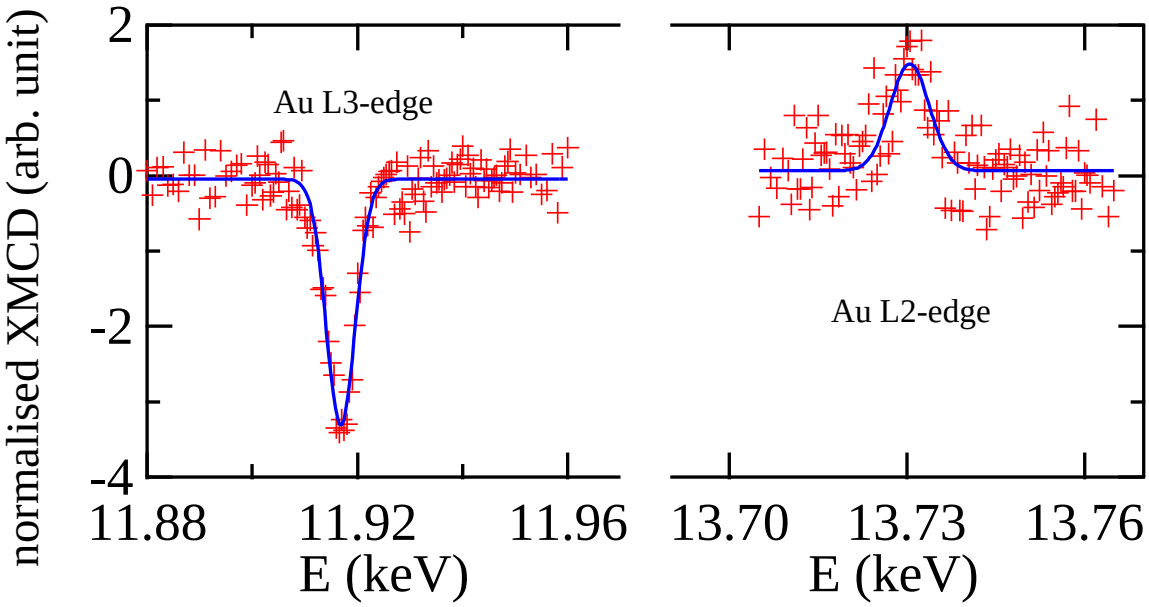

Figure 7.15: *Experimental points (red crosses) and fit (blue line) obtained for the XMCD signal at H = 50 kOe and T = 5 K for the as deposited alloy.*

From eq. 5.19 and 5.20 it is obvious that, the integrals of both XMCD signals should be calculated to quantify the magnetic moment of the Au atoms. The number of holes is an unknown parameter, although can be estimated. However, we can calculate the ratio

between the orbital and the spin magnetic moment avoiding this uncertainty. Specifically:

$$\frac{m_{orb}}{m_{spin}} = \frac{2q}{(9p - 6q)} \tag{7.14}$$

where p is the integral over both $L_{2,3}$-edge and q is the integral over the L_3-edge. In our particular case, the values p = -2.856 x 10^{-2} and q = -1.240 x 10^{-2} lead to $\frac{m_{orb}}{m_{spin}} = 0.1358$. The equation 5.20 can be rewritten as:

$$m_{spin} = \frac{3p - 2q}{C} \tag{7.15}$$

in systems of Co nanoparticles embedded in Au matrices [84], [85] the C value used is $C = 7.8\mu_B^{-1}$, leading to $m_{spin}^{Au_{AD}} = 7.81 \times 10^{-3}\mu_B/at.Au$ and $m_{orb}^{Au_{AD}} = 1.06 \times 10^{-3}\mu_B/at.Au$, and hence $m_{tot}^{Au_{AD}} = 8.87 \times 10^{-3}\mu_B/at.Au$. Supposing the bulk lattice parameters of Au occupying 94% of the volume, the Au matrix contributes with a net magnetisation $m^{Au_{AD}} = 4.6$ emu/cc at $H = 50$ kOe. Due to the low signal of the Au L_3-edge in absence of field,the ESM curve (see Fig. 6.27) is too noisy to say whether the Au magnetisation is aligned with the Fe nanoparticles or if it follows the external field. If the Au matrix were paramagnetic this could contribute to the FC upturn, and the $H_c(T)$ would be confirmed as consequence of two Fe environments.

7.3 Electrical transport of the Fe_xM_{100-x} thin films

In section 7.1, it has been shown that the films present a clear magnetoresistive behaviour with $\frac{\Delta R}{R}$ reaching 10% in some cases. On top of the technical implications, it is clear the usefulness of the electrical resistivity measurements. Surprisingly, there has been practically no attention to the thermal dependence of the resistivity $\rho(T)$. This somehow contrasts with the detailed studies of FeAu and other canonical SG [86]. It is probably the small and broad contribution of the SG to the resistivity which has prevented the analysis of the $\rho(T)$ in nanometric metals.

The upturn of the FC magnetisation in the Fe_7Au_{93}, Fe_7Ag_{93}, Fe_9Cu_{91} and $Fe_{14}Ag_{86}$ samples, has already commented but the resistivity provides a new point of view. In other

systems comprising magnetic nanoparticles embedded in a non-magnetic matrix [52] such an upturn is attributed to the existence of a low concentration of sub-nanometric magnetic particles with a paramagnetic behaviour in the whole temperature range. To check for the presence of isolated spins, it is possible to use the thermal dependence of the resistivity (without and with magnetic field). The reason for this possibility is that it is well-known that magnetic impurities can act as electronic scattering centres in metallic systems. Experiments of diluted Fe in a Cu matrix (ranging from 0.05 to 0.2 % at. Fe) display a resistivity minima (26 and 35 K, respectively) [87]. This effect was explained by J. Kondo as the result of the interaction of the *d*-electrons with the *s*-conduction electrons which also produced a subtle decrease of the magnetic moment. The increase of the resistivity (when decreasing T) behaves as a characteristic logarithmic dependence $\rho_{kondo} \propto Ln(T)$.

In every sample, there is an absence of a Kondo minimum (see Fig. 6.22). This experimental fact clearly rules out the presence of solved Fe atoms/subnanometric particles, at least in the Kondo range although it does not apply to the paramagnetic Au or noble metal. It should be noted that a recent contribution on melt spun CuCo [88] nanometric alloys, claims for the Kondo minimum intrinsically connected to the spin cluster existence. However the microscopic information reported there is limited.

Another remarkable result is the large residual resistivity compared to the bulk raw noble metals (0.001 $\mu\Omega cm$, for the bulk Au and Ag or 0.03 $\mu\Omega cm$ for the Cu [89] vs 62 $\mu\Omega cm$ for the Fe_7Au_{93}; 31 $\mu\Omega cm$ for the Fe_7Ag_{93}; 34 $\mu\Omega cm$ for the Fe_9Cu_{91} or 32 $\mu\Omega cm$ for the $Fe_{14}Ag_{86}$ thin films) or in the canonical SG with similar chemical composition (49 $\mu\Omega cm$) [90]. The origin of such an increase of the residual resistivity is not only related to the inclusion of the magnetic nanoparticles (which enhance the magnetic scattering of the conduction electrons) but also to the great number of grain boundaries (directly connected to the nanogranular character of the systems). The thermal variation of the resistivity is also larger than in the bulk alloys, proving the modification of the conduction band of the pure noble metal by the inclusion of the Fe nanoparticles in the matrix. Typically, in non-magnetic metals the electron-phonon scattering of $\rho(T)$ follows a Grüneisen-Bloch

law (GB) [89]:

$$\rho(T) = \rho_0 + K\frac{T^5}{\theta_D^6}\int_0^{\frac{T}{\theta_D}} \frac{x^5}{(e^x-1)(1-e^{-x})}dx \tag{7.16}$$

where ρ_0 is the residual resistivity, θ_D is the Debye temperature and K is a constant. This formula which is a solution of the Boltzmann's transport equation employs a Bose-Einstein distribution for the phonon spectrum. Considering that we are dealing with magnetic alloys and assuming the Matthiessen's rule (ρ is an additive sum of magnetic and electronic contributions), a magnetic term can be added to eq. 7.16, in the form of:

$$\rho(T) = \rho_0 + K_1\frac{T^5}{\theta_D^6}\int_0^{\frac{T}{\theta_D}} \frac{x^5}{(e^x-1)(1-e^{-x})}dx + K_2T^{\frac{3}{2}} \tag{7.17}$$

In the following, we will analyse the relative variation of the resistivity $\Delta\rho$ which is obtained subtracting the residual resistivity to the total ρ. Eq 7.17 is not able to fit all the temperature range (2-300 K) except in the more concentrated samples (see Fig. 7.16), and in both situations the magnetic contribution to the resistivity is feeble (more than six orders of magnitude smaller than the G-B term). Complex models specifically designed for systems comprising magnetic nanoparticles in a metallic matrix [91, 92] have been tried, without satisfactory results. One speculative explanation for the fail of these models resides in the possibility that the nanoparticles present a spin glass behaviour, contrary to the ferromagnetically coupled nanoparticles (aligned by the field) required by those models. In opposition to the broad peak in the $\rho(T)$ expected for canonical spin glass[46, 86, 90], a maximum is not present when the resistivity of the bulk matrix (Au, Ag or Cu) is subtracted to the system resistivity. Below T_f the total resistivity follows a $T^{\frac{3}{2}}$ law. This is a similar variation to that of the canonical SG and contrasts with the expected T^5 GB dependence.

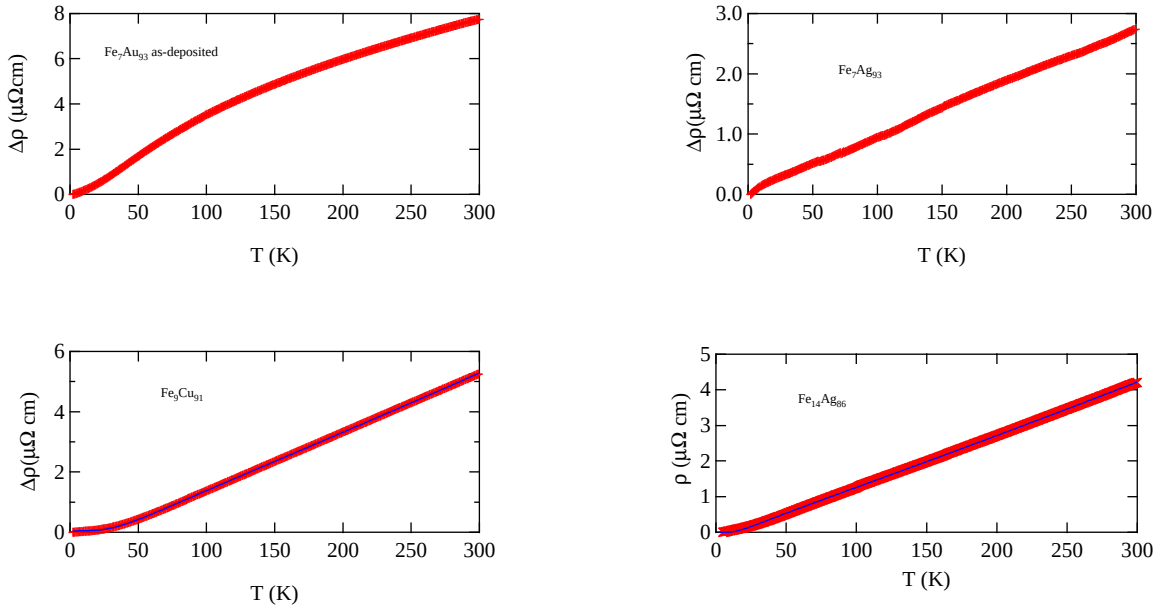

Figure 7.16: $\Delta\rho$ *of* Fe_7Au_{93} *as-deposited (upper left),* Fe_7Ag_{93} *(upper right),* Fe_9Cu_{91} *(down left) and* $Fe_{14}Ag_{86}$ *(down right). Only the* Fe_9Cu_{91} *and* $Fe_{14}Ag_{86}$ *thin films follows a Grüneisen-Bloch + a magnetic term law in the whole temperature range, with a Debye temperature of 227 (3) and 95 (1) K, more than 100 K lower than the pure bulk Cu and Ag, respectively.*

The Thermal Coefficient of the Resistivity (TCR) is defined as:

$$TCR = (\frac{d\rho}{dT}\frac{1}{\rho_{300K}}) \tag{7.18}$$

has been calculated for all the alloys. The obtained values are lower than those for the crystalline components of the films, but are mixed within the values of the canonical spin glasses and magnetic disordered amorphous alloys, as can be deduced from the data compiled in table 7.5.

Table 7.5: Resistivity and TCR of the different alloys used in the current work, and other metals in crystalline and amorphous state for comparison. The data for bulk metals have been obtained from [89], the bulk spin glasses from [86] and the value of the (amorphous, *a*) *a*-$Fe_{90}Zr_{10}$ from [93] and the value for *a*-$Co_{75}B_{25}$ from [94].

Metal	$\rho_{300K}(\mu\Omega cm)$	TCR (K^{-1}) x 10^5
Fe_7Au_{93}	69.9	24.0
Fe_7Ag_{93}	33.8	9.2
Fe_9Cu_{91}	39.6	48.7
$Fe_{14}Ag_{86}$	32.3	41.3
Bulk Au	2.18	324
Bulk Ag	1.60	328
Bulk Cu	1.73	362
Bulk Fe	9.79	464
Fe_1Au_{99} S.G.	9.3	66.7
Fe_2Au_{98} S.G	17.46	35.5
Fe_5Au_{95} S.G	41.89	6.19
Fe_8Au_{92} S.G	55.18	19.9
a-$Fe_{90}Zr_{10}$	122	12.0
a-$Co_{75}B_{25}$	137	27.4

Following the typical analysis for SG resistivity $\rho(T)$, we obtain the variation shown in Fig. 7.17. Two salient features are evident: i) The shape of the curve does not follow that expected for bulk SG, and ii) the magnitude of the residual resistivity is around 50 $\mu\Omega cm$, much higher that in $\Delta\rho$ CuMn $\sim$ 10 $\mu\Omega cm$. This is another confirmation of the presence of nanocrystals contributing to an excess of the resistivity.

With the aim of gaining some extra information, we will discuss the effect of the magnetic field on the electrical transport. The thermal variation of the resistivity has been recorded with an static magnetic field of $H = 20kOe$. In the Fe_7Au_{93} as-deposited system (Fig. 7.18), all the resistivity curves vary with the same slope at high temperatures.

The effect of the magnetic field is to shift up both the inflection point of the curve and the temperature where the final slope of the curve is reached, towards higher temperatures. The fact that the high temperature slope of the resistivity tends to a constant value despite the field reflects the progressive decrease of the magnetoresistance when approaching higher temperatures. Interestingly, there is a marked change of slope around 50 K in the $\Delta\rho(T)$ which deserves some attention (see Fig. 7.18). A general inspection of Fig. 7.18 shows a definite change of the slope, more clearly visible observing the peak in the derivative (inset). The peak temperature (around 50 K) is slightly larger than the corresponding T_f for all the alloys. It should be reminded that the peak in ρ_{mag} for ideal SG was also slightly higher than T_f [46]. So it may be inferred that the origin is due to a magnetic change in the Fe nanoparticles. Research in this particular feature is surprisingly scarce, although some models connect these aspects: the cluster size and width and the distribution of random molecular fields [92].

The measurements of $\rho(T)$ have provided new information for the global understanding of the magnetic behaviour of the films. Particularly, a crucial result is the absence of Kondo behaviour, narrowing the amount of solved impurities in the matrix. In addition it has been established the small magnetic contribution to the total resistivity at high temperatures, with a shape which does not follow the typical trend found in SG. Finally the thermal dependence of the resistivity measured under a magnetic field, shows an inflection point already reported in GMR CoAg films [91], but we think this can be an open field of future research.

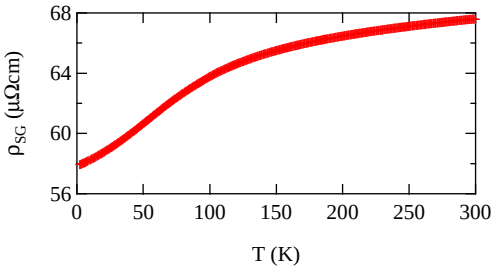

Figure 7.17: *Difference of the resistivity of the Fe_7Au_{93} as-deposited minus the Au bulk resistivity. The typical broad peak of the SG resistivity does not appear.*

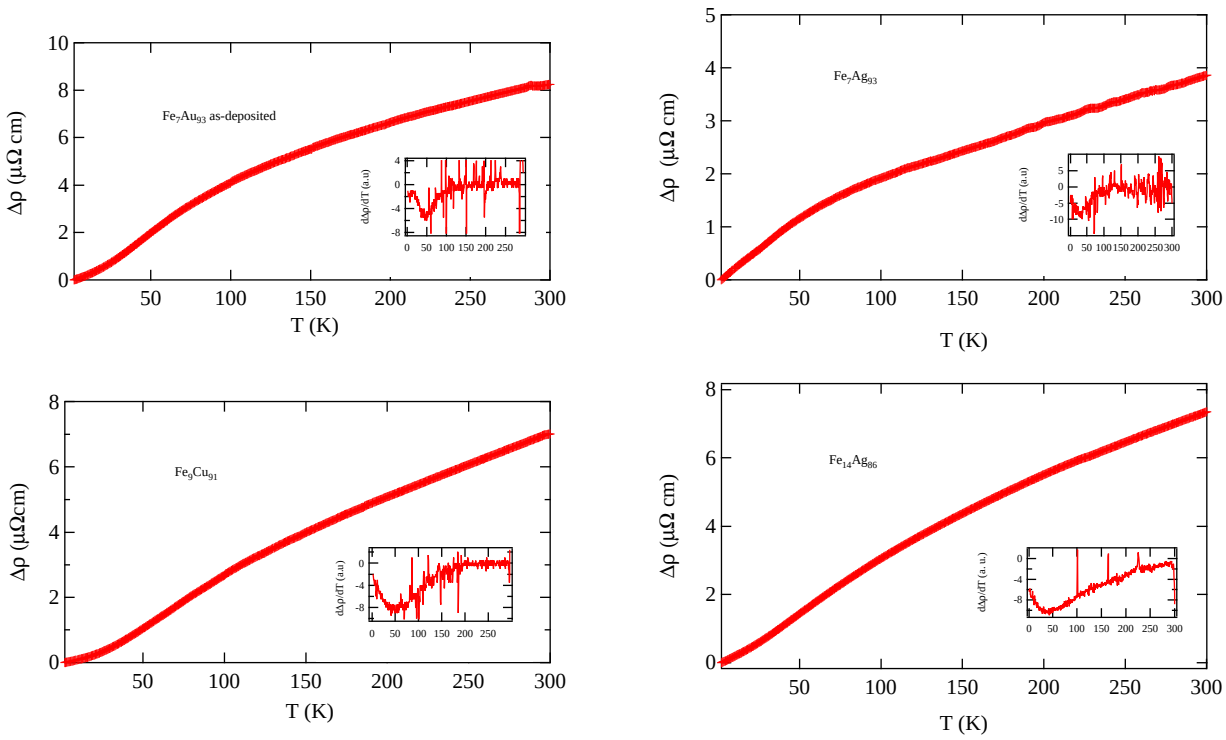

Figure 7.18: *$\Delta\rho$ of Fe_7Au_{93} A.C. (upper left), Fe_7Ag_{93} (upper right), Fe_9Cu_{91} (down left) and $Fe_{14}Ag_{86}$ (down right) with an static field of 20 kOe (right). The inset shows $\frac{d(\Delta\rho_H - \Delta\rho_{H=0T})}{dT}$. All the samples present an inflection point in the variation of the resistivity with temperature.*

7.4 Annealing of the Fe_7Au_{93} thin film

The annealing of metastable alloys is a normal procedure to extract valuable information on whether the magnetic (structural) clusters are present [95]. A number of alloys have been annealed during 1h at 50 °C, 100 °C, 150 °C, 200 °C and 250 °C. In this discussion we will concentrate on the properties which could be modified by the thermal treatment. In this sense, the magnetoresistance measurement (see Fig. 6.25) shows a clear GMR behaviour with a $\Delta R/R = 8$ % at 5 K. Again, the MR measurements confirm the existence of magnetic nanoparticles, and the larger MR value should be connected to an increase of either the number of magnetic centres of scattering and/or a growth of the NP surface and hence, the existence of bigger particles.

The ZFC-FC M_{DC} magnetisation results are extremely revealing. The FC presents

different regimes at low fields: there is a peak at $T \sim 32$ K which divides the curve in two. When the field increases the position of such a maximum remains almost constant (see Fig. 6.13). The ZFC process is very clear; there is again a well-defined peak at a similar temperature than in the FC peak but there exists a broad hump between 70 and 200 K (see Fig. 7.19 for a direct comparison between the as-deposited and the sample annealed at 200 ºC). This is a sign of a magnetic phase separation. This two-phase state had been discussed in the as-deposited Fe_7Au_{93} film (in all the alloys, actually), and was especially evident through the study of the asymmetry in the ZFC M_{DC} and in the $H_c(T)$ variation. In Fig. 7.20 (where the comparison is now between the as-deposited and the film annealed at 250 ºC) the two-phase state is more evident. In fact the ZFC shape is similar to that of RSG systems [59], [96]. The FC upturn is still observed although it seems slightly weakened in both annealed alloys. In principle the thermal treatment favours the mobility of the magnetic atoms through the noble metal matrix, producing the aggregation onto the Fe nanoparticles. This hypothesis fully agrees with the GMR rise above commented. When $H = 10$ kOe the irreversibility it is destroyed, as is typical in disordered magnets just bearing in mind a very general point of view. Moreover, even at intermediate fields, the high-temperature contribution (phase) is washed out in the M_{DC} curves.

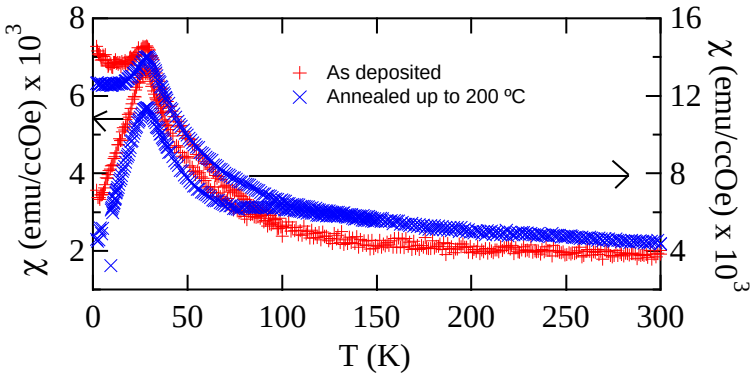

Figure 7.19: *ZFC/FC process for the as deposited (red) and annealed (blue) at $T = 200$ ºC Fe_7Au_{93} at $H = 100$ Oe. Note the shape change and the rise on the magnetisation with the thermal treatment.*

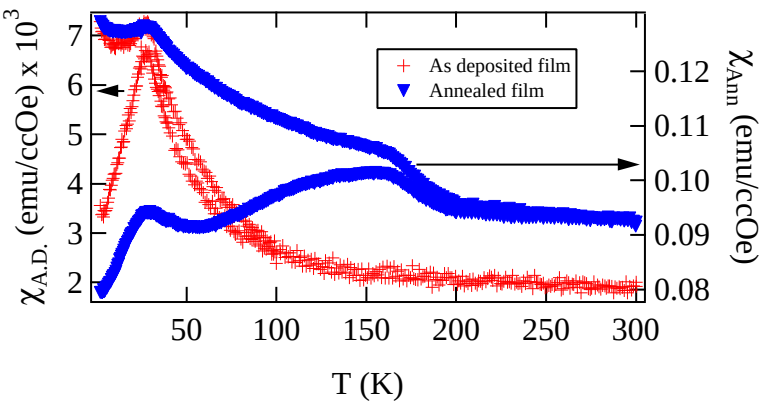

Figure 7.20: *ZFC/FC process for the as deposited (red) and annealed (blue) at T = 250 °C Fe_7Au_{93} at H = 100 Oe. Again, there is a shape change and a rise on the magnetisation with the thermal treatment. The two different phases are now more segregated, evidencing more clearly the change in the nanostructure.*

The hysteresis loops present a dramatic change when the alloy has been annealed at 250 °C (not significant changes has been observed annealing at 200 °C). The first striking detail is the higher saturation magnetisation (more than twice the value of the as-deposited film in the alloy annealed at 250 °C). Moreover, when the magnetisation is normalised to the actual volume of Fe (measured by EDX), the magnetisation per cubic centimetre of Fe shows an amazing excess magnetisation compared to that of bulk Fe. Back in the seventies, it was also observed a magnetisation rise of the Fe when it was placed into a Au matrix [46, 97]. In such reports the great magnetic moment observed per Fe atom was attributed to the existence of SPM clusters, and the value was obtained in an indirect procedure and no relevant discussion was brought into. However, recent works [98, 99] have shown the great ability of Au to become magnetically polarised. The magnetised Au could play a role in the magnetic phases previously observed and quantitative values are included in the following.

The Fe_7Au_{93} as-deposited film displays a minimum in the thermal variation of the coercive field (see fig. 7.12) which has been attributed to the existence of a magnetic decoupling process at the minimum temperature of the magnetic phases. This behaviour is

destroyed after the thermal treatment (see Fig. 7.21) of the alloy and is also interesting to observe the three-fold drop of the coercive field. Such a reduction of the coercivity can be associated with the reduction of the magnetic interactions among the magnetic particles. The annealing produces an enlargement of the Fe particles, by the addition of Fe atoms or clusters solved in the matrix but these particles become uncoupled as deduced from the $H_c(T)$ variation and $H_c^{250^oC} < H_c^{AD}$ at RT. Finally the shape of the hysteresis loops is modified, as can be observed in figure 7.22. The rise in the magnetisation at low fields is much more rapid in the annealed alloy, reaching quicker the saturation magnetisation. Again this behaviour can be interpreted as a modification in the magnetic interactions. In the as deposited film, the interactions (at random directions) are stronger, leading to the necessity of a high magnetic field to overcome and align the magnetic nanoparticles. If the interaction diminishes, the nanoparticles pinning force will be smaller, and consequently, the external magnetic field necessary to align them will be lower. As occurs in the as-deposited films, there is a lack of saturation at 45 kOe.

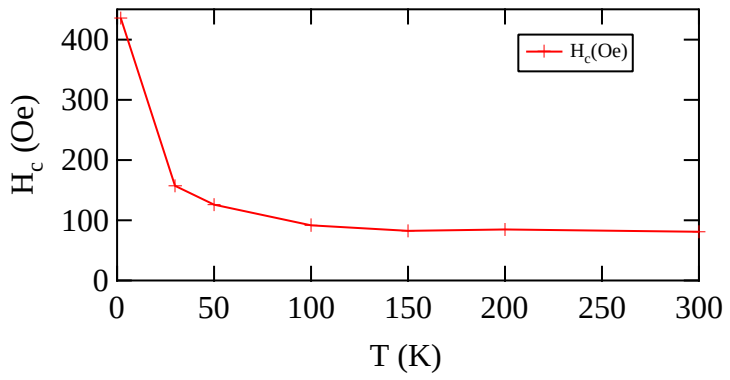

Figure 7.21: *Thermal dependence of the coercive field of the Fe_7Au_{93} film after the thermal treatment.*

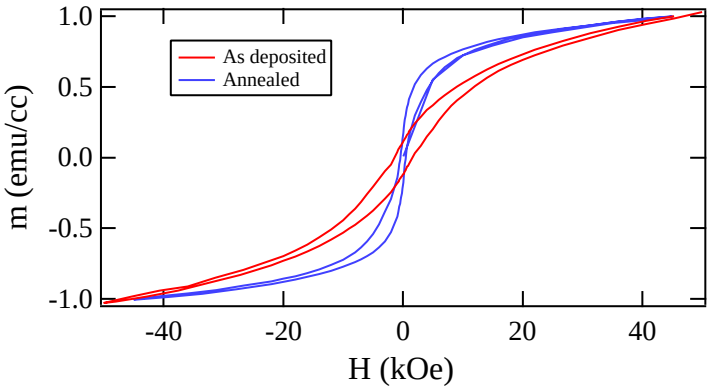

Figure 7.22: *Hysteresis loops at 2 K of the Fe_7Au_{93} thin film as deposited (red line) and after a thermal treatment (blue line). A rise in the magnetisation, a drop in the coercivity and a change in the loop shape are present.*

It have been stated that the annealing process produces a change in the nanostructure. In order to check the influence of the Au atoms in such a change, XMCD was also performed in the film annealed at 200 °C. The results can be seen in Fig. 7.23, and the integral gives values of $p = -3.061 \times 10^{-2}$ and $q = -1.476 \times 10^{-2}$, which lead to a ratio $\frac{m_{orb}^{Au_{ann}}}{m_{spin}^{Au_{ann}}} = 0.1579$, marginally larger (0.0221) than the as-deposited sample. The resultant spin magnetic moment is $m_{spin}^{Au_{Ann}} = 7.99 \times 10^{-3}\mu_B/at.Au$ and the orbital contribution $m_{orb}^{Au_{Ann}} = 1.26 \times 10^{-3}\mu_B/at.Au$, leading to a raw magnetic moment of $m_{tot}^{Au_{Ann}} = 9.25 \times 10^{-3}\mu_B/at.Au$. This Au magnetisation contribution leads to a raw magnetic moment of 4.8 emu/cc at $H = 50$ kOe. The increase of the Au magnetic moment is feeble in the annealed sample. This indicates that the polarisation of Au is still small when the nanostructure has not been modified to a great extent.

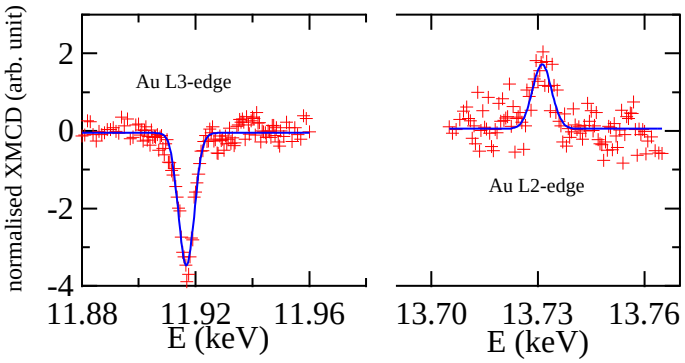

Figure 7.23: *Experimental points (red crosses) and fit (blue line) obtained for the XMCD signal at $H = 50$ kOe and $T = 5$ K for the as deposited alloy.*

Again, the ESM does not allow a measurement of the coercive field of the Au particles, and when both loops are plotted together (Fig. 7.24) it is obvious that variations do not appear significant.

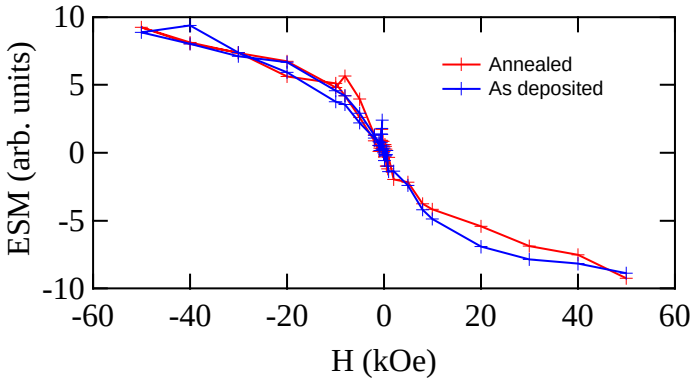

Figure 7.24: *ESM of both, as-deposited and annealed at 200 °C films. The data are normalised to the unity and then multiplied for the calculated magnetic moment at 50 kOe for a direct comparison between both.*

Bibliography

[1] J. Alonso, M. L. Fdez-Gubieda, G. Sarmiento, J. M. Barandiarán, A. Svalov, I. Orue, J. Chaboy, L. Fernández Barquín, C. Meneghini, T. Neisius, and N. Kawamura. Influence of the interface on the electronic channel switching of a Fe–Ag thin film on a Si substrate. *Appl. Phys. Lett.*, **95**:082103, 2009.

[2] J. Alonso, M. L. Fdez-Gubieda, L. Fernández Barquín, I. de Pedro, J. M. Barandiarán, I. Orue, A. Svalov, and G. Sarmiento. Collective magnetic behaviors of Fe–Ag nanostructured thin films above the percolation limit. *J. Appl. Phys.*, **105**:07B513, 2009.

[3] Anushree Roy and Ajay K. Sood. Surface and confined optical phonons in CdS_xSe_{1-x} nanoparticles in a glass matrix. *Phys. Rev. B*, **53**:12127, 1996.

[4] B. R. Taylor, S. M. Kauzlarich, G. R. Delgado, and H. W. H. Lee. Solution Synthesis and Characterization of Quantum Confined Ge Nanoparticles. *Chem. Matter*, **11**:2493–250, 2009.

[5] G. F. Goya, T. S. Berquó, F. C. Fonseca, and M. P. Morales. Static and dynamic magnetic properties of spherical magnetite nanoparticles. *Journal of Applied Physics*, **94**:3520–3528, 2003.

[6] Janet M. Petroski, Zhong L. Wang, Travis C. Green, and Mostafa A. El-Sayed. Kinetically Controlled Growth and Shape Formation Mechanism of Platinum Nanoparticles. *J. Phys. Chem. B*, **102**:3316–3320, 1998.

[7] A. P. Murani, S. Roth, P. Radhakrishna, B. D. Rainford, B. R. Coles, K. Ibel, G. Goeltz, and F. Mezei. Small angle critical neutron scattering and the onset of ferromagnetism in Au-Fe alloys. *J. Phys. F*, **6**:425, 1976.

[8] H. Chen, J. Anderson, K. Ohshima, H. Okajima, and J. Harada. Atomic short-range-order structure in Au-Fe alloys. *Phys. Rev. B*, **42**:2342, 1990.

[9] Y. Yoshida, F. Langmayr, P. Fratzl, and G Vogl. Short-range order in Au-Fe alloys studied by high-temperature Mössbauer spectroscopy. *Phys Rev. B*, **39**:6395, 1989.

[10] A. P. Murani. Ferromagnet or spin glass? Magnetic ordering in Au-Fe alloys. *J. Phys. F: Metal Phys.*, **4**:757, 1974.

[11] Z. G. Li, H. Wan, J. Liu, A. Tsoukatos, G. C. Hadjipanayis, and L. Liang. Microstructural investigation of granular Ag-Fe and Ag-Co thin films by atomic resolution and nanochemical analysis electron microscopy. *Appl. Phys. Lett.*, **63**:3011, 19993.

[12] C. J. Kinane. *The interplay of magnetism and structure in patterned multilayer thin films.* PhD thesis, University of Leeds, 2008.

[13] J. Alonso. *Collective magnetic behaviours of* Fe_xAg_{100-x} *(*$20 \leq x \leq 55$*) granular thin films ans their structural characterization.* PhD thesis, Universidad del Pais Vasco, 2010.

[14] N. S. Cohen, E. Ahlswede, J. D. Wicks, and Q. A. Pankhurst. Investigation of the ternary phase diagram of mechanically alloyed FeCuAg. *Journal of Physics: Condensed Matter*, **9**:3259, 1997.

[15] L. Fernández Barquín, R. García Calderón, B. Farago, J. Rodríguez-Carvajal, A. Bleloch, D. McComb, R. Chater, and Q. A. Pankhurst. Neutron spin echo evidence of mesoscopic spin correlations among Fe(Cu) ferromagnetic nanoparticles in a silver diamagnetic matrix. *Phys. Rev. B*, **76**(17):172404, 2007.

[16] D. Martínez-Blanco, P. Gorria, and J.A. Blanco. Nanostructured Fe obtained by high-energy ball milling. *J. Magn. Magn. Mat.*, **300**:e339–e341, 2006.

[17] R. L. Snyder, J. Fiala, and H. J. Bunge. *Defect and microstructure analysis by diffraction*. Oxford university press, New York, 1999.

[18] M. N. Baibich, J. M. Broto, A. Fert, F. Nguyen Van Dau, F. Petroff, P. Etienne, G. Creuzet, A. Friederich, and J. Chazelas. Giant magnetoresistance of (001)Fe/(001)Cr Magnetic Superlattices. *Phys. Rev. Lett.*, **61**:2472, 1988.

[19] G. Binasch, P. Grünberg, F. Saurenbach, and W. Zinn. Enhanced magnetoresistance in layered magnetic structures with antiferromagnetic interlayer exchange. *Phys. Rev. B*, **39**:4828, 1989.

[20] J. Q. Xiao, J. S. Jiang, and C. L. Chien. Giant magnetoresistance in nonmultilayer magnetic system. *Phys Rev. Lett.*, **68**:3749, 1992.

[21] R. García Calderón. *Efectos cooperativos en la relajación magnética de aleaciones nanométricas de Fe-Cu-Ag*. PhD thesis, Universidad de Cantabria, 2005.

[22] M. G. M. Miranda, E. Estevez-Rams, G. Martínez, and M. N. Baibich. Segregation dynamics in annealed CoCu ribbons: spinodal decomposition and giant magnetoresistance. *Phys. B*, **320**:139–142, 2002.

[23] L. Xing and Yia-Chung Chang. Theory of giant magnetoresistance in magnetic granular systems. *Phys. Rev. B*, 48:4156, 1993.

[24] S. Zhang. Theory of giant magnetoresistance in magnetic granular films. *Appl. Phys. Lett.*, 61:1855, 1992.

[25] A. K. Nigam and A. K. Majumdar. Anomalous magnetoresistance in AuFe spin glass. *J. Appl. Phys.*, 50:1712, 1979.

[26] F. Spizzo, E. Angeli, D. Bisero, F. Ronconi, P. Vavassori, P. Allia, V. Selvaggini, M. Coisson, P. Tiberto, and F. Vinai. GMR as a function of temperature in FeAg granular samples: the effect of magnetic interactions. *J. Magn. Magn. Mat.*, **262**:88–91, 2003.

[27] Chubing Peng, Sheng Zhang, Guozhong Li, and Daosheng Dai. Particle size dependence of magnetic behavior and giant magnetoresistance in granular Fe-Ag films. *J. Appl. Phys.*, **76**:998, 1994.

[28] Neil S Cohen, Quentin A Pankhurst, and Luis Fernandez Barquin. Structural and magnetoresistive properties of mechanically alloyed Fe-Co-Ag. *J. Phys.:Condens. Matter*, **11**:8839–8853, 1999.

[29] P. Allia, M. Coisson, P. Tiberto, F. Vinai, D. Bisero, and F. Spizzo. Magnetoresistance Analysis of Nanoscale Magnetic Correlation in Cosputtered $Fe_{100-x}Ag_x$ films. *IEEE transactions on magnetics*, **41**:3412, 2005.

[30] J. I. Gittleman, Y. Goldstein, and S. Bozowski. Magnetic Properties of Granular Nickel Films. *Phys Rev. B*, **5**:3609, 1972.

[31] J. I. Gittleman, B. Abeles, and S. Bozowski. Superparamagnetism and relaxation effects in granular Ni-SiO_2 and Ni-Al_2O_3 films. *Phys. Rev. B*, **9**:3891, 1974.

[32] F. Badia, X. Batlle, A. Labarta, M. L. Watson, A. B. Johnston, and J. N. Chapman. Magnetotrasnport properties of NiFe-Ag granular alloys: Origin of the thermal behavior. *J. App. Phys.*, **82**:677, 1997.

[33] P. Allia, M. Knobel, P. Tiberto, and F. Vinai. Magnetic properties and giant magnetoresistance of meltspun granular $Cu_{100-x}Co_x$ alloys. *Phys Rev. B*, **52**:15398, 1995.

[34] C. Kittel. *Introduction to solid state physics*. John Wiley, New York, 1986.

[35] K. H. Hellwege and O. Madelung, editors. *Numerical data and functional relationships in science and technology*, volume 19. Springer-Verlag, Germany, 1986.

[36] X. Batlle and A. Labarta. Finite-size effects in fine particles: magnetic and transport properties. *J. Phys. D: Appl. Phys.*, **35**:R15–R42, 2002.

[37] P. V. Hendriksen, S. Linderoth, and P.A. Lindgård. Magnetic properties of Heisenberg clusters. *J. Phys.: Condens. Matter*, **5**:5675, 1993.

[38] S. Linderoth, L. Balcells, A. Labarta, J. Tejada, P.V. Hendriksen, and S.A. Sethi. Magnetization and mössbauer studies of ultrafine Fe-C particles. *J. Magn. Magn. Mat.*, **124**:269–276, 1993.

[39] P. Crespo, J. M. Gonzalez, A. Hernando, and F. J. Yndurain. Spin-wave excitations in ribbon-shaped Fe nanoparticles. *Phys. Rev. B*, **69**:012403, 2004.

[40] E. Della Torre, L. H. Bennett, , and R. E. Watson. Extension of the Bloch $t^{3/2}$ Law to Magnetic Nanostructures: Bose-Einstein Condensation. *Phys. Rev. Lett.*, **94**:147210, 2005.

[41] G. Xiao and C. L. Chien. Temperature dependence of spontaneous magnetization of ultrafine Fe particles in Fe-SiO_2 granular solids. *J. Appl. Phys.*, **61**:3308, 1987.

[42] R. Aquino, J. Depeyrot, M. H Sousa, F. A. Tourinho, E. Dubois, and R. Perzynski. Magnetization temperature dependence and freezing of surface spins in magnetic fluids based on ferrite nanoparticles. *Phys Rev. B*, **72**:184435, 2005.

[43] T. N. Shendruk, R. D. Desautels, B. W. Southern, and J. van Lierop. The effect of surface spin disorder on the magnetism of γ-Fe_2O_3 nanoparticle dispersions. *Nanotechnology*, **18**:455704, 2007.

[44] E. P. Sajitha, V. Prasad, S. V. Subramanyam, Ajay Kumar Mishra, Subhajit Sarkar, and Chandrahaas Bansal. Size-dependent magnetic properties of iron carbide nanoparticles embedded in a carbon matrix. *J. Phys: Condens. Matter*, **19**:046214, 2007.

[45] K. Maaz, A. Mumtaz, S.K. Hasanain, and M.F. Bertino. Temperature dependent coercivity and magnetization of nickel ferrite nanoparticles. *J. Magn. Magn. Mat,*, **332**:2199–2202, 2010.

[46] J. A. Mydosh. *Spin Glasses: An Experimental Introduction.* Taylor and Francis, London, 1993.

[47] J. L. Dormann, D. Fiorani, and E. Tronc. Magnetic relaxation in fine-particle systems. *Adv. Chem. Phys.*, **98**:283, 1997.

[48] L. Néel. Théorie du trainage magnétique des ferromagnétiques en grains fins avec applications aux terres cuites. *Ann. Geophys.*, **5**:99–136, 1949.

[49] and M. B. Madsen S. Mörup, J. Franck, J. Villadsen, and C. J. W. Koch. A new interpretation of mössbauer spectra of microcrystalline goethite: Super-ferromagnetism or super-spin-glass behaviour? *Journal of Magnetism and Magnetic Materials*, **40**:163 – 174, 1983.

[50] J. Alonso, M. L. Fdez-Gubieda, J. M. Barandiarán, A. Svalov, L. Fernández Barquín, D. Alba Venero, and I. Orue. Crossover from superspin glass to superferromagnet in Fe_xAg_{100-x} nanostructured thin films ($20 \leq x \leq 50$). *Phys. Rev. B*, **82**:054406, 2010.

[51] W. C. Nunes, L. M. Socolovsky, J. C. Denardin, F. Cebollada, A. L. Brandl, and M. Knobel. Role of magnetic interparticle coupling on the field dependence of the superparamagnetic relaxation time. *Phys. Rev. B*, **72**:212413, 2005.

[52] S. Bedanta, T. Eimuller, W. Kleemann, J. Rhensius, F. Stromberg, E. Amaladass, S. Cardoso, and P. P. Freitas. Overcoming the dipolar disorder in dense CoFe nanoparticle ensembles: Superferromagnetism. *Phys. Rev. Lett.*, **98**:176601, 2007.

[53] C. Binns, M. J. Maher, Q. A. Pankhurst, D. Kechrakos, and K. N. Trohidou. Magnetic behavior of nanostructured films assembled from preformed fe clusters embedded in Ag. *Phys. Rev. B*, **66**:184413, 2002.

[54] N. Marcano, J. C. Gómez Sal, J. I. Espeso, L. Fernández Barquín, and C. Paulsen. Cluster-glass percolative scenario in $CeNi_{1-x}Cu_x$ studied by very low-temperature ac susceptibility and dc magnetization. *Phys. Rev. B*, **76**:224419, 2007.

[55] E. Dagotto. *Nanoscale phase separation and colossal magnetoresistance : the physics of manganites and related compounds*. Springer, Berlin, 2003.

[56] E. L. Nagaev. *Colossal magnetoresistance and phase separation in magnetic semiconductors*. Imperial college press, London, 2002.

[57] C. Raj Sankar and P. A. Joy. Superspin glass behavior of a nonstoichiometric lanthanum manganite $lamno_{3.13}$. *Phys. Rev. B*, *72*:132407, 2005.

[58] D. H. Ryan, J. M. D. Coey, E. Batalla, Z. Altounian, and J. O. Ström-Olsen. Magnetic properties of iron-rich Fe-Zr glasses. *Phys. Rev. B*, **35**:8630, 1987.

[59] S. N. Kaul, V. Siruguri, and G. Chandra. Magnetization and Mössbauer study of the reentrant amorphous $Fe_{90}Zr_{10}$ alloy. *Phys. Rev. B*, **45**:12343, 1992.

[60] R. García Calderón, L. Fernández Barquín, S. N. Kaul, J. C. Gómez Sal, Pedro Gorria, J. S. Pedersen, and R. K. Heenan. Small-angle neutron scattering study of a magnetically inhomogeneous amorphous alloy with reentrant behavior. *Phys. Rev. B*, **71**:134413, 2005.

[61] Masatsugu Suzuki, Sharbani I. Fullem, Itsuko S. Suzuki, Lingyan Wang, and Chuan-Jian Zhong. Observation of superspin-glass behavior in Fe_3O_4 nanoparticles. *Phys Rev. B*, **79**:024418, 2009.

[62] Anita Semwal and S. N. Kaul. Irreversibilities in low-field magnetization of site-disordered $Ni_{75}Al_{25}$. *Phys. Rev. B*, **68**:024410, 2003.

[63] B. D. Cullity. *Introduction to magnetic materials*. Addison-Wesley, Massachusetts, 1972.

[64] J. R. L. de Almeida and D. J. Thouless. Stability of the Sherrington-Kirkpatrick solution of a spin glass model. *J. Phys. A: Math. Gen.*, **11**:983, 1978.

[65] R. V. Chamberlin, M. Hardiman, L. A. Turkevich, and R. Orbach. $h - t$ phase diagram for spin-glasses: An experimental study of Ag:Mn. *Phys. Rev. B*, *25*:6720, 1982.

[66] B. Martınez, X. Obradors, Ll. Balcells, A. Rouanet, and C. Monty. Low Temperature Surface Spin-Glass Transition in γ-Fe_2O_3 Nanoparticles. *Phys Rev. Lett.*, **80**:181, 1998.

[67] F. Jiménez-Villacorta, J. Sánchez-Marcos, E. Céspedes, M. García-Hernández, and C. Prieto. Effects of interparticle interactions in magnetic Fe/Si_3N_4 granular systems. *Phys Rev. B*, **82**:134413, 2010.

[68] P. Allia, M. Coisson, J. Moya, P. Tiberto, and F. Vinai. Granular metallic systems as interacting superparamagnets: anhysteretic magnetization and hysteresis loops. *J. Magn. Magn. Mat.*, **254–255**:143–148, 2003.

[69] R. H. Kodama, A. E. Berkowitz, E. J. McNiff, Jr., and S. Foner. Surface spin disorder in $NiFe_2O_4$ nanoparticles. *Phys. Rev. Lett.*, **77**:394, 1996.

[70] M. El Ghannami, C. Gómez-Polo, G. Rivero, and A. Hernando. Exchange Correlation Length and Magnetoresistance in Fe-Cu and Fe-Cu-Ni Melt-Spun Ribbons. *Europhys. Lett.*, **26**:701, 1994.

[71] P. Crespo, A. Hernando, R. Yavari, O. Drbohlav, A. García Escorial, J. M. Barandiarán, and I. Orue. Magnetic behavior of metastable fcc Fe-Cu after thermal treatments. *Phys. Rev. B*, **48**:7134, 1993.

[72] P. Crespo, A. Hernando, and A. García Escorial. Spinodal decomposition of FeCu nanocrystals: Control of the atomic magnetic moment and magnetic porperties. *Phys Rev. B*, **49**:13227, 1994.

[73] G. Herzer. Grain structure and magnetism of nanocrystalline ferromagnets. *IEEE transactions on magnetics*, **25**:3327, 1989.

[74] L. Fernández Barquín, J. C. Gómez Sal, P. Gorria, J. S. Garitaonandia, and J. M. Barandiarán. Dynamic susceptibility of reentrant Fe-rich inhomogeneous amorphous alloys. *Eur. Phys. J. B*, **35**:3, 2003.

[75] Vassil Skumryev, J. Nogués, J. S. Muñoz, B. Martínez, R. Senis, J. Fontcuberta, L. Pinsard, A. Revcolevschi, and Y. M. Mukovskii. Anomalous anisotropic ac susceptibility response of $La_{1-x}Sr_xMnO_3$ ($x \approx 1/8$) crystals: Relevance to phase separation. *Phys. Rev. B*, **62**:3879, 2000.

[76] J. A. De Toro, M. A. López de la Torre, J. M. Riveiro, J. Bland, J. P. Goff, and M. F. Thomas. Magnetic nanogranularity and spin-glass behavior in mechanically alloyed $Fe_{35}Al_{50}B_{15}$. *Phys. Rev. B*, **91**:8396, 2002.

[77] D. Alba Venero, L. Fernández Barquín, J. A. De Toro, and J. M. Riveiro. Spin dynamics of the low temperature magnetic relaxation in disordered $Fe_{35}Al_{50}B_{15}$ alloys. *To be published*, 2011.

[78] Xi Chen, S. Bedanta, O. Petracic, W. Kleemann, S. Sahoo, S. Cardoso, and P. P. Freitas. Superparamagnetism versus superspin glass behavior in dilute magnetic nanoparticle systems. *Phys. Rev. B*, **72**:214436, 2005.

[79] S. Geschwind, A.T. Ogielski, G. Delvin, J. Hegarty, and P. Bridenbaugh. Activated dynamic scalling and magnetic ordering in $Cd_{1-x}Mn_xTe$: Spin glass or random antiferromagnet. *J. Appl. Phys.*, **6**3, 1988.

[80] J. L. Tholence and R. Tournier. Susceptibility and remanente magnetization of a spin glass. *Journal de physique*, **5**:C4–229, 1974.

[81] Marco Picco and Felix Ritort. Dynamical ac study of the critical behavior in Heisenberg spin glasses. *Phys. Rev. B*, **71**:100406, 2005.

[82] Andrew T. Ogielski and Ingo Morgenstern. Critical behavior of three-dimensional Ising spin-glass model. *Phys. Rev. Lett.*, **54**:928, 1985.

[83] C. Djurberg, P. Svedlindh, P. Nordblad, M. F. Hansen, F. Bødker, and S. Mørup. Dynamics of an Interacting Particle System: Evidence of Critical Slowing Down. *Phys. Rev. Lett.*, **79**:5154, 1997.

[84] J. Bartolomé, F. Bartolomé L. M. García, F. Luis, F. Petroff R. López-Ruiz, C. Deranlot, F. Wilhelm, A. Rogalev, P. Bencok, N. B. Brookes, L. Ruiz, and J. M. González-Calbet. Magnetic polarization of noble metals by Co nanoparticles in M-capped granular multilayers (M = Cu, Ag, and Au): An x-ray magnetic circular dichroism study. *Phys Rev. B*, **77**:184420, 2008.

[85] F. Wilhelm, M. Angelakeris, N. Jaouen, P. Poulopoulos, E. Th. Papaioannou, Ch. Mueller, P. Fumagalli, A. Rogalev, and N. K. Flevaris. Magnetic moment of Au/Co interfaces: A direct experimental determination. *Phys Rev. B*, **69**:220404R, 2004.

[86] P. J. Ford and J. A. Mydosh. Electrical resistivity of noble-metal-host-3d solute spin glass alloys. *Phys. Rev. B*, **14**:2057, 1976.

[87] J. P. Franck, F. D. Manchester, and D. L. Martin. The Specific Heat of Pure Copper and of Some Dilute Copper+Iron Alloys Showing a Minimum in the Electrical Resistance at Low Temperatures. *Proc. Roy. Soc. B*, **263**:494, 1961.

[88] L. M. Fabietti, J. Ferreyra, M. Villafuerte, S. E. Urreta, and S. P. Heluani. Kondo-like effect in magnetoresistive CuCo alloys. *Phys Rev. B*, **82**:172410, 2010.

[89] G. T. Meaden. *Electrical resistance of metals.* Heywood books, London, 1966.

[90] J. A. Mydosh, P. J. Ford, M. P. Kawatra, and T. E. Whall. Electrical resistivity of AuFe alloys in the spin-glass mictomagnetic and ferromagnetic regimes. *Phys. Rev. B*, **10**:2845, 1974.

[91] A. Gerber, A. Milner, I. Ya. Korenblit, M. Karpovsky, A. Gladkikh, and A. Sulpice. Temperature dependence of resistance and magnetoresistance of nanogranular Co-Ag films. *Phys. Rev. B*, **57**:13667, 1998.

[92] A. Milner, I. Ya. Korenblit, and A. Gerber. Effect of magnetic impurities on electronic transport of heterogeneous ferromagnets. *Phys. Rev. B*, **60**:14821, 1999.

[93] D. Gómez Plaza, L. Fernández Barquín, J. García Soldevilla, R. Antras, and J. C. Gómez Sal. Annealing and magnetic field effects on the resistivity of Fe-rich Fe-Zr glasses. *Solid State Communications*, **102**:353, 1997.

[94] A. Das and A. K. Majumdar. High temperature resistivity minima in Co-rich amorphous ferromagnets. *Phys. Rev. B*, **43**:6042, 1991.

[95] A. García Prieto, M. L. Fdez-Gubieda, J. Chaboy, M. A. Laguna-Lago, T. Muro, and T. Nakamura. Interface effects on the magnetic moment of Co and Cu in CoCu granular alloys. *Phys Rev. B*, **72**:212403, 2005.

[96] Anita G. Berndt, X. Chen, H. P. Kunkel, and Gwyn Williams. Field-dependent ac susceptibility of amorphous $(Fe_{1-x}Mn_x)_{75}P_{16}B_6Al_3$: Weakly frustrated regime. *Phys. Rev. B*, **52**:10160, 1995.

[97] V. Canella and J. A. Mydosh. Magnetic ordering in Fe-Au alloys. *Phys. Rev. B*, **6**:4220, 1972.

[98] P. Crespo, R. Litran, T. C. Rojas, M. Multigner, J. M. de la Fuente, J. C. Sanchez-Lopez, M. A. Garcıa, A. Hernando, S. Penadés, , and A. Fernandez. Permanent Magnetism, Magnetic Anisotropy, and Hysteresis of Thiol-Capped Gold Nanoparticles. *Phys. Rev. Lett.*, **93**:087204, 2004.

[99] Y. Yamamoto, T. Miura, M. Suzuki, N. Kawamura, H. Miyagawa, T. Nakamura, K. Kobayashi, T. Teranishi, and H. Hori. Direct Observation of Ferromagnetic Spin Polarization in Gold Nanoparticles. *Phys. Rev. Lett*, **93**:116801, 2004.

Chapter 8

Overall picture and conclusions

It is instructive trying to compile altogether the results and their discussion in order to draw a complete picture of the alloys and the underlying physical mechansims governing the magnetic behaviour. As can be seen in figure 8.1, bulk alloys with similar chemical composition behave as spin glasses ($x \leq 16\%$ at.). This excellent sumary published in the 90s is a remarkable roadsheet for further investigations. In this recipe, it should not be forgotten the possible role of the Kondo effect (for example for Fe solved in Cu) or a metallurgical lack of solubillity (like in Fe-Ag alloys). The freezing temperature in this SG rises with increasing Fe concentration. Above a certain amount of Fe, a ferromagnetic phase is present, in the the so-called reentrant spin glasses state (RSG).

When the solved spin are replaced by nanoparticles, the general landscape is modified, entering into the *supermagnetism*. For example, inspecting again figure 8.1, it can be deduced that a bulk alloy of $Fe_{24}Au_{76}$ is a ferromagnet below 200 K. However, a system with a close chemical composition, like $Fe_{24}Ag_{76}$ but composed by nanoparticles, presents a spin glass like (super spin glass) behaviour up to 140 K, being superparamagnetic at higher temperatures. Actually, in Fe_xAg_{100-x} a very attractive crossover from super spin glass to superferromagnet have been observed recently, as it has been summarised in Fig. 8.2. The interpretation there is attributed to the magnetic percolation of the system, motivated by the increasing importance of direct exchange interactions as the density of Fe nanoparticles increases.

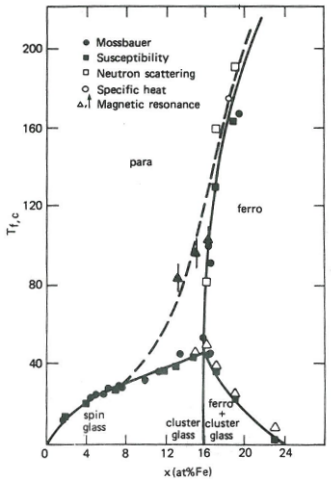

Figure 8.1: *Phase diagram of diluted Fe solved in a Au matrix. The freezing temperatures have been obtained with different techniques. Reproduced form the book "Spin Glasses: An Experimental Introduction".*

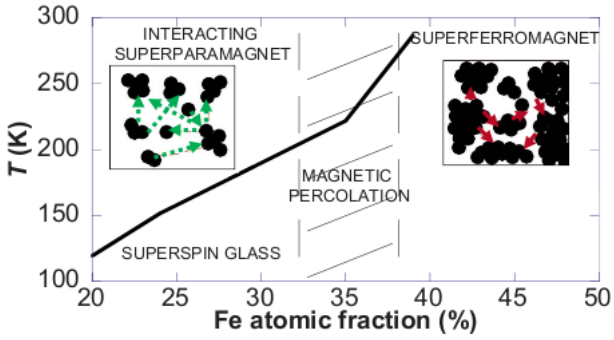

Figure 8.2: *Phase diagram of Fe_xAg_{100-x} composed by nanoparticles instead of solved spins. The difference between both magnetic phase diagram are evident. There is a crossover from a SSG to a SFM behaviour in the region where the magnetic percolation takes place. Reproduced form Phys. Rev. B* ***82*** *: 054406 2010.*

In this thesis we have studied systems somehow between the previously described: the chemical composition is close to those in the canonical spin glass region ($x \lesssim 15\%\ at.$) but the alloys are composed by nanoparticles, as was demonstrated by the magnetoresistance results. Even with the extensive structural characterisation performed, a defined size distribution and correlation length of the Fe nanoparticles has not been fully obtained.

Our system presents a super spin glass phase at low temperatures (as has been proved by χ_{AC}). Surprisingly, despite the low Fe-concentration, there is ferromagnetism *like* at room temperature. This fact justifies the crucial importance of the nanostructure: such diluted alloys are expected to behave as a superparamagnet, but the importance of the magnetic interactions modify those expectations.

Another salient result is the presence of different magnetic phases within the metallic arrangement.Two phases have been ascertained from the ZFC peak shape and the thermal dependence of the coercive field with temperature. Those phases are confirmed beyond any doubt by the annealing of the Fe_7Au_{93} film. To determine the exact nature of the second phase (assuming that "pure" Fe nanoparticles is the other) it is an interesting (and challenging) problem that may deserve further attention.

The sputtering route allows a modification of the traditional phase diagram of FeAu canonical spin glasses. Inserting the additional points obtained in our work and those in the more concentrated Fe_xAg_{100-x} thin films we can obtain figure 8.3. The Fe_7Au_{93} freezing temperature matches perfectly that of the canonical spin glass, although the films are constituted by an ensemble of nanoparticles of both, Fe and Au. By contrast, the rest of the alloys present a transition temperature below the corresponding FeAu for such a chemical composition, in some sense coming from the matrix nature. Eventually, the work presented here should be extended to assess with precision the existence of compositional trends.

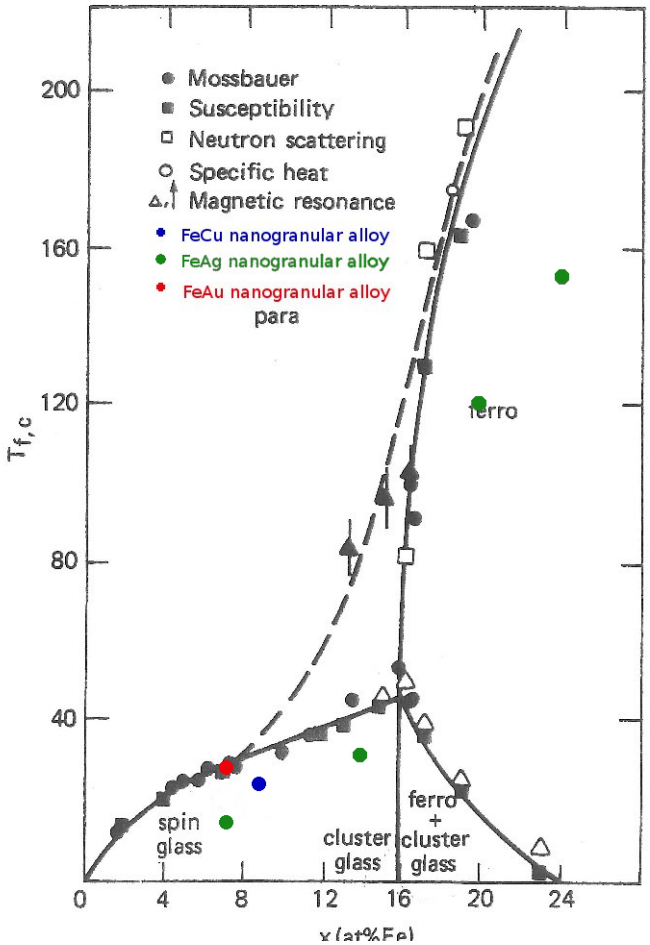

Figure 8.3: *Modified phase diagram of the Fe_xAu_{100-x}, where the new points coming from our super spin glass systems have been inserted.*

Summarising, the main conclusions of this work are:

- Magnetic binary (Fe_xM_{100-x}: M = Au, x = 7; M = Ag, x = 7, 14; M = Cu, x = 9) nanostructured thin films with SSG behaviour have been deposited by DC-magnetron sputtering. The films are composed by nanoparticles of both, Fe and the noble metal with mean diameters below 10 nm.

- Two magnetic phases have been detected. Its presence produces a rise of the coercitive field above a certain temperature ($T \gtrsim 50$ K), consequence of a decrease of the magnetic coupling.

- A curious FC upturn is observed in the magnetisation. The origin is still controversial: the existence of paramagnetic solved atoms is discarded in a very wide compositional range by the absence of a Kondo minimum in the variation of the resistivity with the temperature. On the other hand, the decrease of the upturn, as well as the rise of the GMR after the annealing may be correlated with spins solved in the matrix.

- A thermal treatment (above 200 °C) changes drastically the magnetic response of the alloy: the two phases become segregated. Since both transitions are well separated, a further study would be interesting to follow their behaviour (higher temperatures for examples).

- XMCD reveals the existence of an induced moment in the Au atoms reaching a value of $\mu = 9.25$ x 10^{-3} $\mu_b/at.Au$. This value of the Au polarisation is in the same order of magnitude of other nanostructured binary systems.

Publication list

- D. Alba Venero , R. Rodríguez García;2 , L. Fernández Barquín , E. Apiñaniz , J. S. Garitaonandia , and F. Plazaola. Dynamics of the Magnetic Susceptibility of $Fe_xAl_{100-x}(x = 70, 71)$ Alloys. *IEEE trans. magn.*, **44**:3883, 2008

- D. Alba Venero , L. Fernández Barquín , J. Alonso , A. Svalov and M. L. Fdez-Gubieda. Magnetic disorder in nanostructured Fe_7Au_{93} films and $Fe_{14}Au_{86}$ powders. *J. Phys: Conf. series*, **200**:072028, 2010

- J. Alonso, M. L. Fdez-Gubieda, J. M. Barandiarán, A. Svalov, L. Fernández Barquín, D. Alba Venero, and I. Orue. Crossover from superspin glass to superferromagnet in Fe_xAg_{100-x} nanostructured thin films ($20 \leq x \leq 50$). *Phys. Rev. B*, **82**:054406, 2010.

- L. Fernández Barquín, D. Alba Venero, C. Echevarria Bonet, R. García Calderón and D. Rojas Pupo. Scrutinising magnetic disorder through metastable 3d- and 4f-nanostructured alloys. *Invited contribution to the ISMANAN conference* (2011)

- D. Alba Venero , L. Fernández Barquín , J. Alonso , M. L. Fdez-Gubieda and A. Svalov. Superspin glass state in diluted Fe_xM_{100-x} thin films. *to be submitted to Phys. Rev. B.*

- D. Alba Venero , L. Fernández Barquín , J. Alonso , M. L. Fdez-Gubieda, A. Svalov, R. Boada, C. Guglieri, J. Chaboy and M. Suzuki. Polarisation of Au in Fe-Au nanometric thin films. *to be submitted to EPL.*

List of Tables

List of Figures